

A search for the Higgs boson decaying to e^+e^- using data from the ATLAS detector

Master Thesis in experimental particle physics

by

Tor Gunnar Hagen

Supervisors: Professor Bjarne Sandvik Stugu

Professor Gerald Eigen



Department of Physics and Technology

University of Bergen

June 14, 2021

Acknowledgements

I would like to thank my advisors Professor Bjarne Sandvik Stugu and Professor Gerald Eigen for giving me this thesis related to the decay of the Higgs Boson. Without your help and encouragement, I would not have succeeded in my studies. I can not thank you enough! I would like to thank Graham Richard Lee, Postdoctoral Fellow, for all the help with ROOT and for answering all my stupid questions.

I would also thank my fellow student Rasmus Jørgensen Brekke for the good time working on the master thesis and cooperation working on the data from CERN.

I would like to thank my partner Amalie Storesund for laughing at most of my jokes. Lastly, I would like to thank my dad, Dr. Bjarne Christian Hagen, for reading through my thesis and giving me a lot of feedback, even though he did not understand what I was doing.

Abstract

Aim: The aim of this thesis is to examine the decay of the Higgs boson to an electron-positron pair, $H \rightarrow e^+e^-$ using the invariant mass of the leading and sub-leading electrons.

Method: An invariant mass reconstruction model, with two different types of cuts, was developed by looking at a $Z \rightarrow e^+e^-$ Monte Carlo sample and then real data. The model was then been run on real data from the LHC.

Findings: By running the model against real data, it is found that the model correctly identifies the presence of Z bosons and also confirms that Higgs bosons are not present in the samples that the model is investigating. This model got limits for the effective cross sections of the $H \rightarrow e^+e^-$ decay. For the 2018 sample with a $p_T > 20$ GeV cut the effective cross section limit was found to be $\sigma_{eff} < 99.04$ fb and for the 2016 sample with Loose electrons the effective cross section limit was found to be $\sigma_{eff} < 24.23$ fb.

Contents

Acknowledgements	ii
Abstract	iii
1 Introduction	1
1.1 Background	1
1.2 Problem statement	2
1.3 Limitations	2
2 The experimental equipment	4
2.1 CERN	4
2.2 LHC	5
2.3 The ATLAS Detector	7
2.3.1 The Inner Detector	8
2.3.2 Calorimeters	10
2.3.3 Muon spectrometer	11
2.3.4 Coordinates	12
2.4 Electron reconstruction and identification	13
3 The Standard Model	15
3.1 Notation	15
3.2 Elementary particles	17
3.3 Quantum Field Theory	19
3.3.1 Group theory	20
3.3.2 Quantum Electrodynamics	22
3.3.3 Quantum Chromodynamics	23
3.3.4 Electroweak	27

3.4	The Higgs Boson	30
3.5	Higgs production at ATLAS	36
4	Simulation	40
4.1	Monte Carlo	40
4.1.1	Simulated events	41
4.1.2	Event Reconstruction	42
4.2	The Grid	43
4.3	Athena and samples	43
4.3.1	ROOT	43
4.3.2	C++ and Python	44
5	Monte Carlo $Z \rightarrow e^+e^-$	45
5.1	Sample	45
5.2	Kinematics	46
5.3	Background	53
5.4	Selection optimisation	56
5.5	Concluding comment	61
6	Real data: $Z \rightarrow e^+e^-$	63
6.1	Kinematics	63
6.2	Cuts	68
6.2.1	p_T cuts	68
6.2.2	Working point cut	72
6.3	Concluding comment	76
7	$H \rightarrow e^+e^-$	77
7.1	Higgs region from a single file	77
7.2	Higgs region from a whole sample	79
7.2.1	2018 data with a $p_T > 20$ GeV cut	81
7.2.2	2016 data with Loose working points	82
7.2.3	Υ and J/Ψ found in the Loose invariant mass plot	84
7.3	Analysing $H \rightarrow e^+e^-$ using $p_T > 20$ GeV cut	85
7.4	Analysing $H \rightarrow e^+e^-$ using Loose working points	89
7.5	Concluding comment	91

8	Results and Discussion	93
8.1	Finding Z and H using model	93
8.2	Uncertainty	95
8.3	Improving cuts	96
8.4	Concluding remark	97
9	Conclusion	98

List of Figures

2.1	Inner Detector of ATLAS [13].	8
2.2	Calorimeter at ATLAS [20].	11
2.3	Muon spectrometer at ATLAS [23].	12
2.4	Pseudorapidity and theta [11]	13
3.1	Ways that the Higgs boson is produced at the ATLAS detector [29]	37
3.2	Ways that the Higgs boson decay that is detected at the ATLAS detector [30]	38
3.3	Decays of the Standard Model Higgs [32]	39
4.1	An example of how an event generator can simulate a proton proton collision [36]	41
4.2	A schematic representation of the Full Chain Monte Carlo production [37]	42
5.1	The angles η and ϕ of the electrons in the sample.	46
5.2	Electron Truth (Blue) and reconstructed (Truth) η (black). . .	47
5.3	The p_T and energy of the electron candidates in the sample. .	47
5.4	Number of electrons per event.	48
5.5	The leading and subleading p_T of the electrons in the sample.	48
5.6	Scatter plot of leading vs subleading p_T . There are bright spots at coordinates (5,5) and (45,45)	49
5.7	The reconstructed invariant mass.	50
5.8	The p_T of truth electrons and matched electrons.	51
5.9	Truth - matched electron η and p_T for finding the η and p_T resolutions.	51

5.10	p_T resolution vs truth p_T	52
5.11	Truth - matched electron p_T for different truth p_T ranges to see how the distribution changes.	52
5.12	The invariant mass for matched and truth electrons.	52
5.13	Background plots with $Z \rightarrow \tau\tau$, ttbar, single top, Drell-Yan and diboson.	54
5.14	Background plots with $Z \rightarrow \tau\tau$, ttbar, single top, Drell-Yan and diboson on a log scale.	55
5.15	Invariant mass for background processes, $Z \rightarrow \tau\tau$, ttbar, single top, Drell-Yan and diboson, and a truth-matched $Z \rightarrow e^+e^-$ signal sample.	55
5.16	Background plots with $Z \rightarrow \tau\tau$, ttbar, single top, Drell-Yan and diboson and min bias.	56
5.17	Background plots with $p_T > 20$ cuts.	57
5.18	Efficiency plotted against transverse energy E_T [24].	58
5.19	The leading and subleading p_T of the electrons.	58
5.20	Loose invariant mass.	59
5.21	Loose background with p_t cuts.	59
5.22	Truth invariant mass for $ \eta < 2.7$	60
5.23	Invariant mass plot with a $p_T > 20$ GeV cut. The FWHM of this fit is 5.06 GeV.	61
6.1	The angles η and ϕ of the electrons in the real data.	64
6.2	The energy and p_T of the electrons in the real data.	64
6.3	Number of electron candidates in per event.	65
6.4	The leading and subleading p_T of the electrons in the real data.	66
6.5	Scatter plot of leading vs sub-leading p_T . There are brightspots at coordinates (3,35) and (45,45).	67
6.6	Invariant mass plot of the data.	68
6.7	The leading and subleading p_T of the electrons in the real data with $p_T > 20$ GeV.	69
6.8	Scatter plot of leading vs sub-leading p_T with $p_T > 20$ GeV. There are brightspots at coordinates (35,30) and (45,45)	70
6.9	Invariant mass plot of the data with $p_T > 20$ GeV, but without the Higgs region.	71
6.10	The angles η and ϕ of the Loose electrons in the real data.	72

List of Figures

6.11	The energy and p_T of the Loose electrons in the real data.	73
6.12	The number of electrons per event when looking at the Loose electrons.	73
6.13	The leading and subleading p_T of the Loose electrons in the real data.	74
6.14	Scatterplot of the p_T of the leading electrons and sub-leading electron. There is a brightspot at coordinate (45,45)	74
6.15	Invariant mass plot of the data with Loose working points without the Higgs region. The FWHM of this fit is 5.15 GeV	75
7.1	The invariant mass with Higgs region from a single file from the 2018 sample.	78
7.2	The Higgs region of the invariant mass from a single file from the 2018 sample with sub-leading $p_T > 20$ GeV cut seen in fig. 6.9 fitted with a Breit-Wigner with an exponential background. Here the mass of the Breit-Wigner is set to be the Higgs mass, 125 GeV.	78
7.3	The Higgs region of the Loose invariant mass from a single file from the 2018 sample seen in fig. 6.15 fitted with a Breit-Wigner with an exponential background. Here the mass of the Breit-Wigner is set to be the Higgs mass, 125 GeV.	79
7.4	Invariant mass of the whole 2018 sample.	80
7.5	The invariant mass of the whole 2018 sample with a $p_T > 20$ GeV cut.	81
7.6	The Loose invariant mass of the whole 2016 sample.	83
7.7	The Loose invariant mass of the whole 2018 sample in the 0 GeV to 15 GeV region.	84
7.8	The truth invariant mass of the MC $Z \rightarrow e^+e^-$, here fitted with a Breit-Wigner.	86
7.9	The Higgs region of the invariant mass of the whole 2018 sample with a $p_T > 20$ GeV cut fitted with a background in green. The Chi2 of this fit is 88.08.	86
7.10	The Higgs region of the invariant mass of the whole 2018 sample with a $p_T > 20$ GeV cut. Here a simulated Higgs peak is plotted with a Gaussian in red.	87

7.11	The Higgs region of the invariant mass of the whole 2018 sample with a $p_T > 20$ GeV cut. Here a Higgs peak is fitted with a Gaussian in red and background in green.	88
7.12	The Higgs region of the invariant mass of the whole 2018 sample with a $p_T > 20$ GeV cut with a Gaussian in red and background in green. This plot is zoomed in.	88
7.13	The Higgs region of the Loose invariant mass of the whole 2016 sample fitted with a background in green. The Chi2 of this fit is 164.96	89
7.14	The Higgs region of the Loose invariant mass of the whole 2016 sample. Here with a simulated Higgs peak in red.	90
7.15	The Higgs region of the Loose invariant mass of the whole 2016 sample. Here a Higgs peak is fitted with a Gaussian in red and background in green.	90
7.16	The Higgs region of the Loose invariant mass of the whole 2016 sample with a Gaussian in red and background in green. This plot is zoomed in.	91

List of Tables

3.1	Comparing SI and natural units	17
3.2	Fermions	18
3.3	Bosons and the forces	18
3.4	The cross sections for Higgs production at a c.o.m energy of $\sqrt{(s)} = 13$ TeV, in pb. [33].	37
5.1	Cross section for the different backgrounds	53
5.2	The significance of the p_T cuts	57
5.3	The significance of the p_T cuts and Loose working points . . .	60
6.1	The significance of the real data before any cuts	68
6.2	The significance of the p_T cuts.	70
6.3	The significance of the p_T cuts on Loose electrons.	76

Chapter 1

Introduction

1.1 Background

The Standard Model (SM) is a very successful model of particle physics. It explains elementary particles and their interactions. One of the bases of this theory is the electroweak force, a way of explaining the electromagnetic and weak force with the same theory. However, this theory implies that the force carriers for the weak force, known as the W and Z bosons, have zero mass, but these particles have nearly 100 times the mass of a proton. Robert Brout, François Englert and Peter Higgs made a proposal on how to solve this problem, what is now known as the Higgs mechanism. The W and Z bosons get masses from interacting with the Higgs field. This field is responsible of giving mass to all the elementary particles. Like with all quantum fields, the Higgs field has an associated particle, the Higgs boson [35].

The Large Hadron Collider (LHC) is the worlds most powerful particle accelerator and is one of the colliders at CERN. It consists of a 27 kilometer long ring with a number of accelerating structures that boost the energy of the particles going through it [4]. Some of the main goals of the LHC are to look for more fundamental interactions not found in less powerful colliders, study the properties of anti-matter and to search for the Higgs boson. On 4. July 2012, CERN announced that the ATLAS and CMS experiments at the LHC had identified a particle consistent with the Higgs boson in the mass region around 125 GeV.

It is important to map all properties of the particle that was found in

2012 to confirm that they are consistent with the expected properties of the Standard Model's Higgs boson. Even if the branching ratio to e^+e^- is expected to be very small, it should be sought, so that good boundaries of the decay can be set. Most of the data we have so far are in decay channels of heavy bosons (ZZ or W^+W^-) or quarks and leptons in the third generation (ttbar, bbbar and $\tau^+\tau^-$). It is important to search for Higgs in the decay of 1st and 2nd generation particles as well.

1.2 Problem statement

The aim of this thesis is to examine the e^+e^- decay mode of the Higgs boson. A model to determine the invariant mass was developed by taking the leading and sub-leading electrons and adapting cuts to them using a Monte Carlo $Z \rightarrow e^+e^-$. This model will then be tested using a single real data file from 2018 and then used on all the data from 2018 and 2016 for two different types of cuts to find the Higgs boson in the 125 GeV region.

1.3 Limitations

In this thesis $Higgs \rightarrow e^+e^-$ is examined using an invariant mass model. The model is developed using a Monte Carlo $Z \rightarrow e^+e^-$ sample, as there was no Monte Carlo $H \rightarrow e^+e^-$ sample available. The invariant mass model created works very well for $Z \rightarrow e^+e^-$, but without a Monte Carlo $H \rightarrow e^+e^-$ sample one can not verify how well the model identifies the Higgs boson. This limitation is probably not a large issue, but it gives some uncertainty of the efficiency, ϵ , of the model.

When looking at real data, a 2018 DAOD was used for most of the analysis. However, when implementing a working point cut on the whole sample, using the Grid, these cuts did not go through. This did not work on a 2017 DAOD of the same type either. Therefore a 2016 DAOD sample was used instead. This sample have lower integrated luminosity than the 2018 sample used in the rest of the thesis.

Working points were a problem in general. On the original real data sample that was looked at, none of the working point types worked. Because of this, another real data sample was analysed, the 2018 DAOD used in

most of the real data chapters. There are several types of working points, VeryLoose, Loose, Medium, Tight and more, but in this thesis only the Loose working point was used. This is because Loose was the only of the working point that worked for us. The stronger working point cuts could have given stronger result, but this did not work.

When running on the Grid, some of the grid jobs returned 0 files and for the 2018 data sample only 440 out of the 540 files that was created could be read by ROOT. This gives some uncertainty to the luminosity that was run over. Another problem with the Grid is the number of times it took before it worked and every time it ran it could take up to 2 days. This limited the number of runs that was carried out.

Chapter 2

The experimental equipment

The experimental results that will be analysed in this work are produced at the Large Hadron Collider (LHC) at CERN.

2.1 CERN

CERN, the European Organization for Nuclear Research, in Geneva Switzerland, operates the largest particle physics laboratory in the world. It was established in 1954 and has 23 member states from Europe and scientist from around the world are performing research at CERN [2]. From the work done at CERN many important findings and innovations have been introduced. Examples are the neutral currents in 1973 and the discovery of W and Z bosons in 1983 [25]. These were predicted by the electroweak theory, a part of the Standard Model, but without experimental results this could not be confirmed. Studies of antimatter and their properties are also being performed to get a better understanding of why there is so much ordinary matter in the universe, but so little antimatter. One of the biggest technological advances developed CERN is the World Wide Web (WWW). Tim Berners-Lee invented the World Wide Web in 1989 and made the first web browser in 1990 while working for CERN. WWW was released outside of CERN in 1991 [3].

2.2 LHC

The Large Hadron Collider (LHC) is the world's most powerful particle accelerator and is a part of CERN [4]. It consists of a 27 kilometer long ring with superconducting magnets and structures to accelerate protons and heavy ions. Inside the accelerator there are two particle beams that travel close to the speed of light, in opposite directions, in two tubes kept at a vacuum. These beams are made to collide at four different detectors: ATLAS, CMS, ALICE and LHCb [4].

LHC is a synchrotron, a circular accelerator. The first circular accelerator, the cyclotron, was proposed by Lawrence in 1930 and the more powerful synchrotron was proposed in 1945 by McMillan and Veksler [28]. An injector sends particles into the ring with an initial energy E_i . The particles get guided around the ring by dipole magnets, and accelerated by radiofrequency (RF) cavities [28]. The time a particle uses around the ring is:

$$T = \frac{2\pi R}{v} = \frac{2\pi RE}{pc^2} \quad (2.1)$$

where R is the radius of the ring, c is the speed of light and v , E and p is the speed, energy and momentum of the particle.

The LHC uses 1232 dipole magnets to keep the particles on its path and 392 quadrupole magnets to focus the particle beam to increase the luminosity [4]. The dipoles produce a 7.7 T magnetic field to slightly turn the particles, but since they are charged they also repel each other, so they must be focused using quad magnets. Classical electrodynamics tells that accelerating charges lets out radiation and in synchrotrons this radiation is called synchrotron radiation [28]. The power P generated from synchrotron radiation is:

$$P = \frac{2e^2c}{3R^2} \frac{\beta^4}{(1-\beta^2)^2} \approx \frac{2e^2c}{3R^2} \gamma^4 \quad (2.2)$$

Where e is the elementary charge, R is the radius of the collider and $\gamma = \frac{1}{\sqrt{1-\frac{v^2}{c^2}}} = \frac{E}{mc^2}$. If the velocity is close to c then $\beta = \frac{v}{c} \approx 1$ the power becomes:

$$P \approx \frac{2e^2c}{3R^2} \gamma^4 = \frac{2e^2c}{3R^2} \left(\frac{E}{mc^2} \right)^4 \quad (2.3)$$

The particle energy loss during one rotation in the ring is

$$-\Delta E = PT \approx \frac{4\pi e^2}{3R} \left(\frac{E}{mc^2} \right)^4 \quad (2.4)$$

Difference in energy loss between electrons and protons in a synchrotron can be found using eq. 2.4. For equal radius (R) and energy (E), electrons let out approximately 10^{13} times more synchrotron radiation than protons [28].

$$\frac{\Delta E_e}{\Delta E_p} \approx \left(\frac{m_p}{m_e} \right)^4 \approx 10^{13} \quad (2.5)$$

The large energy loss due to synchrotron radiation limits the energies electrons can achieve in the LHC and is why LHC uses protons when running experiments [5].

Two important quantities used in particle physics experiments are luminosity (\mathcal{L}) and cross section (σ). Cross section is an area, but also a probability. The cross section is the area active in the scattering. The unit for cross section is barn (b), where $1 \text{ b} = 10^{-24} \text{ cm}^2 = 100 \text{ fm}^2$. Luminosity \mathcal{L} is defined as the number of collisions per area per time, or as the number of events per unit cross section that take place in a single beam encounter region per unit time. The units are $\text{cm}^{-2}\text{s}^{-1}$, as can be seen in eq. 2.6 that shows how the number of events per time \dot{N} relates to the luminosity.

$$\dot{N} = \mathcal{L}\sigma \quad (2.6)$$

In a collider where two bunches of particles collide head on and with N_1 and N_2 particles respectively, luminosity can be determined using eq. 2.7. If the bunches collide with a frequency f and have area A, then the luminosity is given by [28]:

$$\mathcal{L} = \frac{N_1 N_2 f}{A} \quad (2.7)$$

In the LHC there are a several bunches in each beam and they collide at an angle, not head on. The distributions of particles are Gaussian in each direction which must be taken into account. When calculating \mathcal{L} eq. 2.7 must then be expanded to:

$$\mathcal{L} = \frac{N_b N_1 N_2 f}{4\pi\sigma_x\sigma_y} S \quad (2.8)$$

Where N_b is the number of bunches, σ_x and σ_y are the width of the beam in the directions and S describe the angle at which the beams cross. The luminosity of the LHC has been calculated to be $10^{34} \text{ cm}^{-2} \text{ s}^{-1}$ according to [8].

The reason for colliding two beams, instead of one beam and a stationary target, is the center of mass (c.o.m.) energy. The stationary target collision would have a higher number of collision but the c.o.m. energy is smaller. For collisions with two beams of energy E , the c.o.m. energy becomes $2E$, but for the stationary target with mass m the c.o.m. energy becomes $\sqrt{2Em}$. Therefore a doubling of beam energy will multiply the energy by two in the beam collision, but only multiply by $\sqrt{2}$ in stationary target collisions. Higher energies make more massive particles as shown by Einstein's equation: $E^2 = m^2c^4 + p^2c^2$.

The cross section can be found with eq. 2.6. By integrating \dot{N} and \mathcal{L} over time one gets the number of events, N , and the integrated luminosity, L , and eq. 2.6 becomes:

$$\sigma = \frac{N}{L} \quad (2.9)$$

Where $N = \int \dot{N} dt$ and $L = \int \mathcal{L} dt$. When finding the cross section for an experiment where a particle decays, like $H \rightarrow e^+e^-$, one needs the efficiency of finding the decay, ϵ , and the number of particles that the experiment is looking at, $N = N_{data} - N_{background}$. This cross section will be the effective cross section σ_{eff} .

$$\sigma_{eff} = \frac{N_{data} - N_{background}}{\epsilon L} \quad (2.10)$$

2.3 The ATLAS Detector

The ATLAS detector is the largest detector at LHC [7]. It consists of an inner tracking detector, a thin superconducting solenoid, electromagnetic and hadronic calorimeters, and a muon spectrometer. These layers of detectors have specific tasks, such as momentum and energy measurements, and are ordered to maximize the number of particles that are measured before they are absorbed by the detector [9].

The Inner Tracking Detector (ID) finds the point of the proton collision and any secondary vertices where short-lived particles decay, f. ex the Higgs boson. The magnetic field bend the path of charged particles. The bending radius is proportional to the momentum of the charged particles. After the Inner Detector (ID) comes the calorimeters that measures the energy of different particles. These calorimeters absorb most of the particles coming from a collision, making them deposit all their energy within the detector. Outside of the calorimeters are the muon detectors. Muons don't lose much energy to bremsstrahlung because of their higher mass and that they don't interact with the hadronic calorimeter. Since muons have higher penetrating power than other particles, it is assumed that most of the particles that interact with the muon detector must be muons. The detectors are explained in more detail in the next sections.

2.3.1 The Inner Detector

The Inner Tracking Detector consists of three different sub-detectors, the pixel detector, Semiconductor Tracker (SCT) and Transition Radiation Tracker (TRT) [13]. Outside of the Inner Detector there is a 2 T solenoidal magnetic field parallel to the beam axis [15]. The Inner Detector set up can be seen in figure 2.1.

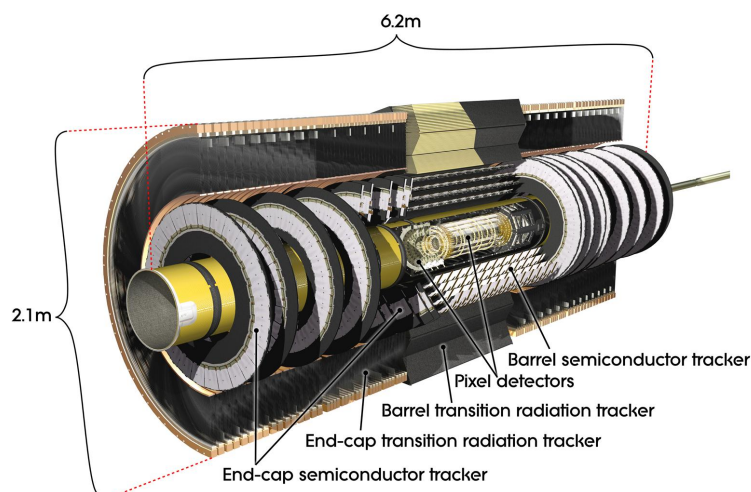


Figure 2.1: Inner Detector of ATLAS [13].

The pixel detector is the innermost part of the detector and is designed to give a high-granularity, high-precision measurements as close to the interaction point as possible. It consists of three barrels located 4 cm, 11 cm and 14 cm from the interaction point and four endcaps on each side [13]. These barrels give three very precise position measurements. This gives the Inner Detector the ability to find short-lived particles such as the τ -lepton. The pixel detector has 92 million pixels, each $50 \mu\text{m}$ in the $R\phi$ direction and $400 \mu\text{m}$ in the z direction [15]. Because the proximity to the collisions, the pixels must be very radiation hardened to withstand 300 kGy of ionising radiation in ten years of operation. An inner pixel layer was added in 2015, the IBL (Insertable Pixel Layer) [15].

The SCT is placed outside the pixel detector and consists of four barrels of silicon microstrip detectors and two endcaps with nine disks each [13]. Each of the modules is made of single-sided strip sensors glued back-to-back. The strips has 40 mrad between them. This gives two-dimensional information about the hits and the small angle minimise the fake hits in the detector [16]. The SCT has an area of 60 m^2 , compared to the pixel detectors 1.9 m^2 , and has 6 million channels, compared to the pixel detectors 92 million [13]. The pixel detector and the SCT work in a similar way, the absorbed energy makes free electrons, which are collected by electrodes.

The last part of the Inner Detector is the TRT. It consists of gas filled drift tubes, called straws, in a Barrel and endcaps. They are parallel to the beam pipe in the Barrel and radially in the endcaps [15]. The straws have a diameter of 4 mm with a 0.03 mm diameter gold-plated tungsten wire. In the Barrel there are 50 000 straws that are 144 cm long and in the end caps there are 250 000 straws, each 39 cm long. Each of these straws are read out separately [13]. The direction of the straws means that η can't be measured, but the transverse position of a charged particle. This means that the transverse momentum, p_T , can be measured. The TRT works in a different way to the pixel detector and the SCT. When a charged particle goes through a straw it ionizes the gas. The free electrons drift towards the wire and create an electric signal which is read out at the end of the straw [13].

2.3.2 Calorimeters

Calorimeters measure the energy of particles. The energy measurement is done by absorbing the particles, forcing them to deposit their energy and starting a particle shower. Calorimeters usually consist of passive and active layers. The passive layers absorb particles and create showers and the active layers read out the energy loss [17]. The active layers are scintillators that produce photons that are sent to photomultipliers. If the passive and active layers are distinct layers, this is called a sampling calorimeter. If the calorimeter is one material with both properties, then it is called a homogeneous calorimeter [18].

There are two main types of calorimeters, electromagnetic (EM) calorimeters that measure electrons and photons, and hadron calorimeters that measure hadrons [18]. Since hadrons pass through the EM calorimeter without being absorbed, the hadron calorimeter is placed after the EM calorimeter. In the EM calorimeter the shower starts when an electron or photon enters a material. At energies above 1 MeV, photons interact primarily through pair production and high-energy electrons emitting photons via bremsstrahlung [21]. In the hadron calorimeter the shower is made by a succession of inelastic hadronic interactions, mainly pion and nucleon production [20]. In ATLAS the calorimeter system consists of two parts, a liquid Argon (LAr) calorimeter and a tile calorimeter (TileCal) [17]. These calorimeter systems together absorb every particle except for muons and neutrinos.

The Liquid Argon (LAr) calorimeter is an EM calorimeter and consists of a barrel and two end caps. It is a sampling calorimeter, where lead is the passive layer and liquid Argon is the active layer. The liquid argon has to have a temperature of -183°C [17]. The LAr calorimeter uses an accordion geometry to give a full ϕ coverage without cracks.

The hadron calorimeter consists of a TileCal barrel and two LAr end caps. The TileCal is a sampling calorimeter that uses steel as the passive layer and scintillator tiles as the active layer. The photons produced by the scintillators are transported and read out by photomultipliers [17]. The hadronic LAr end caps and EM LAr end caps are similar but use copper instead of lead.

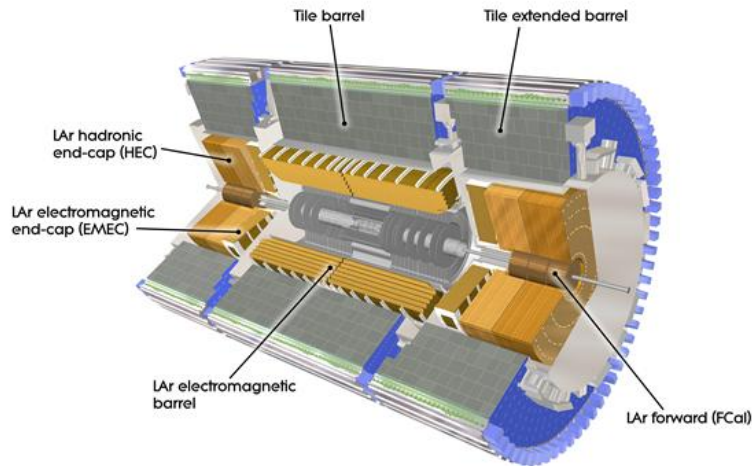


Figure 2.2: Calorimeter at ATLAS [20].

2.3.3 Muon spectrometer

Muons pass through the Inner Detector and calorimeters without interacting with the detector. Muons are much heavier than electrons and lose less energy through bremsstrahlung in the EM calorimeter and don't interact with the hadron calorimeter. Therefore, the muon spectrometer is placed outside of the calorimeters, where only the muons are measured. The muon spectrometer is the largest component of ATLAS and measures the momentum of muons similar to the Inner Detector, by bending their path in a magnetic field [22].

The muon spectrometer is made up of 4 000 muon chambers with four different methods of measuring the momentum, Monitored Drift Tubes (MDT), Cathode Strip Chambers (CSC), Thin Gap Chambers (TGC) and Resistive Plate Chambers (RPC). They are arranged as shown in 2.3 [22].

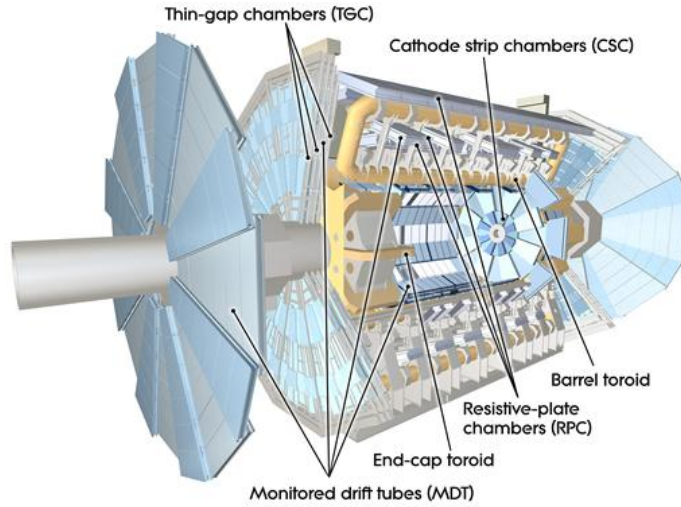


Figure 2.3: Muon spectrometer at ATLAS [23].

2.3.4 Coordinates

ATLAS uses a right-handed coordinate system with its origin at the point of collision in the centre of the detector and the z -axis along the beam pipe. The x -axis points from the collision point to the centre of the LHC ring, and the y -axis points upward. Cylindrical coordinates (r, ϕ) are used in the transverse plane, the x - y plane, where ϕ is the azimuthal angle around the beam pipe. Pseudorapidity, η is a spatial coordinate describing the angle of a particle relative to the beam axis, rather than using θ , and is defined by [12]:

$$\eta = -\ln \left[\tan \left(\frac{\theta}{2} \right) \right] \quad (2.11)$$

In the transverse plane, η is zero and along the beam, η goes to infinity, as seen in 2.4. Since high $|\eta|$ means shallow scattering angles, detectors must have a high η coverage, typical coverage extends to $|\eta| \approx 3$. In chapter 5.2 we will see that ATLAS has a $|\eta| < 2.7$ coverage for electrons, see fig. 5.1a. Pseudorapidity can also be written in terms of the momentum:

$$\eta = \frac{1}{2} \ln \left(\frac{|\mathbf{p}| + p_z}{|\mathbf{p}| - p_z} \right) \quad (2.12)$$

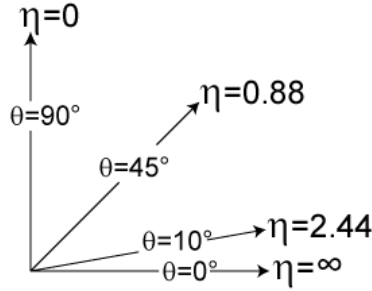


Figure 2.4: Pseudorapidity and theta [11]

Where $|\mathbf{p}|$ is the absolute value of the momentum and p_z is the momentum in the z -direction. For high energy particles where the masses is negligible, the substitution $E \approx |\mathbf{p}|$ holds and this leads to the pseudorapidity converging to rapidity:

$$y = \frac{1}{2} \ln \left(\frac{E + p_z}{E - p_z} \right) \quad (2.13)$$

For the high energies at the LHC this substitution holds [11]. The distance, ΔR between particles is measured in the (η, ϕ) plan and is defined as [12]:

$$\Delta R = \sqrt{(\Delta\eta)^2 + (\Delta\phi)^2} \quad (2.14)$$

Since both η and ϕ is Lorentz invariant if the particle is massless, ΔR is also Lorentz invariant.

2.4 Electron reconstruction and identification

There are many different types of particles that are created at the ATLAS detector and some of these decay into electrons. These final state electrons are important to identify in order to examine the Standard Model. To do this a likelihood-based (LH) identification electron selector is used. This LH selector combine a lot of variables and calculate a probability if the particle is an electron. Some working point cuts, that will be done in chapter 5, 6 and 7, use this LH selector to cut electron candidates [24].

The energy in the EM calorimeter, seen in fig. 2.2, is very important to identify electrons at high energies, $E > 20$ GeV . If there is high energy in the EM and energy in the hadron calorimeter, then it might be a charged pion

instead.

All of the working points, including the Loose working points that will be used in chapter 5, 6 and 7, require hits in the inner detector, seen in fig. 2.1. There must be at least 2 hits in the pixel detector and at least seven hits in the pixel and silicon-strip detector combined. For Medium and Tight working points there are more requirements that must be fulfilled [24].

Chapter 3

The Standard Model

The standard model is currently the model which best describe subatomic particles and their interactions. The basic constituents of matter are three families of point quarks and three of point leptons. There are also three basic non-gravitational gauge-type forces. The quarks interact through all three forces while the (charged) leptons interact only through the electromagnetic force and weak force. All three forces are carried by gauge bosons.

3.1 Notation

In SI units mass, length and time are natural dimensions. An alternative set of units commonly used in high energy physics, is natural units. In this unit system mass, action and velocity are fundamental dimensions. The reduced Planck constant, $\hbar = h/2\pi$, is used as a unit of action and the speed of light, c , is a unit of velocity. $c = \hbar = 1$ in natural units. In natural units the momentum-energy relations are:

$$E^2 = p^2 + m^2 \tag{3.1}$$

The introduction of the electron volt (eV) as a unit for energy requires some justification. One eV is the energy gained by an electron after being

accelerated by an electric potential difference of one volt.

$$\begin{aligned} 1\text{eV} &= 1.6 * 10^{-19}\text{C} \cdot 1\text{V} \\ &= 1.6 * 10^{-19}\text{J} \end{aligned}$$

The electron volt is a convenient energy unit since particles are often accelerated with electromagnetic fields. To explain why electron volts are used for mass and energy one uses eq. 3.1. This equation states that the total energy of a particle is dependent on the mass and momentum of the particle. For a massless particle eq. 3.1 reads:

$$E = p \tag{3.2}$$

and for a particle at rest we get the relation:

$$E = m \tag{3.3}$$

Since the unit of energy is eV, the unit for mass is also eV. 1 eV is a very small amount, so for the high energies made at the LHC, MeV and GeV are commonly used.

In relativistic quantum mechanics four-vectors are necessary to describe the different transformations. A general four-vector A will be written in terms of its contravariant index.

$$A = (A^\mu) = (A^0, \mathbf{A}) = (A^0, A^1, A^2, A^3) \tag{3.4}$$

Where A^0 is the time component and \mathbf{A} is the spatial components such that $\mathbf{A} = (A^i) = (A^1, A^2, A^3)$. The contravariant components A^1, A^2 and A^3 are physical components like A^x, A^y and A^z and the covariant components A_1, A_2 and A_3 will be related to the contravariant components. The four-position vector x is given by:

$$x = (x^\mu) = (x^0, \mathbf{x}) = (x^0, x^1, x^2, x^3) = (t, x, y, z) \tag{3.5}$$

$$x_\mu = \sum_{n=0}^3 g_{\mu\nu} x^\nu \equiv g_{\mu\nu} x^\nu \tag{3.6}$$

Where $g_{\mu\nu} = \text{diag}(1,-1,-1,-1)$. This gives:

$$x^2 = g_{\mu\nu}x^\nu x^\mu = x_\mu \cdot x^\mu = (x^0)^2 - \mathbf{x}^2 = t^2 - x^2 - y^2 - z^2 \quad (3.7)$$

Some other 4-vectors are the 4-momentum $(p^\mu) = (E, \mathbf{p})$ and the space-time analogue to the ∇ operator, $(\partial_\mu) = (\partial/\partial t, \nabla)$. All the different units can be seen in table 3.1. For example, the invariant mass of an unstable particles can be described by taking the square root of s , where s is:

$$\begin{aligned} s &= (p_1^\mu + p_2^\mu)^2 \\ &= (E_1 + E_2)^2 - (\mathbf{p}_1 + \mathbf{p}_2)^2 \\ &\approx 2p_1 p_2 (1 - \cos\theta) \end{aligned} \quad (3.8)$$

Table 3.1: Comparing SI and natural units

Quantity	Natural Units	SI
Velocity	c	m/s
Energy	eV	eV
Momumentum	eV	eV/c
Mass	eV	kg or eV/c ²
Time	1/eV	s
Length	1/eV	m

3.2 Elementary particles

In the Standard Model there are 17 elementary particles, divided into two categories: fermions and bosons. Fermions are spin 1/2 particles and make up the visible matter in the universe. There are 12 flavours of fermions divided into 2 groups, quarks and leptons, and these groups are again divided into 3 sub-groups called generations. Each generation has one up-type quark, one down-type quark, one negative charged lepton and one neutral lepton.

Table 3.2: Fermions

Type	Name	Symbol	Name	Symbol	Name	Symbol
Quark	Up	u	Charm	c	Top	t
	Down	d	Strange	s	Bottom	b
Lepton	Electron	e	Muon	μ	Tau	τ
	e-neutrino	ν_e	μ -neutrino	ν_μ	τ -neutrino	ν_τ

Bosons are spin 1 particles, except for the Higgs boson which has zero spin, and mediate the fundamental interactions of the weak interaction, the strong interaction and the electromagnetic interaction. Only particles with charge can feel the electromagnetic force. This happens through exchange of a massless boson called photon. Up-type quarks have an electrical charge of $+\frac{2}{3}e$, while the down-type quarks have a charge of $-\frac{1}{3}e$. The charged leptons, e , μ and τ have charge $+1e$. The neutrinos don't have a charge.

The quarks also have colour charge. The colour charges are red, green and blue. The strong force only works on coloured particles and is mediated by gluons. Unlike chargeless photons, gluons are coloured and they can therefore self-interact. Because of confinement only colour neutral particles can exist. This means that quarks and gluons can never be observed individually. A red, a green and a blue quark make a baryon and a quark and an anti-quark make a meson. Baryons and mesons are hadrons. The weak interaction is mediated by the neutral Z^0 boson and the two charged W^+ and W^- bosons. The high mass of Z^0 , W^+ and W^- means that the range of the weak interaction is small. The high mass of the weak bosons also made it difficult to observe them, they were not discovered until 1983, several years after they were postulated. The last boson is the Higgs boson. Unlike the other bosons, it has zero spin and does not mediate a force. The Higgs gives fermions and weak interaction bosons mass.

Table 3.3: Bosons and the forces

Force	Boson	Mass[Gev]	Charge [e]
Electromagnetism	γ	0	0
Weak	Z^0, W^\pm	91.19, 80.38	0, ± 1
Strong	g	0	0

3.3 Quantum Field Theory

In the 1920s, Dirac attempted to quantize the electromagnetic field. This was the beginning of quantum field theory. Then, in 1926, Born, Heisenberg and Jordan invented canonical quantization. Next, in 1927, Dirac created and presented the first reasonably complete theory of quantum electrodynamics (QED) and the following year he presented the Dirac equation. In addition, the same year Wigner found that the quantum field describing electrons or other fermions had to be expanded using anti-commutating creation and annihilation operators due to Pauli exclusion principle. Bethe, Dyson, Feynman, Schwinger and Tomonaga solved the so called 'divergence problem' through renormalization. This was the start of modern QED. In the 1950s Yang and Mills generalised QED to gauge theories - known as Yang-Mills theories. [25]

The Lagrangian density \mathcal{L} and the action S are important quantities in Quantum Field Theory (QFT). Usually, the Lagrangian density is called the Lagrangian. \mathcal{L} is define by:

$$\begin{aligned}\mathcal{L} &= \mathcal{L}(\phi, \partial_\mu\phi) \\ L &= \int \mathcal{L}d^3x \\ S &= \int Ldx^0 = \int \mathcal{L}d^4x\end{aligned}$$

Note that if \mathcal{L} is invariant under Lorentz transformations, then S is also invariant. The principle of least action $\delta S = 0$ gives:

$$\begin{aligned}0 &= \delta S = \delta \int \mathcal{L}(\phi, \partial_\mu\phi)d^4x \\ &= \int \left[\frac{\partial\mathcal{L}}{\partial\phi}\delta\phi - \partial_\mu \left(\frac{\partial\mathcal{L}}{\partial_\mu(\partial\phi)} \right) \delta\phi + \partial_\mu \left(\frac{\partial\mathcal{L}}{\partial_\mu(\partial\phi)}\delta\phi \right) \right] d^4x\end{aligned}\quad (3.9)$$

The last term in the integrand gives no contribution. Since $\delta\phi$ is an arbitrary variation on the field ϕ , eq. 3.9 leads to the equations of motion, i.e. the Euler-Lagrange field equations:

$$\frac{\partial\mathcal{L}}{\partial\phi} - \partial_\mu \left(\frac{\partial\mathcal{L}}{\partial_\mu(\partial\phi)} \right) = 0\quad (3.10)$$

Solving this equation gives the equations of motion for the field ϕ . Example of Lagrangians are:

$$\mathcal{L} = \bar{\psi}(x)(i\gamma^\mu\partial_\mu - m)\psi(x) \text{ for free electrons} \quad (3.11)$$

$$\mathcal{L} = -\frac{1}{4}F^{\mu\nu}F_{\mu\nu} \text{ for free photons} \quad (3.12)$$

Noether's theorem states that for every continuous symmetry of a local Lagrangian, there exist a conservation law, and hence, a conserved quantity [25]. A symmetry is a transformation in the following form:

$$x \rightarrow x' = x + \delta x \quad (3.13)$$

where δx is an arbitrary infinitesimal translation, like:

$$\delta\phi(x) = \phi'(x') - \phi(x) = \delta x^\mu\partial_\mu\phi(x) \quad (3.14)$$

The change induced on \mathcal{L} by such transformations is:

$$\delta\mathcal{L} = \frac{\partial\mathcal{L}}{\partial\phi}\delta\phi + \frac{\partial\mathcal{L}}{\partial(\partial_\mu\phi)}\delta\phi = \frac{\partial}{\partial x^\mu} \left(\frac{\partial\mathcal{L}}{\partial(\partial_\mu\phi)}\delta\phi \right) \quad (3.15)$$

If the lagragian \mathcal{L} is invariant under the transformation in eq. 3.14, then $\delta\mathcal{L} = 0$ and therefore the last equation becomes:

$$j^\mu = \frac{\partial\mathcal{L}}{\partial(\partial_\mu\phi)}\delta\phi \quad (3.16)$$

The Lagrangians must be invariant under such symmetries. This gives additional fields which couple to the original field, which are interpreted as the force carrying bosons. The symmetries come in groups described by group theory. These groups are local gauge transformation groups.

3.3.1 Group theory

A group is a set \mathcal{G} of elements together with a binary operator $*$ that combines any two elements a and b to form a third element denoted a*b. In order to qualify as a group, the set and operator $(\mathcal{G},*)$, must fulfill four requirements, which are called the group axioms [25]:

1. Closure: For all $a, b \in \mathcal{G}$, the result $a*b$ is also in \mathcal{G} .
2. Associativity: For all $a, b, c \in \mathcal{G}$, the condition $(a*b)*c=a*(b*c)$ holds.
3. Identity (or unit) element: There exists an element $e \in \mathcal{G}$ such that for every element $a \in \mathcal{G}$, the condition $e*a=a*e=a$ holds.
4. Inverse element: For each $a \in \mathcal{G}$, there exist an element $b \in \mathcal{G}$, usually denoted a^{-1} , such that $a*b=b*a=e$, where e is the identity element.

In physics Lie groups (or continuous groups) are an important class of groups. Lie groups are characterized by: (i) they can be parametrized by a finite number of parameters n and (ii) the quantity $a * b^{-1}$ is a continuous mapping with respect to these parameters [25]. The elements, g , of a Lie group parametrized by $\mathbf{t} = (t_1, t_2, \dots, t_n)$ and has the identity $e = (0, 0, \dots, 0)$ can be written as:

$$g = \exp(i\mathbf{A}\cdot\mathbf{t}), \text{ where } \mathbf{A}\cdot\mathbf{t} = \sum_{i=1}^n nA_i t_i \quad (3.17)$$

The A_i s are the infinitesimal generators of the group.

The unitary group, denoted $U(n)$, is the group of $n*n$ unitary matrices. An $n*n$ matrix U is said to be unitary if:

$$U^\dagger U = I_n \quad (3.18)$$

In the case of $n=1$, the group $U(1)$ corresponds to the circle group, consisting of all complex numbers with absolute value equal to one. This is the group of the electromagnetic interactions in the Standard Model. The special unitary group, denoted $SU(n)$, is the group of $n*n$ unitary matrices that also satisfies:

$$\det U = 1 \quad (3.19)$$

The dimension of a $SU(n)$ groups is $n^2 - 1$. The special unitary group have applications in the Standard Model. In particular, $SU(2)$ is the gauge group of weak interactions and $SU(3)$ is the gauge group of strong interactions. The group $SU(3) \oplus SU(2) \oplus U(1)$ is the gauge group of the Standard model and is a Lie group with dimension 12 ($8+3+1=12$). The dimensions of the

subgroups correspond to the eight gluons, the three vector bosons and the photon.

3.3.2 Quantum Electrodynamics

Quantum Electrodynamics (QED) explains electrodynamics on a quantum level, using quantum field theory. Classical electrodynamics tells that the electric and magnetic fields, \mathbf{E} and \mathbf{B} , can be explained by the vector field \mathbf{A} and the scalar field ϕ through:

$$\mathbf{E} = -\frac{\partial \mathbf{A}}{\partial t} - \nabla \phi, \quad \mathbf{B} = \nabla \times \mathbf{A} \quad (3.20)$$

Through some transformations of \mathbf{A} and ϕ , see eq. 3.21, \mathbf{E} and \mathbf{B} remain unchanged.

$$\phi \rightarrow \phi' = \phi + \frac{\partial f}{\partial t}, \quad \mathbf{A} \rightarrow \mathbf{A}' = \mathbf{A} + \nabla f \quad (3.21)$$

This is a $U(1)$ gauge symmetry. This can be rewritten as a four-potential

$$A_\mu \rightarrow A'_\mu = A_\mu + \partial_\mu f \quad (3.22)$$

Where the four-potential $A^\mu = (\phi, \mathbf{A})$. For non-relativistic quantum mechanics, the substitution eq. 3.23 for the free-particle Schrödinger equation leads to the correct wave equation for a particle with charge q in an electromagnetic field. This is known as the minimal substitution. A four-vector version of the minimal substitution takes the covariant form:

$$i\frac{\partial}{\partial t} \rightarrow i\frac{\partial}{\partial t} - q\phi, \quad -i\nabla \rightarrow -i\partial - p\mathbf{A} \quad (3.23)$$

$$\partial_\mu = \frac{\partial}{\partial x^\mu} \rightarrow D_\mu = [\partial_\mu + iqA_\mu] \quad (3.24)$$

To introduce the electromagnetic interaction into the free-fermion Lagrangian

$$\mathcal{L}_0 = \bar{\psi}(x)(i\gamma^\mu \partial_\mu - m)\psi(x) = \bar{\psi}(x)(i\cancel{\partial} - m)\psi(x) \quad (3.25)$$

through the minimal substitution eq. 3.24. We required invariance of the resulting Lagrangian:

$$\mathcal{L} = \bar{\psi}(x)(i\gamma^\mu D_\mu - m)\psi(x) = \mathcal{L}_0 - q\bar{\psi}(x)\gamma^\mu\psi(x)A_\mu(x) = \mathcal{L}_0 + \mathcal{L}_I \quad (3.26)$$

under the gauge transformations of the electromagnetic field:

$$A_\mu(x) \rightarrow A'_\mu(x) = A_\mu(x) + \partial_\mu f(x) \quad (3.27)$$

This invariance is ensured if, together with eq. 3.27, the fields $\psi(x)$ and $\bar{\psi}(x)$ undergo the transformations:

$$\begin{aligned} \psi(x) &\rightarrow \psi(x)' = \psi(x)e^{-iqf(x)} \\ \bar{\psi}(x) &\rightarrow \bar{\psi}(x)' = \bar{\psi}(x)e^{iqf(x)} \end{aligned} \quad (3.28)$$

Under these transformations the Lagrangian transforms according to:

$$\begin{aligned} \mathcal{L}_0 &\rightarrow \mathcal{L}_0 = \mathcal{L}_0 - q\bar{\psi}(x)\gamma^\mu\psi(x)\partial_\mu f(x) \\ \mathcal{L}_1 &\rightarrow \mathcal{L}_1 = \mathcal{L}_1 + q\bar{\psi}(x)\gamma^\mu\psi(x)\partial_\mu f(x) \end{aligned} \quad (3.29)$$

The resulting Lagrangian is thus invariant under $U(1)$ gauge transformations, giving the Lagrangian for electrodynamics:

$$\mathcal{L} = \bar{\psi}(x)(i\not{D} - m)\psi(x) - \frac{1}{4}F^{\mu\nu}F_{\mu\nu} \quad (3.30)$$

The free Lagrangian for a photon field A_μ has been included. Where the electromagnetic tensor is given by:

$$F^{\mu\nu} = \partial^\mu A^\nu - \partial^\nu A^\mu \quad (3.31)$$

3.3.3 Quantum Chromodynamics

For QED the gauge theory was a new way to look at already known interactions. The gauge theory for the strong interaction explained previously unknown interactions. This gauge theory is called quantum chromodynamics (QCD) because of the so-called colour charges. Hadrons are bound states of fundamental spin- $\frac{1}{2}$ quarks. In a simple quark model, baryon are made of three quarks and mesons are made of one quark and one anti-quark. This

is a good model to describe hadrons, but it has two inconsistent features. Firstly, free quark or 2 quark systems are never observed and secondly, the spin wavefunction of the baryons are symmetric under exchange of quarks of the same flavour, in apparent contradiction of the Pauli exclusion principle. Both phenomena are explained by the theory of colour, developed by Han, Nambu and Greenberg [25]. The assumption is that quarks, but not leptons, have one of three colour charges, red, green or blue. This gives the quark wavefunction:

$$\Psi = \psi\chi^c \quad (3.32)$$

Where ψ is the space/spin part and a colour wavefunction χ^c . For a single quark the colour wavefunction is denoted by the colour spinors $\chi^c = r, g, b$, where:

$$r = \begin{pmatrix} 1 \\ 0 \\ 0 \end{pmatrix} \quad g = \begin{pmatrix} 0 \\ 1 \\ 0 \end{pmatrix} \quad b = \begin{pmatrix} 0 \\ 0 \\ 1 \end{pmatrix} \quad (3.33)$$

similar to the spin wavefunction $\chi = \alpha, \beta$ is represented by Pauli spinors

$$\alpha = \begin{pmatrix} 1 \\ 0 \end{pmatrix} \quad \beta = \begin{pmatrix} 0 \\ 1 \end{pmatrix} \quad (3.34)$$

To explain why the free quark and two quark systems aren't observed the concept of colour confinement was introduced. Colour confinement says that only "colourless" hadrons can exist. A free quark must have a colour and two quarks can't neutralize each other. For a baryon there are three quarks so they can all have different colours and for a meson there are a quark and an anti-quark so these types of baryons can be colourless.

The free quark Lagrangian becomes:

$$\begin{aligned} \mathcal{L} = & \bar{\psi}_r^f(x)(i\cancel{\partial} - m)\psi_r^f(x) \\ & + \bar{\psi}_g^f(x)(i\cancel{\partial} - m)\psi_g^f(x) + \bar{\psi}_b^f(x)(i\cancel{\partial} - m)\psi_b^f(x) \end{aligned} \quad (3.35)$$

where a sum over the flavour index $f = u, d, s, c, b, t$ is understood. The dirac field $\psi_{r,g,b}^f$ corresponds to a quark of flavour f and colour r, g, b respectively

and can be combined into:

$$\Psi^f(x) = \begin{pmatrix} \psi_r^f(x) \\ \psi_g^f(x) \\ \psi_b^f(x) \end{pmatrix} \quad \bar{\Psi}^f(x) = (\bar{\psi}_r^f(x), \bar{\psi}_g^f(x), \bar{\psi}_b^f(x)) \quad (3.36)$$

The Lagrangian becomes:

$$\mathcal{L} = \bar{\Psi}^f(x)(i\cancel{D} - m)\Psi^f(x) \quad (3.37)$$

To introduce the strong interactions to the free quark Lagrangian use a very similar method as the one for QED. The first step is to introduce the local $SU(3)$ transformation:

$$\begin{aligned} \Psi^f(x) &\rightarrow \Psi^f(x)' = \exp[ig_s\lambda_j\omega_j(x)/2]\Psi^f(x) \\ \bar{\Psi}^f(x) &\rightarrow \bar{\Psi}^f(x)' = \bar{\Psi}^f(x)\exp[ig_s\lambda_j\omega_j(x)/2] \end{aligned} \quad (3.38)$$

where $\omega_j(x)$ ($j=0,1,2,\dots,8$) are arbitrary real differentiable functions, λ_j are three-dimensional analogues of the Pauli matrices and g_s is the coupling constant. The free quark Lagrangian is not invariant under these transformations and transforms as:

$$\mathcal{L}_0 \rightarrow \mathcal{L}'_0 = \mathcal{L}_0 - \frac{1}{2}g_s\bar{\Psi}^f(x)\lambda_j\cancel{D}\omega_j(x)\Psi^f(x) \quad (3.39)$$

for an infinitesimal $\omega_j(x)$. If as in QED, $\partial^\mu\Psi^f(x)$ was replaced by the covariant derivative:

$$D^\mu\Psi^f(x) = [\partial^\mu + ig_s\lambda_j A_j^\mu(x)/2]\Psi^f(x) \quad (3.40)$$

so that \mathcal{L}_0 transforms to:

$$\mathcal{L} = \bar{\Psi}^f(x)(i\cancel{D} - m)\Psi^f(x) = \mathcal{L}_0 + \mathcal{L}_I \quad (3.41a)$$

where:

$$\mathcal{L}_I = -\frac{1}{2}g_s\bar{\Psi}^f(x)\gamma_\mu\lambda_j\Psi^f(x)A_j^\mu(x) \quad (3.41b)$$

Here 8 real gauge fields $A_j^\mu(x)$ are introduced, gluon fields, since there are

8 conserved charges and $\omega_j(x)$. For eq. 3.41a to be invariant under the transformations in eq. 3.38 the transformations of the gluon fields $A_j^\mu(x)$ must be chosen so that the covariant derivatives $D^\mu\Psi^f(x)$ transform the same way as $\Psi^f(x)$ i.e.:

$$D^\mu\Psi^f(x) \rightarrow \exp[ig_s\lambda_j\omega_j(x)/2]D^\mu\Psi^f(x) \quad (3.42)$$

For infinitesimal functions $\omega_j(x)$ the transformations of the gluon fields are given by:

$$A_i^\mu(x) \rightarrow A_i^\mu(x)' = A_i^\mu(x) - \partial^\mu\omega_i(x) - g_s f_{ijk}\omega_j A_k^\mu(x) \quad (3.43)$$

where f_{ijk} are the structure constants. 3.41a and 3.43 are $SU(3)$ gauge transformations and any theory which is invariant under them is $SU(3)$ gauge invariant. For QED the term $-\frac{1}{4}F_{\mu\nu}F^{\mu\nu}$ describe a free photon. This term is gauge invariant. An analogous expression:

$$-\frac{1}{4}F_{i\mu\nu}(x)F_i^{\mu\nu}(x) \quad (3.44)$$

where:

$$F_i^{\mu\nu}(x) = \partial^\mu A_i^\nu(x) - \partial^\nu A_i^\mu(x) \quad (3.45)$$

would describe free massless gluons, but it is not invariant under gauge transformations because of the transformations in eq. 3.43. Eq. 3.44 will be gauge invariant by replacing $F_i^{\mu\nu}(x)$ by:

$$G_i^{\mu\nu}(x) = F_i^{\mu\nu}(x) + g_s f_{ijk}A_j^\mu(x)A_k^\nu(x) \quad (3.46)$$

This gives the free gluon Lagrangian:

$$\mathcal{L}_G = -\frac{1}{4}G_{i\mu\nu}(x)G_i^{\mu\nu}(x) \quad (3.47)$$

which is gauge invariant. This gives the QCD Lagrangian

$$\mathcal{L} = \bar{\Psi}^f(x)(i\not{D} - m)\Psi^f(x) - \frac{1}{4}G_{i\mu\nu}(x)G_i^{\mu\nu}(x) \quad (3.48)$$

There are some important differences between QED and QCD. The gluons themselves carry colour charge. This can be seen in eq. 3.46 where the second term indicates that the gluons interact with each other. Another difference is

that QCD describes the strong interaction, which is too strong for lowest order perturbation theory. The strong interaction is only strong at small distances and disappear for distances bigger than 1 fm. When one tries to separate a quark from a nucleus the potential energy builds uptill it is enough to create often several quark-antiquark pairs, leading to a spray of new particles, known as a jet. Colour confinement makes it impossible for colourless particles to exist.

3.3.4 Electroweak

The weak interaction is the force responsible for flavour change in elementary particles and radioactive decay of atoms, often through beta-decay. The electromagnetic and strong interactions is carried through massless, spin-1, gauge bosons. But the weak interaction is carried through three massive vector bosons, W^+ , W^- and Z^0 , the masses of these particles are:

$$M_W = 80.40 GeV \quad M_Z = 91.19 GeV \quad (3.49)$$

The high masses of these bosons have several consequences. The range of the weak interactions is of order 10^{-3} fm. The large energy needed to produce the W^\pm and Z^0 bosons in a laboratory meant that they were not discovered until 1983, long after they were theoretically predicted by Glashow, Salam and Weinberg's electroweak theory [25]. The weak interaction only works on left-handed particles. The left- and right-handed parts of a field is defined by:

$$\left. \begin{aligned} \psi^L &= P_L \psi(x) \\ \psi^R &= P_R \psi(x) \end{aligned} \right\} = \frac{1}{2}(1 \mp \gamma_5)\psi(x) \quad (3.50)$$

Furthermore, leptons are assumed to be massless. This gives the free lepton Lagrangian:

$$\mathcal{L}_0 = i[\bar{\psi}_l^L(x)\not{\partial}\psi_l^L(x) + \bar{\psi}_{\nu_l}^L(x)\not{\partial}\psi_{\nu_l}^L(x) + \bar{\psi}_l^R(x)\not{\partial}\psi_l^R(x) + \bar{\psi}_{\nu_l}^R(x)\not{\partial}\psi_{\nu_l}^R(x)] \quad (3.51)$$

Where a sum over the flavour index $l = e, \mu, \tau$ is understood. Since only left-handed particles interact with the weak force, one can combine the left-handed

fields into the two-component fields:

$$\Psi_l^L(x) = \begin{pmatrix} \psi_{\nu_l}^L(x) \\ \psi_l^L(x) \end{pmatrix} \quad \bar{\Psi}_l^L(x) = (\bar{\psi}_{\nu_l}^L(x), \bar{\psi}_l^L(x)) \quad (3.52)$$

With these fields, 3.51 becomes:

$$\mathcal{L}_0 = i[\bar{\Psi}_l^L(x) \not{D} \Psi_l^L(x) + \bar{\psi}_l^R(x) \not{\partial} \psi_l^R(x) + \bar{\psi}_{\nu_l}^R(x) \not{\partial} \psi_{\nu_l}^R(x)]. \quad (3.53)$$

To make electroweak gauge theory one introduce $SU(2)$ and $U(1)$ gauge transformations. Like in QED, the introduction of gauge fields generates the interaction. First the $SU(2)$ transformations:

$$\begin{aligned} \Psi_l^L(x) &\rightarrow \Psi_l^L(x)' = \exp[ig\tau_j\omega_j(x)/2] \Psi_l^L(x) \\ \bar{\Psi}_l^L(x) &\rightarrow \bar{\Psi}_l^L(x)' = \bar{\Psi}_l^L(x) \exp[-ig\tau_j\omega_j(x)/2] \\ \psi_l^R(x) &\rightarrow \psi_l^R(x)' = \psi_l^R(x), \quad \psi_{\nu_l}^R(x) \rightarrow \psi_{\nu_l}^R(x)' = \psi_{\nu_l}^R(x) \\ \bar{\psi}_l^R(x) &\rightarrow \bar{\psi}_l^R(x)' = \bar{\psi}_l^R(x), \quad \bar{\psi}_{\nu_l}^R(x) \rightarrow \bar{\psi}_{\nu_l}^R(x)' = \bar{\psi}_{\nu_l}^R(x) \end{aligned} \quad (3.54)$$

where $\omega_j(x)$, $j=1, 2, 3$, are arbitrary real differentiable functions and g is a coupling constant. By applying the transformations in eq. 3.54 to the free lepton Lagrangian in eq. 3.53 for a infinitesimal $\omega_j(x)$ transforms like:

$$\mathcal{L}_0 \rightarrow \mathcal{L}'_0 = \mathcal{L}_0 - \frac{1}{2} g \bar{\Psi}_l^L(x) \tau_j \not{\partial} \omega_j(x) \Psi_l^L(x) \quad (3.55)$$

If, like in QED, $\partial^\mu \Psi_l^L(x)$ was replaced by the covariant derivative:

$$D^\mu \Psi_l^L(x) = [\partial^\mu + ig\tau_j W_j^\mu(x)/2] \Psi_l^L(x) \quad (3.56)$$

so that \mathcal{L}_0 transforms to

$$\mathcal{L}_0 = i[\bar{\Psi}_l^L(x) \not{D} \Psi_l^L(x) + \bar{\psi}_l^R(x) \not{\partial} \psi_l^R(x) + \bar{\psi}_{\nu_l}^R(x) \not{\partial} \psi_{\nu_l}^R(x)] \quad (3.57)$$

For this modified Lagrangian to be invariant under the transformations in eq. 3.54 then the covariant derivative $D^\mu \Psi_l^L(x)$ must transform like the fields $\Psi_l^L(x)$:

$$D^\mu \Psi_l^L(x) \rightarrow \exp[ig\tau_j\omega_j(x)/2] D^\mu \Psi_l^L(x) \quad (3.58)$$

for an infinitesimal $\omega_j(x)$ the gauge fields $W_j^\mu(x)$ must transform like:

$$W_i^\mu(x) \rightarrow W_i^\mu(x)' = W_i^\mu(x) - \partial^\mu \omega_i(x) - g\epsilon_{ijk}\omega_j(x)W_k^\mu(x). \quad (3.59)$$

eq. 3.54 and eq. 3.59 are the $SU(2)$ gauge transformations of electroweak interaction. The $U(1)$ transformations for electroweak are almost identical to the $U(1)$ of QED. Instead of the charge q and field $A_\mu(x)$ in QED, electroweak uses the weak hyper charge Y and the field $B_\mu(x)$ and a coupling constant g' .

$$\begin{aligned} \psi(x) &\rightarrow \psi(x)' = \exp[ig'Yf(x)]\psi(x) \\ \bar{\psi}(x) &\rightarrow \bar{\psi}(x)' = \bar{\psi}(x)\exp[-ig'Yf(x)] \\ \partial^\mu \psi(x) &\rightarrow D^\mu \psi(x) = [\partial^\mu + ig'YB^\mu(x)]\psi(x) \\ B^\mu(x) &\rightarrow B^\mu(x)' = B^\mu(x) - \partial^\mu f(x) \end{aligned} \quad (3.60)$$

By the $SU(2)$ transformations in eq. 3.54 and eq. 3.59 and the $U(1)$ transformation in eq. 3.60 on the free lepton Lagrangian in eq. 3.53, one gets:

$$\mathcal{L}^L = i[\bar{\Psi}_l^L(x)\not{D}\Psi_l^L(x) + \bar{\psi}_l^R(x)\not{D}\psi_l^R(x) + \bar{\psi}_{\nu_l}^R(x)\not{D}\psi_{\nu_l}^R(x)] \quad (3.61)$$

where:

$$\begin{aligned} D^\mu \Psi_l^L(x) &= [\partial^\mu + ig\tau_j W_j(x)/2 - ig'B^\mu(x)/2]\Psi_l^L(x) \\ D^\mu \psi_l^R(x) &= [\partial^\mu - ig'B^\mu(x)/2]\psi_l^R(x) \\ D^\mu \psi_{\nu_l}^R &= \partial^\mu \psi_{\nu_l}^R \end{aligned} \quad (3.62)$$

To ensure invariance under these transformations four gauge fields are introduced, $B(x)$ form the $U(1)$ transformation and three $W_i(x)$ form the $SU(2)$ transformations. These bosons give rise to a free boson Lagrangians:

$$\mathcal{L}^B = -\frac{1}{4}B_{\mu\nu}(x)B^{\mu\nu}(x) - \frac{1}{4}G_{i\mu\nu}(x)G_i^{\mu\nu}(x) \quad (3.63)$$

where:

$$B^{\mu\nu}(x) = \partial^\nu B^\mu(x) - \partial^\mu B^\nu(x) \quad (3.64)$$

$$F_i^{\mu\nu}(x) = \partial^\nu W_i^\mu(x) - \partial^\mu W_i^\nu(x) \quad (3.65)$$

$$G_i^{\mu\nu} = F_i^{\mu\nu}(x) + g\epsilon_{ijk}W_j^\mu(x)W_k^\nu(x) \quad (3.66)$$

These four fields combine, through spontaneous symmetry breaking, into W^\pm , Z^0 and γ .

$$\begin{aligned} W_\mu^\pm &= \frac{1}{\sqrt{2}}(W_{1\mu} \mp iW_{2\mu}) \\ W_{3\mu}(x) &= \cos\theta_W Z_\mu(x) + \sin\theta_W A_\mu(x) \\ B_\mu(x) &= -\sin\theta_W Z_\mu(x) + \cos\theta_W A_\mu(x) \end{aligned} \tag{3.67}$$

where θ_W is the weak mixing angle or Weinberg angle. Quarks are also affected by the weak interaction. Like the two-component spinors with leptons and neutrinos, each of the three quark generations has an up- and down-type which make up two-component spinors. To get these fields we had to assume that all leptons and quarks are massless. To reintroduce these masses, the Higgs mechanism must be introduced.

3.4 The Higgs Boson

In the last section a gauge theory for the electromagnetic and weak interaction was introduced. To make these interactions, all leptons, quarks and gauge bosons must have zero mass, but only photons and gluons are massless. To add the masses back to the Lagrangian, the mechanism of spontaneous symmetry breaking is introduced. Spontaneous symmetry breaking is when at low energy a system has a preferred direction, while at higher energy all directions are symmetric. Like a pencil standing on its end, the state of the system will eventually fall into another state for which the potential energy of the system has a local minimum [27]. Ferromagnetism is a famous example of spontaneous symmetry breaking. At higher temperatures there is no magnetism in the system because the forces that couple the spins of the system are rotationally invariant. However, the spins are aligned at low temperatures which makes the ferromagnet magnetic.

In field theory spontaneous symmetry breaking is only relevant if the vacuumstate is non-unique. This was first suggested by Nambu and his co-workers. If the vacuum states are required to be invariant under Lorentz transformations, then the field must be a scalar field, $\phi(x)$, and the vacuum expectation value must be:

$$\langle 0|\phi(x)|0 \rangle = c \neq 0 \tag{3.68}$$

unlike the vacuum expectation values for a spinor field $\psi(x)$ and vector field $V^\mu(x)$, where:

$$\langle 0|\psi(x)|0 \rangle = 0, \quad \langle 0|V^\mu(x)|0 \rangle = 0 \quad (3.69)$$

The Goldstone model is the simplest field theory exhibiting spontaneous symmetry breaking. Its Lagrangian is:

$$\mathcal{L}(x) = [\partial^\mu \phi^*(x)][\partial_\mu \phi(x)] - \mu^2 |\phi(x)|^2 - \lambda |\phi(x)|^4 \quad (3.70)$$

where $\phi(x)$ is a complex scalar field:

$$\phi(x) = \frac{1}{\sqrt{2}}[\phi_1(x) + i\phi_2(x)] \quad (3.71)$$

The potential energy density of the field is given by:

$$\mathcal{V}(\phi) = \mu^2 |\phi(x)|^2 + \lambda |\phi(x)|^4 \quad (3.72)$$

and μ^2 and λ are real parameters. For the energy of the field to be bounded from below, then $\lambda > 0$. Two situations arise depending on the sign of μ^2 . For a positive μ^2 , $\mathcal{V}(\phi)$ has a unique value for $\phi(x) = 0$, therefore spontaneous symmetry breaking cannot occur. Negative μ^2 $\mathcal{V}(\phi)$ has a local positive for $\phi(x) = 0$ and a circle of minima at:

$$\phi(x) = \phi_0 = \left(\frac{-\mu^2}{2\lambda} \right)^{1/2} e^{i\theta}, \quad 0 \leq \theta < 2\pi \quad (3.73)$$

where θ is the direction in the complex $\phi(x)$. Since there is not a unique vacuum state, spontaneous symmetry breaking will occur for a significant direction θ . Picking $\theta = 0$ gives a purely real solution:

$$\phi_0 = \left(\frac{-\mu^2}{2\lambda} \right)^{1/2} = \frac{1}{\sqrt{2}}v \quad (3.74)$$

By introducing two real fields $\sigma(x)$ and $\eta(x)$, $\phi(x)$ can be written as:

$$\phi(x) = \frac{1}{\sqrt{2}}[v + \sigma(x) + i\eta(x)] \quad (3.75)$$

and the Lagrangian becomes:

$$\begin{aligned} \mathcal{L}(x) = & \frac{1}{2}[\partial^\mu\sigma(x)][\partial_\mu\sigma(x)] - \frac{1}{2}(2\lambda v^2)\sigma^2(x) + \frac{1}{2}[\partial^\mu\eta(x)][\partial_\mu\eta(x)] \\ & - \lambda v\sigma(x)[\sigma^2(x) + \eta^2(x)] - \frac{1}{4}\lambda[\sigma^2(x) + \eta^2(x)]^2 \end{aligned} \quad (3.76)$$

The first three terms in this Lagrangian have quadratic $\sigma(x)$ and $\eta(x)$ terms and can be treated as the free Lagrangian and the remaining cubic and quadratic terms as interactions. The free Lagrangian shows that the $\sigma(x)$ and $\eta(x)$ fields are Klein Gordon fields of spin-0 particles. The $\sigma(x)$ boson has a mass of $\sqrt{2\lambda v^2}$, but since there are no $\eta^2(x)$ terms the η boson must have zero mass. These massless bosons are called Goldstone bosons, but no Goldstone bosons have been observed. The Higgs mechanism was introduced to solve this problem. By using the same fields and Lagrangian as in the Goldstone model and using a $U(1)$ gauge symmetry, a gauge boson field A^μ is introduced with the covariant derivative:

$$D_\mu\phi(x) = [\partial_\mu + iqA_\mu(x)]\phi(x) \quad (3.77)$$

and the free Lagrangian for the free boson field:

$$-\frac{1}{4}F_{\mu\nu}F^{\mu\nu} \quad (3.78)$$

where:

$$F_{\mu\nu} = \partial_\nu A_\mu - \partial_\mu A_\nu \quad (3.79)$$

The Lagrangian for the Higgs model then becomes:

$$\mathcal{L}(x) = [D^\mu\phi(x)][D_\mu\phi(x)] - \mu^2|\phi(x)|^2 - \lambda|\phi(x)|^4 - \frac{1}{4}F_{\mu\nu}F^{\mu\nu} \quad (3.80)$$

and is invariant for the $U(1)$ gauge transformations:

$$\begin{aligned} \phi(x) & \rightarrow \phi(x)' = \phi(x)e^{-iqf(x)} \\ \phi^*(x) & \rightarrow \phi^*(x)' = e^{iqf(x)}\phi^*(x) \\ A_\mu(x) & \rightarrow A_\mu(x)' = A_\mu(x) + \partial_\mu f(x) \end{aligned} \quad (3.81)$$

Like in the Goldstone model to keep the energy bounded from below, λ

must be positive. There are now two situations that can arise. For $\mu^2 > 0$ spontaneous symmetry breaking cannot occur. For $\mu^2 < 0$ the vacuum states are not unique, leading to spontaneous symmetry breaking. And like in the Goldstone model the real value for ϕ_0 is chosen and two real fields $\sigma(x)$ and $\eta(x)$ are chosen. In these fields the Lagrangian becomes:

$$\begin{aligned}
 \mathcal{L}(x) = & \frac{1}{2}[\partial^\mu \sigma(x)][\partial_\mu \sigma(x)] - \frac{1}{2}(2\lambda v^2)\sigma^2(x) \\
 & - \frac{1}{4}F_\mu \nu(x)F^\mu \nu(x) + \frac{1}{2}(qv)^2 A_\mu(x)A^\mu(x) \\
 & + \frac{1}{2}[\partial^\mu \eta(x)][\partial_\mu \eta(x)] \\
 & + qvA^\mu(x)\partial_\mu \eta(x) + \text{'interaction terms'}
 \end{aligned} \tag{3.82}$$

where the interactions terms are cubic and quadratic of $\sigma(x)$ and $\eta(x)$. The first line in eq. 3.82 describes a real Klein-Gordon field which gives an uncharged spin-0 boson with mass $\sqrt{2\lambda v^2}$. However the term $qvA^\mu(x)\partial_\mu \eta(x)$ on the fourth line in eq. 3.82 shows that A^μ and η can't be separate fields. This can be solved by expressing $\phi(x)$ as:

$$\phi(x) \rightarrow \phi(x)' = \phi(x)e^{-i\theta(x)/v} = \frac{1}{\sqrt{2}}(v + H(x)) \tag{3.83}$$

and the gauge field A^μ as:

$$A_\mu(x) \rightarrow A'_\mu(x) = A_\mu(x) + \frac{\partial_\mu \theta(x)}{v} \tag{3.84}$$

The gauge in which $\phi \rightarrow \phi'$ and $A^\mu \rightarrow A'^\mu$ is called the unitary gauge. By choosing $\theta = 0$ the η field is eliminated from 3.82 and transforms $\phi(x)$ becomes:

$$\phi(x) = \frac{1}{\sqrt{2}}(v + H(x)) \tag{3.85}$$

In this gauge the Lagrangian becomes:

$$\begin{aligned}
 \mathcal{L} = & \frac{1}{2}[\partial^\mu H(x)][\partial_\mu H(x)] - \frac{1}{2}(2\lambda v^2)H^2(x) \\
 & - \frac{1}{4}F_{\mu\nu}F^{\mu\nu} + \frac{1}{2}(qv)^2 A_\mu(x)A^\mu(x) \\
 & - \lambda v H^3(x) - \frac{1}{4}\lambda H^4(x) \\
 & - \frac{1}{2}A_\mu(x)A^\mu(x)[2vH(x) + H^2(x)]
 \end{aligned} \tag{3.86}$$

The first two lines are the free particle Lagrangian for a real Klein-Gordon field $H(x)$ and a real vector field $A_\mu(x)$. The scalar boson $H(x)$ has a mass of $\sqrt{2\lambda v^2}$ and is called the Higgs Boson. The third and fourth line show that the Higgs field $H(x)$ interacts with itself and the gauge field $A_\mu(x)$. The Higgs mechanism also has no Goldstone boson as the degree of freedom $\eta(x)$ is "eaten" by the field $A_\mu(x)$.

In section 3.3 a Lagrangian model for electroweak interactions with massless leptons and gauge bosons was introduced, shown in eq. 3.87.

$$\mathcal{L} = \mathcal{L}^L + \mathcal{L}^B \tag{3.87}$$

where \mathcal{L}^L and \mathcal{L}^B are described in eq. 3.61 and eq. 3.63, respectively. To give masses to the bosons, the Higgs mechanism is used. To break the $SU(2)$ symmetry a weak isospin doublet $\Phi(x)$ is introduced:

$$\Phi(x) = \begin{pmatrix} \phi_a(x) \\ \phi_b(x) \end{pmatrix} \tag{3.88}$$

where $\phi_a(x)$ and $\phi_b(x)$ are scalar fields. Φ transforms under $SU(2) \times U(1)$ gauge transformations. Φ transforms as shown in eq. 3.54, resulting in eq. 3.89:

$$\begin{aligned}
 \Phi(x) & \rightarrow \Phi'(x) = \exp[ig\tau_j\omega_j(x)/2]\Phi(x) \\
 \Phi^\dagger(x) & \rightarrow \Phi^\dagger(x)' = \Phi^\dagger(x)\exp[-ig\tau_j\omega_j(x)/2]
 \end{aligned} \tag{3.89}$$

and as shown in eq. 3.60:

$$\begin{aligned}
 \Phi(x) & \rightarrow \Phi'(x) = \exp[ig'Yf(x)]\Phi(x) \\
 \Phi^\dagger(x) & \rightarrow \Phi^\dagger(x)' = \Phi^\dagger(x)\exp[-ig'Yf(x)]
 \end{aligned} \tag{3.90}$$

This gives the Lagrangian:

$$\mathcal{L}^H(x) = [D^\mu \Phi(x)]^\dagger [D_\mu \Phi(x) - \mu^2 \Phi^\dagger(x) \Phi(x) - \lambda [\Phi^\dagger(x) \Phi(x)]^2] \quad (3.91)$$

where the covariant derivative $D^\mu \Phi(x)$ is defined by:

$$D^\mu \Phi(x) = [\partial^\mu + ig\tau_j W_J^\mu(x)/2 + ig'Y B^\mu(x)] \Phi(x) \quad (3.92)$$

By choosing the isospinor to be:

$$\Phi(x) = \frac{1}{\sqrt{2}} \begin{pmatrix} 0 \\ v + H(x) \end{pmatrix} \quad (3.93)$$

the terms $\mathcal{L}^B + \mathcal{L}^H$ becomes:

$$\begin{aligned} \mathcal{L}^B + \mathcal{L}^H = & -\frac{1}{4} F_{\mu\nu} F^{\mu\nu} \\ & -\frac{1}{2} F_{W\mu\nu}^\dagger F_W^{\dagger\mu\nu} + m_W^2 W_\mu^\dagger W^\mu \\ & -\frac{1}{4} Z_{W\mu\nu} F^{\dagger\mu\nu} + m_Z^2 Z_\mu Z^\mu \\ & +\frac{1}{2} (\partial^\mu H)(\partial_\mu H) - m_H^2 H^2 \\ & + \mathcal{L}_I^{BB} + \mathcal{L}_I^{HH} + \mathcal{L}_I^{HB} \end{aligned} \quad (3.94)$$

where $\mathcal{L}_I^{BB} + \mathcal{L}_I^{HH} + \mathcal{L}_I^{HB}$ are interaction terms. The masses m_W, m_Z and m_H are defined as:

$$m_W = \frac{1}{2}vg, \quad m_Z = \frac{m_W}{\cos\theta_W}, \quad m_H = \sqrt{-2\mu^2}. \quad (3.95)$$

By using eq. 3.94 and eq. 3.95 the Higgs boson, Z^0 and W^\pm have gotten masses. To give masses to the leptons, the lepton and Higgs fields are coupled through Yukawa interactions. This gives the Lagrangian:

$$\begin{aligned} \mathcal{L}^{LH}(x) = & -g_l [\bar{\Psi}_l^L(x) \Phi(x) \psi_l^R + \bar{\psi}_l^R(x) \Phi^\dagger(x) \Psi_l^L] \\ & -g_{\nu_l} [\bar{\Psi}_l^L(x) \tilde{\Phi}(x) \psi_{\nu_l}^R + \bar{\psi}_{\nu_l}^R(x) \tilde{\Phi}^\dagger(x) \Psi_l^L] \end{aligned} \quad (3.96)$$

where $\tilde{\Phi}(x)$ is defined by:

$$\tilde{\Phi}(x) = -i[\Phi^\dagger(x)\tau_2]^T = \begin{pmatrix} \phi_b^*(x) \\ -\phi_a^*(x) \end{pmatrix} \quad (3.97)$$

The terms $\mathcal{L}^L + \mathcal{L}^{LH}$ give the free lepton Lagrangian and some additional interaction terms:

$$\mathcal{L}^L + \mathcal{L}^{LH} = \bar{\psi}_l(i\cancel{\partial} - m_l)\psi_l + \bar{\psi}_{\nu l}(i\cancel{\partial} - m_l)\psi_{\nu l} + \mathcal{L}_I^{LB} + \mathcal{L}_I^{HL} \quad (3.98)$$

The masses m_l and $m_{\nu l}$ are defined by:

$$m_l = \frac{vg_l}{\sqrt{2}}, \quad m_{\nu l} = \frac{vg_{\nu l}}{\sqrt{2}}. \quad (3.99)$$

Eq. 3.94 and eq. 3.98 combine to give the complete Lagrangian of the standard electroweak theory:

$$\mathcal{L} = \mathcal{L}_0 + \mathcal{L}_I \quad (3.100)$$

where:

$$\begin{aligned} \mathcal{L}_0 = & \bar{\psi}_l(i\cancel{\partial} - m_l)\psi_l + \bar{\psi}_{\nu l}(i\cancel{\partial} - m_l)\psi_{\nu l} \\ & - \frac{1}{4}F_{\mu\nu}F^{\mu\nu} \\ & - \frac{1}{2}F_{W\mu\nu}^\dagger F_W^{\dagger\mu\nu} + m_W^2 W_\mu^\dagger W^\mu \\ & - \frac{1}{4}Z_{W\mu\nu}F_{\dagger\mu\nu} + m_Z^2 Z_\mu Z^\mu \\ & + \frac{1}{2}(\partial^\mu H)(\partial_\mu H) - m_H^2 H^2 \end{aligned} \quad (3.101)$$

and

$$\mathcal{L}_I = \mathcal{L}_I^{LB} + \mathcal{L}_I^{BB} + \mathcal{L}_I^{HH} + \mathcal{L}_I^{HB} + \mathcal{L}_I^{HL} \quad (3.102)$$

3.5 Higgs production at ATLAS

In July 2012, a particle consistent with the Standard Model (SM) Higgs boson was discovered. For energy over 100 GeV the most important mechanism for production of massive particles, like the Higgs boson, is by gluon-gluon fusion

[31]. To produce a Higgs boson two gluons interact, forming a top quark loop which again produce a Higgs boson. All fermions could make the loop, but since the top quarks are so heavy they interact more with the Higgs boson than any other fermion. Some other processes are boson fusions where top quark produce W^\pm or Z^0 which then produce the Higgs boson. This is called vector boson fusion (VBF) [31].

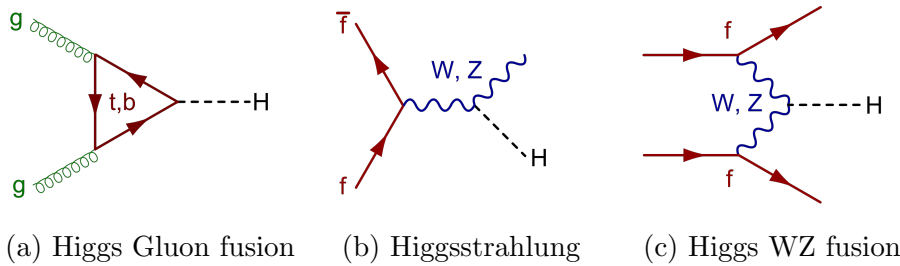


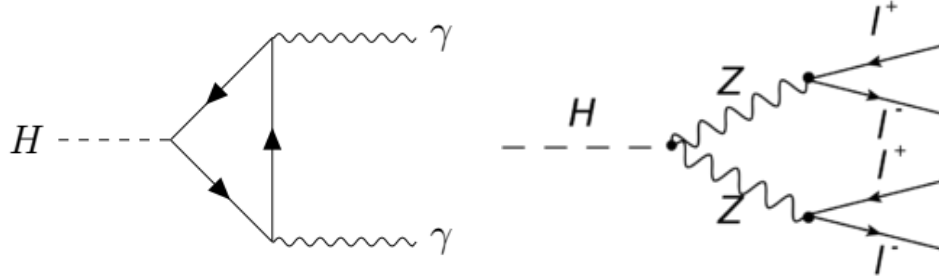
Figure 3.1: Ways that the Higgs boson is produced at the ATLAS detector [29]

The cross sections for Higgs production at a c.o.m energy of $\sqrt{(s)} = 13$ TeV is shown in table. 3.4. The combined cross section for Higgs production is 55.1 pb. When using eq. 2.9, with $\sigma = 55.1$ pb and $L = 139 \text{ fb}^{-1}$ [34], one gets that the number of Higgs bosons produced at the ATLAS detector is $N = 7.66 \cdot 10^6$.

Table 3.4: The cross sections for Higgs production at a c.o.m energy of $\sqrt{(s)} = 13$ TeV, in pb. [33].

	ggF	VBF	WH	ZH	ttH	Combined
Predicted						
cross section	$48.6^{+5\%}_{-5\%}$	$3.7^{+2\%}_{-2\%}$	$1.37^{+2\%}_{-2\%}$	$0.88^{+5\%}_{-5\%}$	$0.5^{+9\%}_{-13\%}$	55.1

The Higgs bosons decay vertices are proportional to the mass of the produced particles. For higher the mass of the particles, the higher cross section, so a bottom quark/antiquark pair are therefore the dominating decay mode, as seen in fig. 3.3. This decay mode is difficult to observe at the LHC because of the large background due to jets. The most important processes for identification of the Higgs are decay to two photons and to a ZZ^* pair, where both decay to a pair of electrons or muons.



(a) Higgs boson decay to two photons (b) Higgs boson decay to four lepton

Figure 3.2: Ways that the Higgs boson decay that is detected at the ATLAS detector [30]

60% of Higgs bosons decay into bottom quark/antiquark pairs, because bottom quarks are the heaviest particles that the Higgs boson can decay into. 5% of Higgs bosons decay into tau-antitau pairs [32]. To find the amount of Higgs that decay into e^+e^- one can use the ratio of the branching factors.

$$\begin{aligned} \frac{\Gamma(H \rightarrow e^+e^-)}{\Gamma(H \rightarrow \tau^+\tau^-)} &= \\ \frac{BR(H \rightarrow e^+e^-)}{BR(H \rightarrow \tau^+\tau^-)} &= \frac{m_e^2}{m_\tau^2} = \frac{0.511 \text{ MeV}^2}{1776.86 \text{ MeV}^2} = 8.27 * 10^{-8} \end{aligned} \quad (3.103)$$

The decay probability for $H \rightarrow e^+e^-$ becomes $5\% * \frac{m_e^2}{m_\tau^2} = 4.14 * 10^{-7} \%$. Using this with the number of Higgs produced at the ALTAS detector, $N = 7.66 * 10^6$, one gets that the number of times Higgs have decayed into e^+e^- is $N_{H \rightarrow e^+e^-} = N * 5\% * \frac{m_e^2}{m_\tau^2} = 0.003 \approx 0$. This tell us that that one does not expect to find any $H \rightarrow e^+e^-$ events in chapter 7 where real data is analysed.

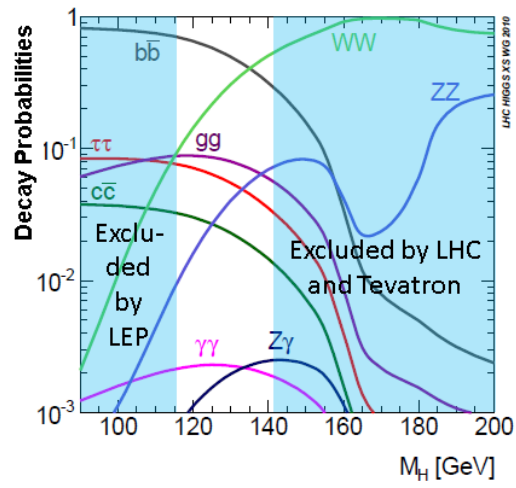


Figure 3.3: Decays of the Standard Model Higgs [32]

Chapter 4

Simulation

This chapter will give an introduction to the software used when analysing collision data from the ATLAS detector. Monte Carlo, simulated events, the ATHENA framework and different programming language will be described.

4.1 Monte Carlo

Before looking at real data from the ATLAS detector we will look at a simulated dataset, so we have something to compare the results with. These simulations can be used to determine background, efficiency and signal to background ratio. These simulated datasets are Monte Carlo simulations of proton-proton collisions at the ATLAS detector. Monte Carlo simulations generate random objects with the help of a computer, using the Law of Large Numbers as an advantage. This means that the error in the simulations goes as one over the square root of the number of events [38].

An example of what a Monte Carlo simulation can do is to find an approximation of π with generating random points inside a square. The Monte Carlo simulation generate points in a $1 \cdot 1$ square. Some of these points will be inside a quadrant with a radius of 1. The number of points inside the quadrant divided by the number of points inside the square will be $\frac{\frac{1}{4} \cdot \pi \cdot 1 \cdot 1}{1 \cdot 1} = \frac{\pi}{4}$. Then multiply the ratio by four to get an approximation of π . With more and more points the approximation becomes better and better.

4.1.1 Simulated events

The programs that create the MC simulations are called event generators. They calculate the collisions and the decay of different processes. Because of the many different processes, there are many different types of event generators. At first we will be looking at proton-proton collisions that make a Z boson which then decay into e^+e^- . A simulation of proton-proton collisions starts with a hard scattering of two partons, two gluons or a quark-antiquark pair. A Parton Distribution Function (PDF) determine the probability of the different partons to take part of the process. PDFs can be found experimentally. The particles from the initial scattering then make a Z boson which decay into e^+e^- . Min-bias is also added. Min-bias comes from the fact that in real collisions there are multiple collisions at once, the collisions that are not being studied are called minimum bias. The Z boson processes are generated with the Powheg-Box v2 Monte Carlo program interfaced to the Pythia 8.186 parton shower model [10].

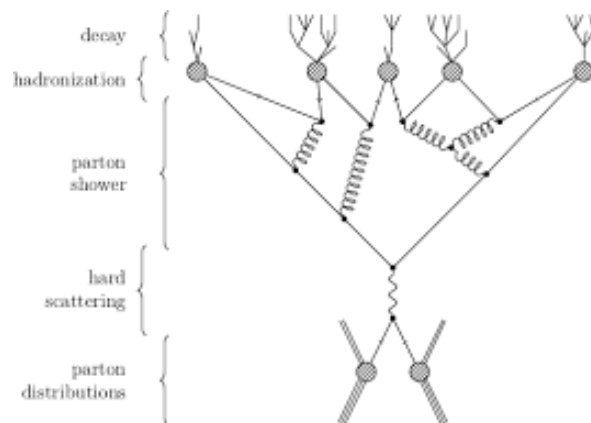


Figure 4.1: An example of how an event generator can simulate a proton proton collision [36]

An example of how the simulation works is shown in fig. 4.1. In this figure the process starts with a PDF and then a hard scattering of the particles. The outgoing particles create a parton shower where the different partons collide, interact and decay into other partons that then hadronize into different hadrons. The unstable hadrons then decay again into the final structure of the simulation.

4.1.2 Event Reconstruction

The event generators produce many particles with energy and momentum that move in different directions. These simulated particles then pass through a simulated detector. This means that the response of the ATLAS detector, when the simulated particles go through it, must be simulated. The simulated ATLAS detector response is done with Geant4 [10]. The simulated energy measured by the calorimeters and the hits measured in the inner detectors are stored like real detectors and can be reconstructed in the same way.

A schematic representation of the Full Chain Monte Carlo production can be seen in fig. 4.2. Here every step from the event generation to the Analysis Object Data (AOD) is shown. The square boxes are the different production processes and the circular boxes are the different types of outcomes. There are two ways from the event generation to an AOD. The first way is via the simulated detector and the second way is using the software Atlfast. Atlfast provides a simulation that "smear" the generated events to directly into an AOD [37].

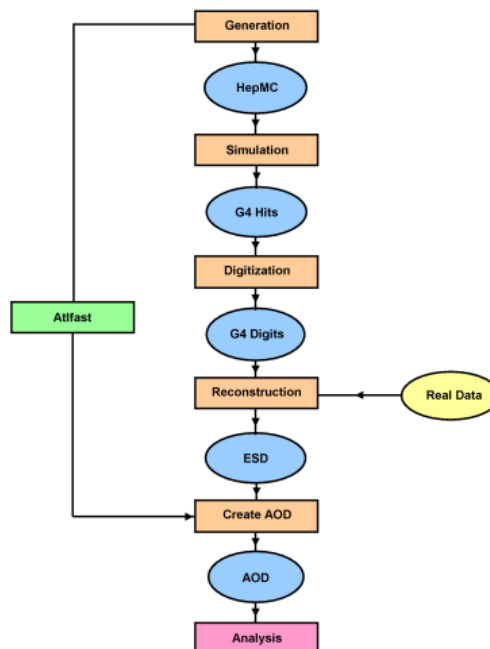


Figure 4.2: A schematic representation of the Full Chain Monte Carlo production [37]

4.2 The Grid

The Worldwide LHC Computing Grid, often called the Grid, was launched in 2002 to be a resource to store and analyse the large amounts of data generated at the LHC. The Grid is a global network of computers and storage systems in 42 countries and is based on the European Grid Infrastructure and the Open Science Grid in the USA. This makes it the largest computing network of its kind. The Grid has many advantages over a centralized system; there are multiple copies stored at different sites, no single point of failure can stop everything, the centers are spread over several time zones and the resources can be distributed across the world.

The Grid gives access to computing resources like storage and processing power. A user send a grid job request, for example to perform some analysis, then the Grid established the identity of the user, checks their credentials, and searches for available sites that can provide the resources requested. The user does not have to worry about where the computing resources are coming from, they can tap into the Grid's computing power and access storage on demand [39].

4.3 Athena and samples

The Athena Framework is a control framework. A framework is a skeleton application that developers can plug their code into that provides common functions and communication between different components. Athena is a implementation of the Gaudi framework. Gaudi was developed by LHCb, but now it is used at ATLAS, with ATLAS specific enhancements [42].

The processing of ATLAS data, like high-level trigger, reconstruction and analysis takes place in the Athena framework. This makes it easier for developers and users to test and run code because the geometry is the same and the data is read the same way for all types of applications [43].

4.3.1 ROOT

Root was developed at CERN by Rene Brun and Fons Rademakers in 1995. It is a framework that uses C++ to for mathematical and statistical analysis. ROOT has a C++ interpreter and libraries. The C++ interpreter makes

it possible to run scripts without compiling them. The libraries provide mathematical and statistical functions and tools that make it possible to do many complicated operations with simple commands.

ROOT is written in C++, but other languages like Python is integrated. PyROOT is a Python extension module that enables Python to interact with the ROOT libraries.

4.3.2 C++ and Python

C++ and Python are very important in particle physics. C++ is a object-oriented programming language created by Bjarne Stroustrup and is an extension of C. It is a low-level programming language, giving memory manipulation, and makes C++ flexible and robust, but makes it more difficult to learn. A C++ script also has to be compiled before running the code, but it is very fast when compiled. This is very useful when dealing with scripts with many calculations.

Python was designed by Guido van Rossum as a successor to ABC. Python is a high level programming language and it's design philosophy is code readability. This makes Python very used friendly. Unlike C++, Python is a interpreted language, so a Python script does not have to be compiled before running. This makes C++ faster than Python when working with complex scripts.

Chapter 5

Monte Carlo $Z \rightarrow e^+e^-$

In order to investigate $H \rightarrow e^+e^-$ decay, a mass reconstruction model must be developed using a known decay process. The $Z \rightarrow e^+e^-$ process is well understood, so large changes to decrease the background and increase the Z peak at 90 GeV can be done without forcing a Higgs peak at 125 GeV. In this chapter a mass reconstruction model using leading and sub-leading electrons will be developed using a simulated Monte Carlo $Z \rightarrow e^+e^-$ sample.

5.1 Sample

The samples used to develop the mass reconstruction model are Monte Carlo simulations of pp collisions producing Z bosons, which decayed into e^+e^- . The sample is made with Monte Carlo simulations of proton-proton collisions at $\sqrt{s} = 13$ TeV at the ATLAS detector. The proton-proton collision produces Z bosons, which decay into an electron-positron pair. The sample has 2000 events.

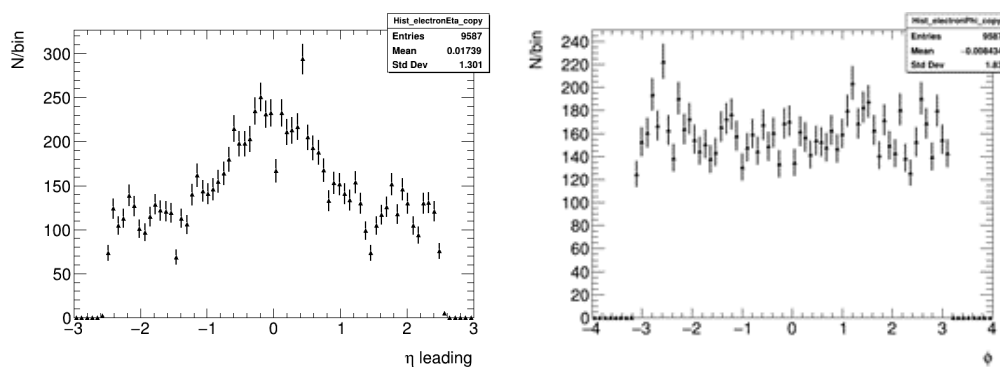
To get the information out of this sample a n-tuple was made. Each of the branches of this n-tuple has a different kind of kinematic stored in them. To fill in these branches one took all the electron candidates from the electron container and, one at a time, found their kinematics and placed them in the correct branch. When more than one electron candidates per event was needed, like when finding the invariant mass of two electrons, the electrons were stored until needed. Then at the end of the event, the invariant mass is found using the two stored electrons, the kinematic branch will be filled and

then a new event started, so the stored electrons are forgotten.

In this electron container are all the electron candidates, without any quality test. Many of these electron candidates are electromagnetic background, like photons, from bremsstrahlung or other processes. In the first few plots all of the electron candidates are represented, before the developed model will reduce the number of electron candidates using cuts.

5.2 Kinematics

When looking at the different angles in the ATLAS detector, the distribution of electron ϕ is spread uniformly over the entire 2π range, while the electron η has a distribution spread with a peak at $\eta = 0$. This is because of the way η is defined, as seen in eq. 2.11. The ATLAS detector measures the electron η differently on the $|\eta| < 2.7$ range. The ATLAS detector does not measure electrons well for $\eta \approx 1.5$, so there are two minimums in fig. 5.1a. This can be seen in fig. 5.2 where the reconstructed η , in black, is plotted together with truth η , in blue. Here the electrons pass between the barrel and endcap EM calorimeters, $1.37 < |\eta| < 1.52$, [10]. The electrons between these angles will not be considered in the reconstruction. The reconstructed electrons and the truth electrons are very similar when close to 0, but when $|\eta| > 1$ the reconstructed electrons are fewer than the truth electrons and for $|\eta| > 2.7$ there are no reconstructed electrons, but still many truth electrons.



(a) Electron η .

(b) Electron ϕ .

Figure 5.1: The angles η and ϕ of the electrons in the sample.

The truth electrons are made by the Monte Carlo simulation, but not

measured by the simulated ATLAS detector and then reconstructed. The reconstructed electrons are made by the Monte Carlo simulation and then measured by the simulated ATLAS detector and then reconstructed. This means that the truth electrons do not have background and min-bias in them, and the electrons can cover the full $|\eta|$ range. The reconstructed electrons will have background, min-bias and the electrons only cover the range of $|\eta| < 2.7$.

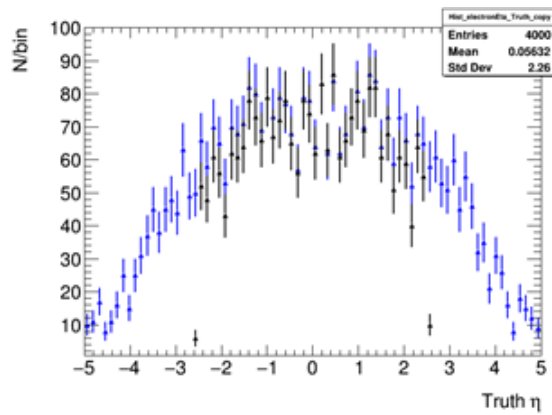
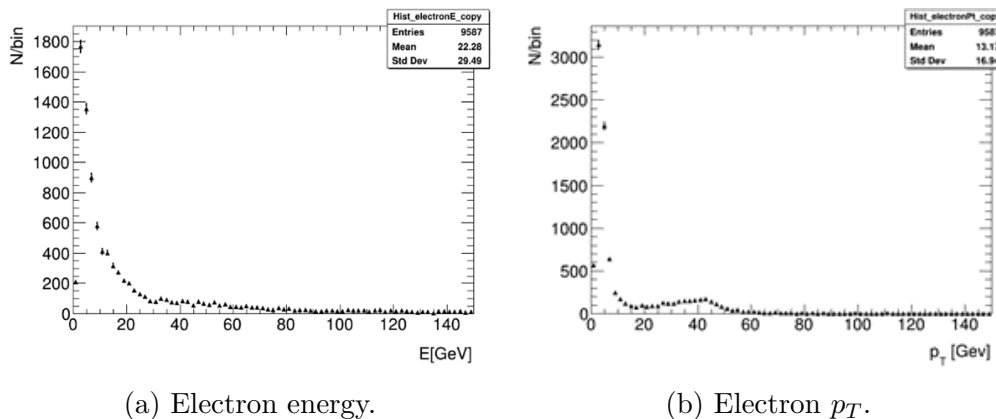


Figure 5.2: Electron Truth (Blue) and reconstructed (Truth) η (black).

In the reconstructed energy and transverse momentum p_T (see fig. 5.3a and fig. 5.3b) there are a lot of unexpected low energy electrons, less than 20 GeV. These low electrons will occur in other plots later. The energy plot is spread out, but there is a peak at 45 GeV in the p_T plot 5.3b. This peak is expected since this is half the known Z mass of 91.19 GeV.



(a) Electron energy.

(b) Electron p_T .

Figure 5.3: The p_T and energy of the electron candidates in the sample.

To reconstruct the mass of the Z boson, one must calculate the invariant mass of the electrons, see eq. 3.8, but this equation requires two electrons. Most events have more than two electrons as seen in fig. 5.4. To use eq. 3.8 one uses the two electrons with the highest p_T , these two electrons are called leading and sub-leading electrons. The p_T of these electrons can be seen in fig. 5.5a and fig. 5.5b. There are clear peaks at around 45 GeV in both plots. To see which leading p_T and sub-leading p_T that are matched up one can use a scatterplot as seen in fig. 5.6. There is a bright spot at very small p_T values, but like expected there is a brighter area where the peaks of 5.5a and 5.5b are. These electrons will give a peak around double 45 GeV.

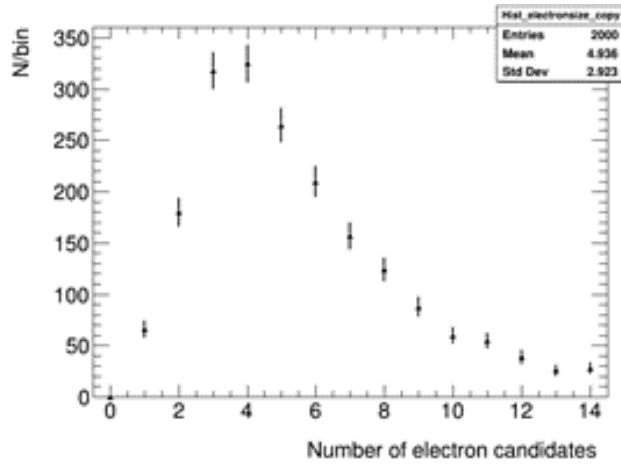
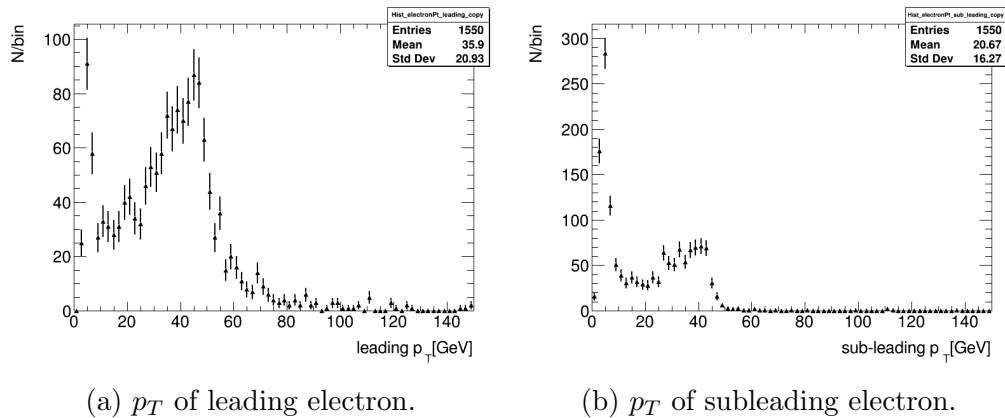


Figure 5.4: Number of electrons per event.

(a) p_T of leading electron.(b) p_T of subleading electron.Figure 5.5: The leading and subleading p_T of the electrons in the sample.

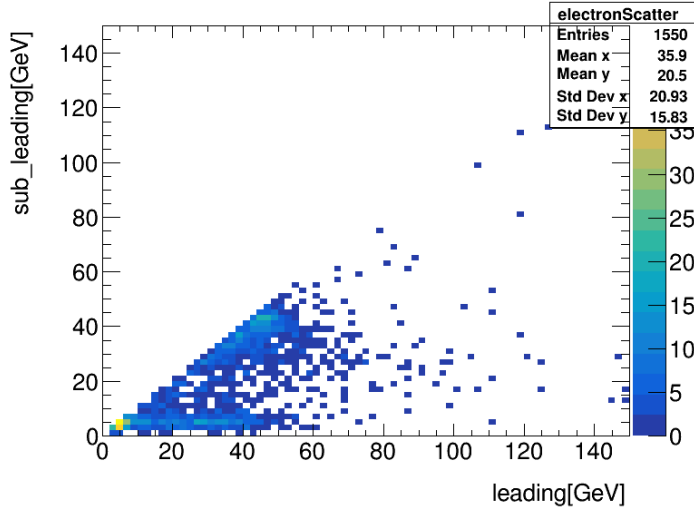


Figure 5.6: Scatter plot of leading vs subleading p_T . There are bright spots at coordinates (5,5) and (45,45)

The invariant mass of the Z boson can then be found with the leading and sub-leading electrons, by using eq. 3.8, the results are shown in fig 5.7. There is a clear peak at 90 GeV, which is where the peak is expected to be found, since it is two times the peaks in the 5.5a and 5.5b plots and the Z mass is known to be 91.19 GeV. The plot is fitted with a Crystal Ball distribution and a Breit-Wigner + Gauss distribution. Crystal Ball distribution is a Gaussian with a power-law tail. Breit-Wigner distribution is used to describe unstable particles with a decay width Γ . This Γ is the full width at half maximum (FWHM) of a Breit-Wigner distribution. The decay width, Γ , and lifetime, τ , are related via:

$$\tau = \frac{1}{\Gamma} \quad (5.1)$$

Therefore, a particle with higher lifetime has a smaller decay width and a stable particle would not have a decay width. The invariant mass in fig. 5.7 is fitted well by a Breit-Wigner + exponential distribution so only this fit is shown. The Crystal Ball fit did not work for multiple plots in later chapters and will therefore not be used. As in the energy and p_T plots (fig. 5.3a and fig. 5.3b) there are low energy electrons in the Z mass, with a wide peak at 15 GeV.

To explain the low energy electrons, the truth electrons will be compared

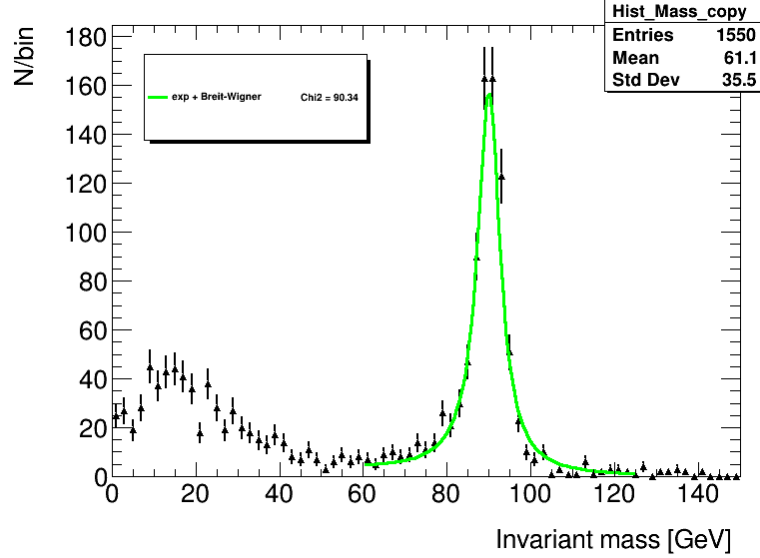
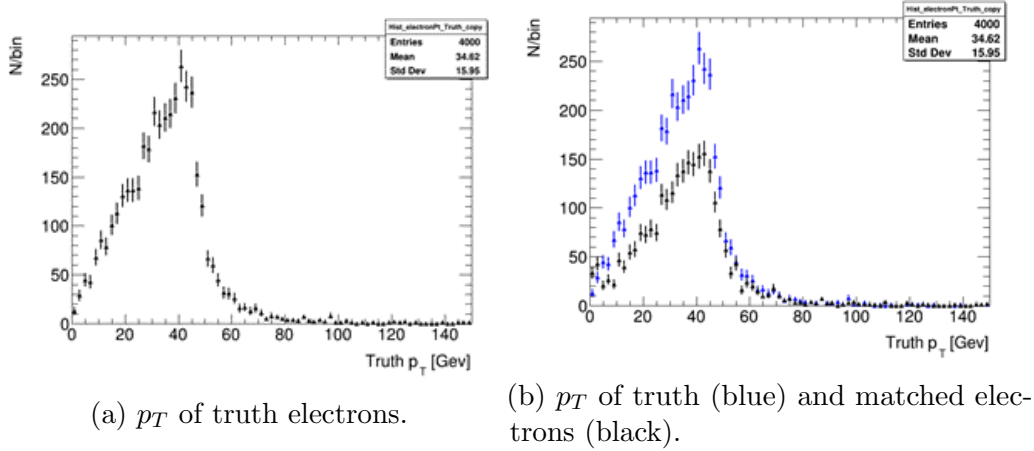
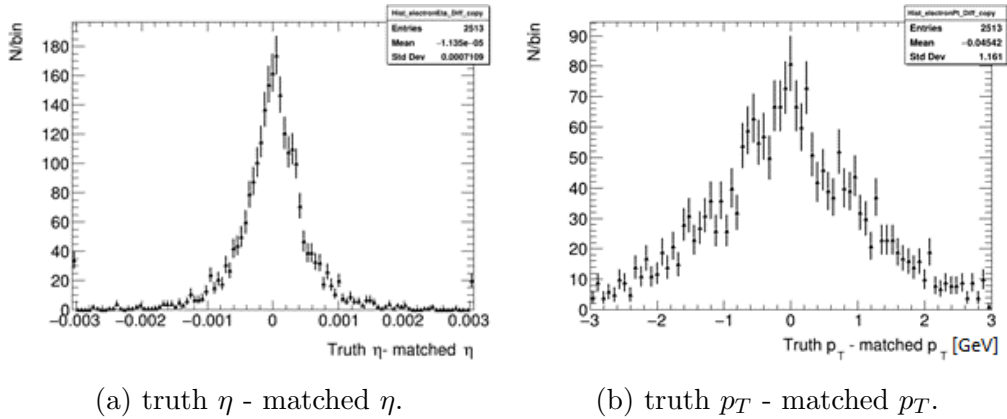


Figure 5.7: The reconstructed invariant mass.

with the matched electrons and reconstructed electrons. As seen in fig. 5.8a there are a peak at 40 GeV like in the reconstructed p_T plot (fig. 5.3b). However there is not a peak of low p_T electrons in fig. 5.8a. By looking at the matched electrons it can be determined if it is background or if it is the way electrons are measured.

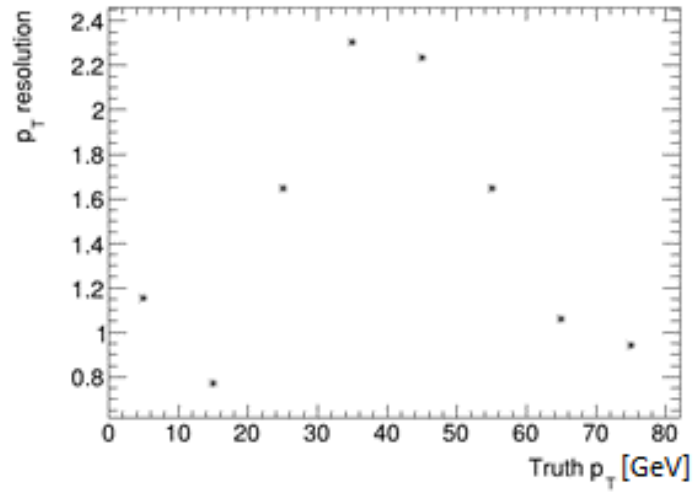
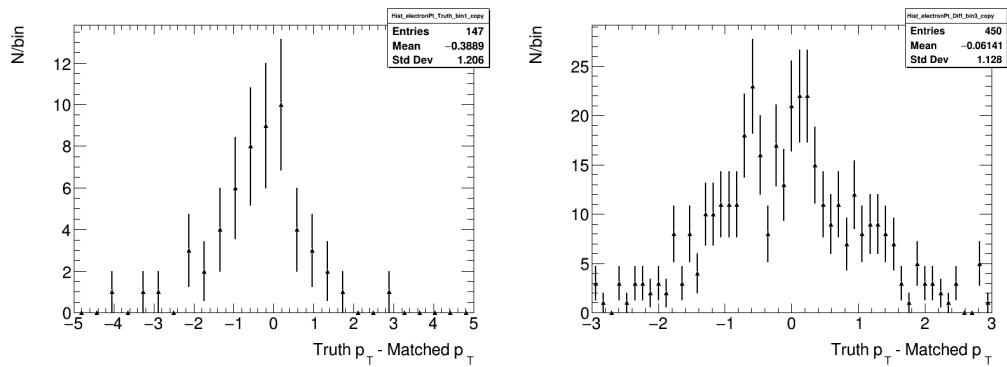
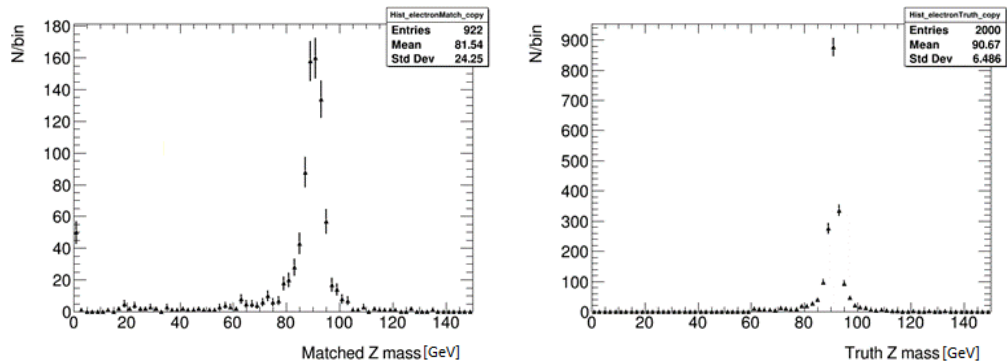
As seen in fig. 5.8b there is less small p_T electrons in the matched electrons than in the truth electrons. This is because of the limit in η measurements as seen in fig. 5.2. The definition $|p| = p_T \cdot \cosh\eta$ shows that high η gives smaller p_T and the η measurements are limited to $|\eta| < 2.7$, therefore small p_T disappear. If the reconstruction changes the η and p_T , this could introduce the low energy electrons. By looking at the difference between truth and matched electrons, as seen in fig. 5.9a and fig. 5.9b, the η or p_T resolutions can be found. Since the truth - matched plots are approximately gaussian, the resolution is defined as the full width at half maximum (FWHM). The FWHM for p_T is around 1.5 GeV and the FWHM for η is about 0.001. The reconstruction does not change the values of η or p_T by very much. This means that the low energy electrons comes from the background.

In fig. 5.10 the p_T resolution is plotted against the truth p_T . The resolution goes from around 0.8 GeV to around 2.4 GeV. The resolution is smallest for small and large p_T and is highest around 40 GeV. The peak at 40 GeV is


 Figure 5.8: The p_T of truth electrons and matched electrons.

 Figure 5.9: Truth - matched electron η and p_T for finding the η and p_T resolutions.

there because most truth and matched electrons have a p_T of around 40 GeV, this can be seen in fig. 5.8b. This distribution gives large uncertainty for the resolutions. Fig. 5.11a have 147 entries and fig. 5.11a have 450 entries.

Another way to check if the electrons are changed by reconstruction, is to look at the mached Z mass and the truth Z mass in plots 5.12a and 5.12b. There is some very small peaks at 20 GeV in 5.12a that are not in 5.12b, but it is so much smaller than the peak in the Z mass plot 5.7. Again, one can see that the electrons are not changed enough for the low energy electrons to matter. This means that the low energy electrons come from the background.

Figure 5.10: p_T resolution vs truth p_T .(a) truth p_T - matched p_T for
 $0 \text{ GeV} < \text{truth } p_T < 10 \text{ GeV}$ (b) truth p_T - matched p_T for
 $30 \text{ GeV} < \text{truth } p_T < 40 \text{ GeV}$.Figure 5.11: Truth - matched electron p_T for different truth p_T ranges to see how the distribution changes.

(a) Matched invariant mass.

(b) Truth invariant mass.

Figure 5.12: The invariant mass⁵² for matched and truth electrons.

5.3 Background

Different decays such as $Z \rightarrow \tau^+\tau^-$, diboson, top quarks and Drell-Yan processes send out electrons that form a background for the $Z \rightarrow e^+e^-$ and $H \rightarrow e^+e^-$ decays [10].

The $Z \rightarrow \tau^+\tau^-$ produces two electrons through leptonic decay of the τ . In the diboson processes there are multiple ways to produce two electrons, like in $ZZ \rightarrow eeee, ee\mu\mu, WZ \rightarrow eee\nu, ee\mu\nu$ and $WW \rightarrow ee\nu\nu$. For the top quark processes the electrons are produced in semileptonic decays and electrons from jets. The Drell-Yan process is when a quark from a hadron and an antiquark from another hadron annihilate, creating a photon or Z boson which can decay to e^+e^- . B and D jets were also considered. The electrons produced by these jets should have low p_T , but due to the number of electrons, some of them could have high enough p_T to show up in the background. The high amount of electrons also made it difficult to add to the background and therefore it was ignored.

The different background processes were plotted one at a time, normalized, scaled by luminosity and cross section and then added to the same histogram. This is different for the Drell-Yan process, where different mass ranges have different cross sections. Here the different ranges were plotted in the same way as the other processes, plotted one at a time, normalized, scaled by luminosity and cross section and then added to the same Drell-Yan histogram, which then was added to the main background plot.

Table 5.1: Cross section for the different backgrounds

Process	Cross section
$Z \rightarrow \tau\tau$	1900 pb
ttbar	696 pb
Single top	43.7 pb
Drell-Yan in mass range 120-180 GeV	17.5 pb,
Drell-Yan in mass range 180-250 GeV	2.92 pb,
Drell-Yan in mass range 250-400 GeV	1.08 pb,
Drell-Yan in mass range 400-600 GeV	0.196 pb,
Drell-Yan in mass range 600-800 GeV	37.4 fb,
Drell-Yan in mass range 800-1000 GeV	10.6 fb,
Drell-Yan in mass range 1000-1250 GeV	4.26 fb
Diboson	1.27 pb

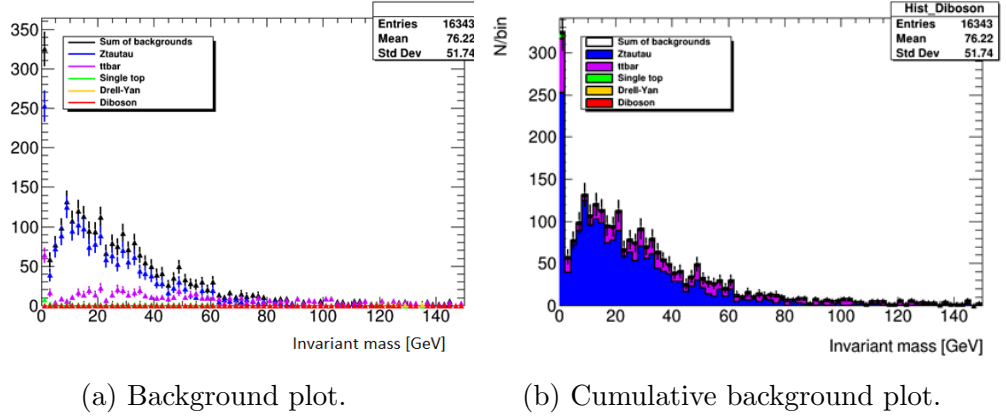


Figure 5.13: Background plots with $Z \rightarrow \tau\tau$, $t\bar{t}$, single top, Drell-Yan and diboson.

Because of the big difference in cross sections the $Z \rightarrow \tau\tau$ and $t\bar{t}$ dominates the background, this can be seen in fig. 5.13a and fig. 5.13b. This is very clear at low energy, but at higher energies the dominance of $Z \rightarrow \tau\tau$ and $t\bar{t}$ is difficult to see. The importance of the different backgrounds is easier to see using a log scale, such as seen in fig. 5.14. At around 90 GeV one can see that $t\bar{t}$ is the dominating contribution with some $t\bar{t}$ and single top. The diboson also have a peak at 90 GeV, which is expected since a Z boson from the diboson can decay to 2 electrons like in the main sample. The Drell-Yan and diboson processes both have small cross sections and therefore do not contribute much to the background.

By normalizing the matched Z mass (see fig. 5.12a), scaling it by the cross section, 1900 pb, like the background and adding it to the background plot one gets fig. 5.15. This plot is very similar to the Z mass plot in fig. 5.7. This means that these backgrounds can be used to find the significance of different cuts on the electrons. A cut is a criterion, for example having a p_T over 20 GeV, that the electrons must have to be considered.

Another background to consider is the min-bias added to the given sample. This sample has a high cross section, like the B and D jets, but will be more important for the significance. Most of the electrons are still low energy electrons, so if one scale it the same way as the other backgrounds, this background would dominate even the Z peak. Because of this, the background was scaled to the cross section of the main $Z \rightarrow e^+e^-$ sample.

The full background found in this section is $Z \rightarrow \tau^+\tau^-$, diboson, top

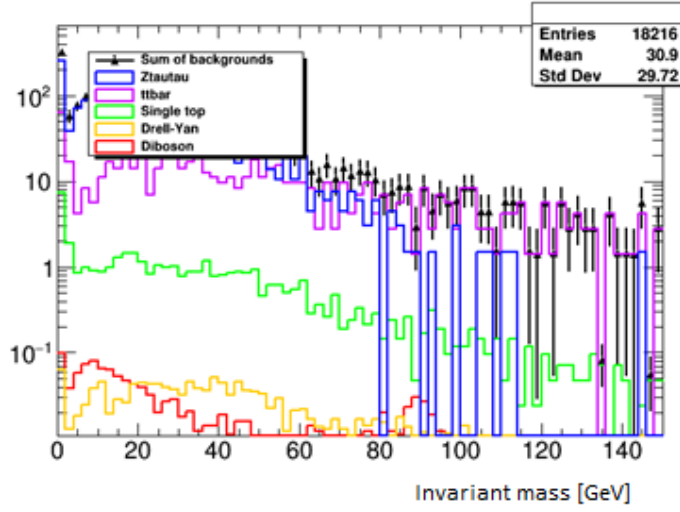


Figure 5.14: Background plots with $Z \rightarrow \tau\tau$, $t\bar{t}$, single top, Drell-Yan and diboson on a log scale.

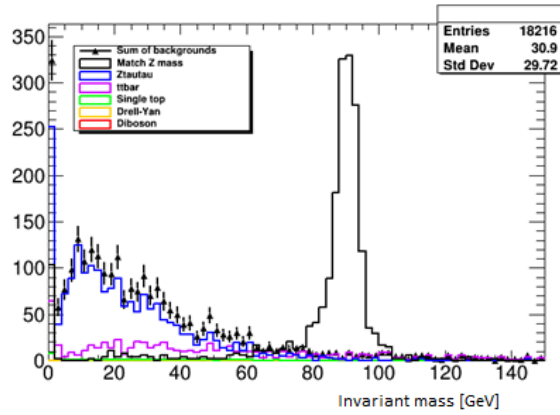


Figure 5.15: Invariant mass for background processes, $Z \rightarrow \tau\tau$, $t\bar{t}$, single top, Drell-Yan and diboson, and a truth-matched $Z \rightarrow e^+e^-$ signal sample.

quarks, Drell-Yan and the min-bias processes. This background is dominated by $Z \rightarrow \tau^+\tau^-$, $t\bar{t}$ and min-bias for small invariant mass and $t\bar{t}$ $Z \rightarrow \tau^+\tau^-$ and single top for high invariant mass.

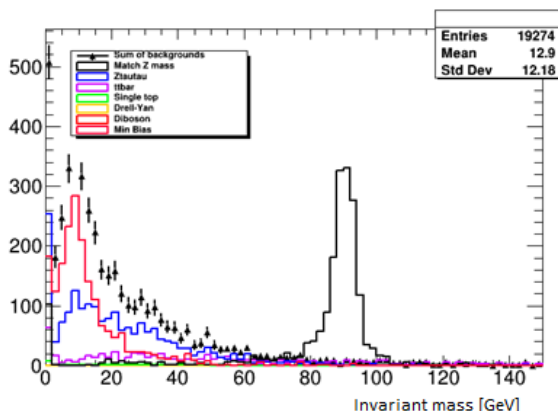


Figure 5.16: Background plots with $Z \rightarrow \tau\tau$, $t\bar{t}$, single top, Drell-Yan and diboson and min bias.

5.4 Selection optimisation

To remove unwanted background, some cuts on the electrons can be introduced. A cut is a filter that reject unwanted electrons. By doing cuts on the backgrounds there will also be cuts on the signal events, in this case the events from the $Z \rightarrow e^+e^-$ process. To find the cuts that keep as much of the signal events as possible, while cutting as much background as possible, one must have a function that finds the best cuts. This function is the significance:

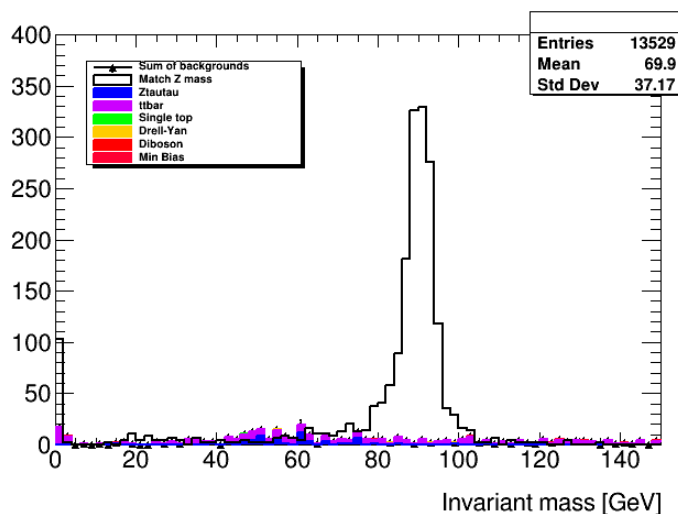
$$\text{significance} = \frac{S}{\sqrt{S+B}} \quad (5.2)$$

where S is the signal and B is the background. The signal and background are both defined to be the number of events in a 4σ distance, about 15 GeV, from the 90 GeV peak. The cuts will be p_T cuts on the sub-leading electron, as this will also cut the leading electrons. When doing a sub-leading $p_T > 20$ GeV cut on the background plot in fig 5.16 it is changed into the plot in fig. 5.17. This cut changes the significance as shown in table 5.2. In this case the significance goes up because of the cuts, but not much. This makes sense since the matched Z mass did not change and the background is very small in comparison. Table 5.2 shows the signal, background and significance of no cut, $p_T > 20$ GeV, $p_T > 30$ GeV and $p_T > 40$ GeV. The signal of no cut, $p_T > 20$ GeV and $p_T > 30$ GeV did not change, but it decreased for

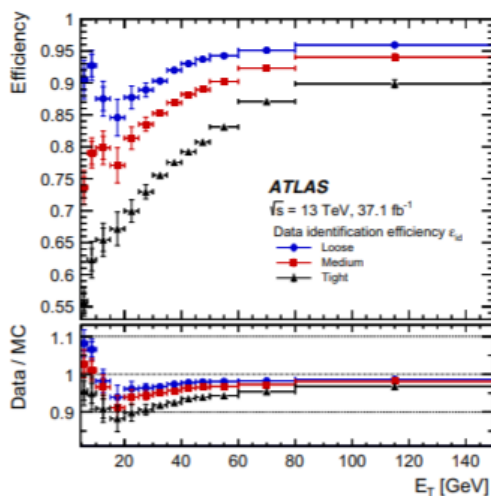
$p_T > 40$ GeV. This means that the significance is highest at $p_T > 20$ GeV and $p_T > 30$ GeV where they have the same signal and background. The significance is slightly higher for $p_T > 30$ GeV.

Table 5.2: The significance of the p_T cuts

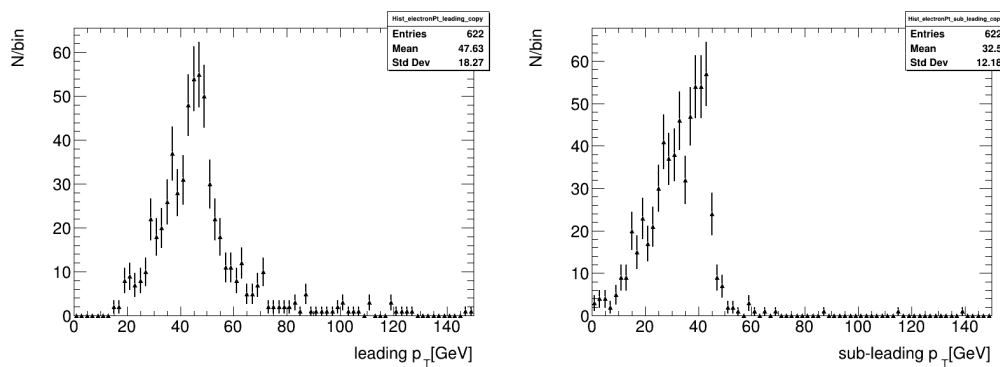
	Without cuts	With $p_T > 20\text{GeV}$	$p_T > 30\text{GeV}$	$p_T > 40\text{GeV}$
signal	1597.07	1597.07	1597.07	1512.58
background	0.0077	0.0055	0.0055	0.0055
significance	39.9332	39.9633	39.9634	38.8919

Figure 5.17: Background plots with $p_T > 20$ cuts.

The cuts removed a lot of the background. Another way to cut is to change what the analysis sees as an electron. There are three different operating points, Loose, Medium and Tight. All of these have requirements on tracking criteria. They require at least two hits in the pixel detector and in total seven hits in the pixel and silicon strip detector. Medium and Tight also require that one of the pixel hits must be the inner most pixel layer. The Tight selection have two other criteria, E/p and ω_{stot} , where ω_{stot} , the shower width, depends on the electron candidate η and the $E/p < 10$ [51]. These higher requirements mean that Medium and Thight working points reject more of the background than Loose working points, this can be seen in fig. 5.18.

Figure 5.18: Efficiency plotted against transverse energy E_T [24].

As an example here are the $Z \rightarrow e^+e^-$ sample leading and sub-leading p_T in fig. 5.19a and in fig. 5.19b and invariant mass 5.20. For the fit on the invariant mass plot the Crystal Ball fit did not work, so it was replaced by a Gauss instead.

(a) Loose leading p_T .(b) Loose sub-leading p_T .Figure 5.19: The leading and subleading p_T of the electrons.

When one looks at the invariant mass plots in fig. 5.7 and 5.20 one can see that most of the background has been rejected, some by the p_T cuts and some by the Loose working points. To see if these cuts improve the significance we will look at the background plots again. Fig. 5.21 shows the background cuts with Loose working points and shows that this takes

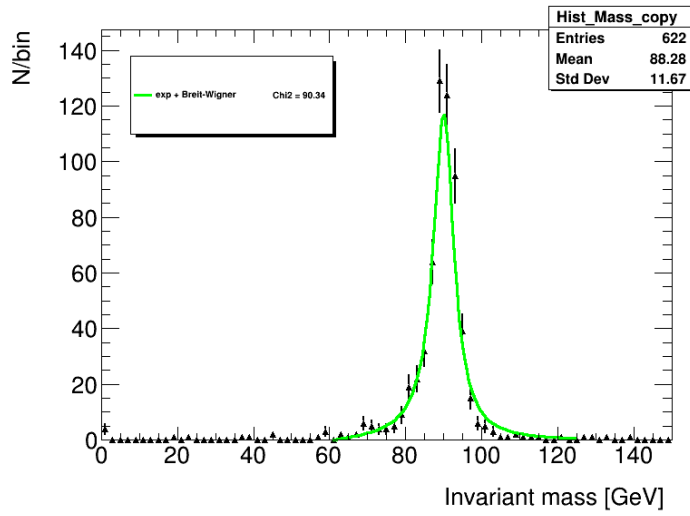


Figure 5.20: Loose invariant mass.

out most of the background. In table 5.3 the different significance is shown. The Loose working points makes a big difference for the significance because it cuts almost all of the background. Because it removes so much of the background any more p_T cuts will only lower the significance.

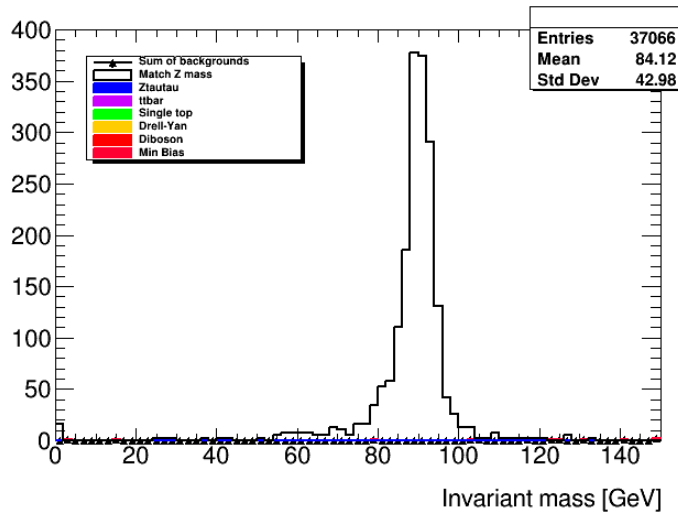


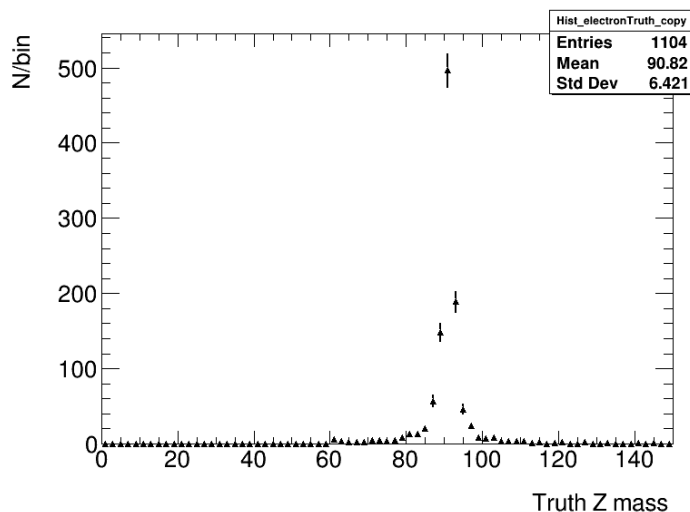
Figure 5.21: Loose background with p_t cuts.

The p_T cuts that increase the significance the most is $p_T > 20$ GeV and $p_T > 30$ GeV. A different type of cut, Loose electron, increased the significance. The increase in significance is higher than for the p_T cuts. The efficiency, ϵ ,

Table 5.3: The significance of the p_T cuts and Loose working points

	Without cuts	With $p_T > 20\text{GeV}$	Loose with $p_T > 20\text{GeV}$
signal	1597.07	1597.07	1745.38
background	0.0077	0.0055	0.0001
significance	39.9332	39.9633	41.7777

the number of events after cuts divided by the number of generated events inside the same η range, $-2.7 < \eta < 2.7$, can be found using eq. 5.3

Figure 5.22: Truth invariant mass for $|\eta| < 2.7$.

$$\epsilon = \frac{N_{reco}}{N_{gen}} \quad (5.3)$$

Here N_{reco} is the number of events in fig. 5.20, 622, and N_{gen} is the number of events in fig. 5.22, 1104. The efficiency ϵ is 0.56. This efficiency will be used in eq. 2.10 to calculate the cross section of $Z \rightarrow e^+e^-$. Here $N_{data} - N_{background} = N_{reco} = 622$ and $\epsilon = 0.56$. To find the integrated luminosity, L , one can use eq. 2.9, with $N = 2000$ and $\sigma = 1.90$ nb, where N is the number of entries in the sample and σ is the total cross section of the sample. This gives $L = 1052.63 \text{ nb}^{-1}$. When calculating the effective cross section one gets:

$$\sigma_{eff} = \frac{N_{reco}}{\epsilon L} = 1.06 \text{ nb} \quad (5.4)$$

When looking at the $p_T > 20$ GeV cut one gets an efficiency, $\epsilon = \frac{739}{1104} = 0.67$ and then a cross section of:

$$\sigma_{eff} = \frac{N_{reco}}{\epsilon L} = 1.05 \text{ nb} \quad (5.5)$$

Both off these effective cross sections are about half of the real cross section of $\sigma = 1.90$ nb. It is expected that they should be lower, as they are effective cross sections that only measure electrons with $|\eta| < 2.7$.

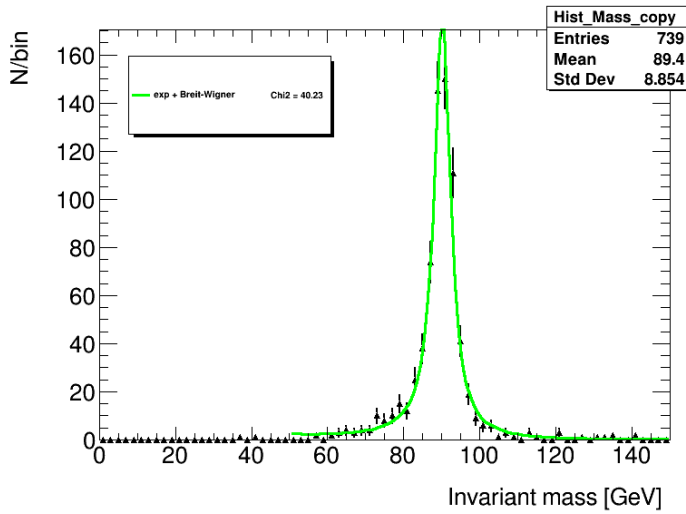


Figure 5.23: Invariant mass plot with a $p_T > 20$ GeV cut. The FWHM of this fit is 5.06 GeV.

5.5 Concluding comment

In this chapter a model for finding the invariant mass was developed. In each event, one finds the leading and sub-leading electrons and these electrons are then used to calculate the invariant mass using eq. 3.8. To remove some of the background, cuts on the electrons are preformed. The cuts that gave the highest significance were $p_T > 20$ GeV and Loose working points.

This invariant mass model works very well at finding the $Z \rightarrow e^+e^-$ decay. It works well for both $p_T > 20$ GeV cuts and for Loose electron cuts. The different cuts have different efficiencies but give very similar effective cross sections. Because of this, both cuts will be included in the model and used to

analyse the real data in the next chapters. This could be interesting as they could give very different result, even when they have so similar result when looking at Monte Carlo.

Chapter 6

Real data: $Z \rightarrow e^+e^-$

In this chapter the reconstruction model from chapter 5 will be evaluated using real data sample and compared with the MC sample from the previous chapter. A single file from the sample will be used in this chapter.

This real data sample has a $\sqrt{s} = 13$ TeV and there are 7402 events. This sample is a DAOD, a smaller subset of the full AOD, of all the events from 2018. This DAOD has a invariant mass cut, the invariant mass of at least one pair of electron candidates must be greater than 50 GeV. This pair of electron candidates does not have to be leading and sub-leading electron candidates since the p_T is just a projection. This DAOD cut will show up in many of the plots in this chapter and the next chapter.

6.1 Kinematics

In this section we will look at the same kinematics as in the chapter 5, the ϕ, η , energy and p_T of all electron candidates, the p_T of the leading and sub-leading electron candidates and the invariant mass of the events. These will be compared to the MC kinematics. Here we expect a higher background to signal ratio because the cross sections for $Z \rightarrow e^+e^-$, and later $H \rightarrow e^+e^-$, is small.

The electron ϕ in fig. 6.1b is spread over the whole 2π range, similar to fig. 5.1b from the MC $Z \rightarrow e^+e^-$ sample. The electron η in fig. 6.1a have a similar shape to fig. 5.1a with a top around $\eta = 0$. Fig. 6.1a shows that the ATLAS detector does not detect electrons well for $|\eta| \approx 1.5$. This is also the

case for the MC $Z \rightarrow e^+e^-$ in fig 5.1a. The angle plots are very similar to the MC $Z \rightarrow e^+e^-$ angle plots.

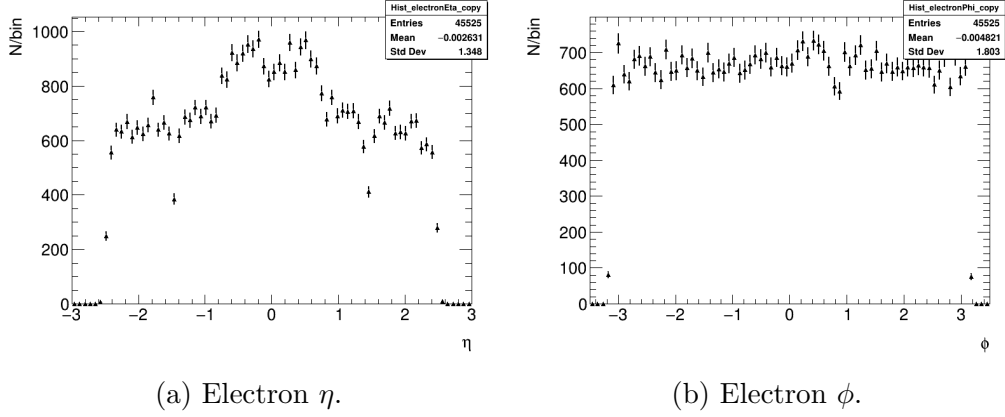


Figure 6.1: The angles η and ϕ of the electrons in the real data.

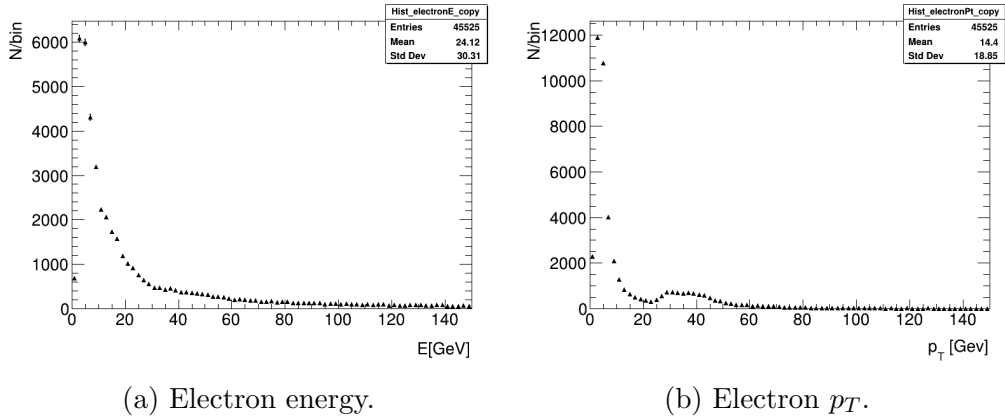


Figure 6.2: The energy and p_T of the electrons in the real data.

Like the angles, the energy of the real electron candidates shown in fig 6.2a is very similar to the energy of the electrons in the MC $Z \rightarrow e^+e^-$ in fig. 5.3a. The electron candidate p_T in fig. 6.2b looks similar to the electron p_T in fig. 5.3b, with few electrons around 20 GeV and a peak around 40 GeV. The difference between the two electrons p_T plots is the width of peak in the real data that is spread from 25 GeV to 45 GeV, but not as high like the one in the MC sample. The valley, due to the few electron candidates around 20 GeV, in the real data is not as wide as in the MC sample and ends at 25 GeV,

not at the 45 GeV peak. The difference comes from the larger background in the real data and from cuts for the DAOD.

To find the invariant mass using eq. 3.8 one needs two electron candidates. However this sample has a distribution of electron candidates per event, where most of the events have 3 or more electrons, seen in fig. 6.3. Once again the two electron candidates with the highest p_T : the leading and the sub-leading electron candidates, will be used.

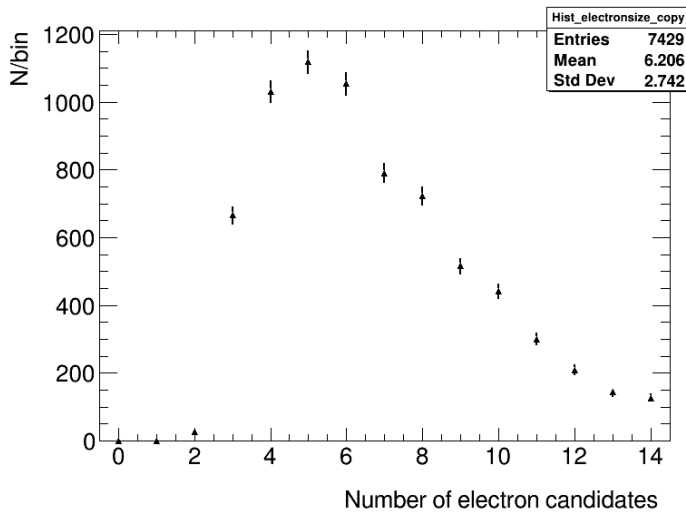


Figure 6.3: Number of electron candidates in per event.

The p_T of the leading and sub-leading electron candidates are shown in fig. 6.4a and fig. 6.4b. Again the cuts from the DAOD are very clear. There is no leading electron candidates, fig. 6.4a, with a p_T under 20 GeV and only after 25 GeV, half of the DAOD invariant mass, are there more than a few leading electron candidates. The p_T of sub-leading electron candidates, fig. 6.4b, looks very similar to the MC sub-leading p_T , fig. 5.5b.

There is a clear 40 GeV peak in the leading p_T plot, fig. 6.4a, and a clear 40 GeV cut off in sub-leading p_T in the sub-leading plot, fig. 6.4b. This is very similar to the MC $Z \rightarrow e^+e^-$ leading and sub-leading p_T plots, fig. 5.5a and fig. 5.5b, where there is a clear peak at 45 GeV in the leading p_T plot, fig. 5.5a, and a clear cut off at 45 GeV in the sub-leading p_T plot, fig. 5.5a. The p_T peaks around 40 GeV in the leading and sub-leading plots, fig. 6.4a and fig. 6.4b, means that there is probably a 90 GeV peak in the invariant mass plot, similar to MC $Z \rightarrow e^+e^-$.

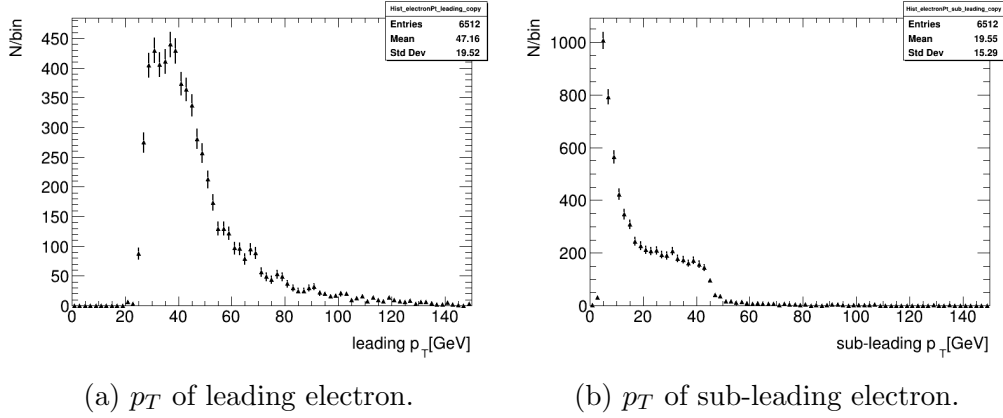


Figure 6.4: The leading and subleading p_T of the electrons in the real data.

To see which leading electron candidates and sub-leading electron candidates line up one uses a scatterplot. The real data scatterplot, fig. 6.5, and the MC $Z \rightarrow e^+e^-$ scatterplot, fig. 5.6 are very different. The real data scatterplot again shows the cuts from the DAOD in it, where the leading p_T have no electron candidates under 20 GeV and very few under 25 GeV.

Fig. 6.5 have a clear bright spot at coordinates around (35,5). This bright spot means that there will be a peak in the invariant mass that is not a Z peak at 91.19 GeV. Like in the MC $Z \rightarrow e^+e^-$ scatterplot there is a slight bright area around coordinates (45,40) in the real data scatterplot, fig. 6.5. This means that there will be a Z peak at 90 GeV in the invariant mass plot.

The clear bright spot around coordinates (35,5) probably comes from the cutting done on the DAOD. The MC $Z \rightarrow e^+e^-$ scatterplot, fig. 5.6, has a bright spot near (0,0) and a bright line where the sub-leading p_T is 5 GeV. This is because of all the low energy electrons. In a real data sample there were probably more low energy electrons, but these were cut by the invariant mass cuts of the DOAD, therefore this bright spot got moved to make a bright spot close to half the value of the cut, as there are a lot more electrons there. If this is the case, one expects to see a sharp cut off in the invariant mass plot of this sample and in fig. 6.6 there is such a clear cut off. Another explanation for this bright spot could be the electrons from $W \rightarrow e\nu_e$ as these would have a $p_T \approx 40$ GeV.

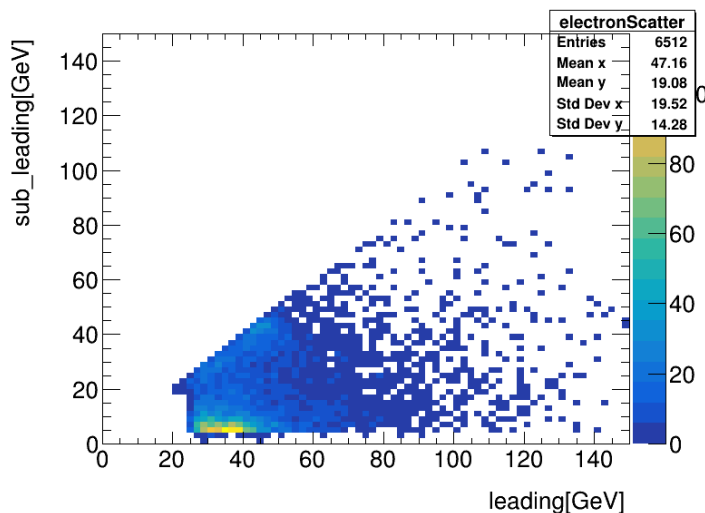


Figure 6.5: Scatter plot of leading vs sub-leading p_T . There are brightspots at coordinates (3,35) and (45,45).

In fig. 6.6 the invariant mass of the real data is plotted. This plot is very different from the MC $Z \rightarrow e^+e^-$ invariant mass plot, seen in fig. 5.7. There is a large Z peak at 90 GeV in fig. 6.6, similar to in fig. 5.7. However, there is also a peak at 50 GeV with a sharp cut off under 50 GeV. This is expected from the 50 GeV invariant mass cuts from the DAOD and from the (35,5) bright spot in the scatterplot, fig. 6.6. The 50 GeV invariant mass DOAD cut does not have to come from the leading and sub-leading electron candidates, so there is some low invariant mass in the plot. The invariant mass is well fitted with a Breit-Wigner distribution with an exponential background.

Here the invariant mass plot includes the Higgs region from 115 GeV and upwards, but this will not be the case for the rest of the invariant mass plots in this chapter. This is to make sure that the cuts that will be done in the next section will not force a Higgs peak where there potentially isn't one.

The significance of the Z peak in fig. 6.6 can be seen in table 6.1. This significance will be increased in the next section with different cuts on the p_T of the sub-leading, and therefore the leading electrons, and by cutting on the Loose, Medium and Tight workpoints.

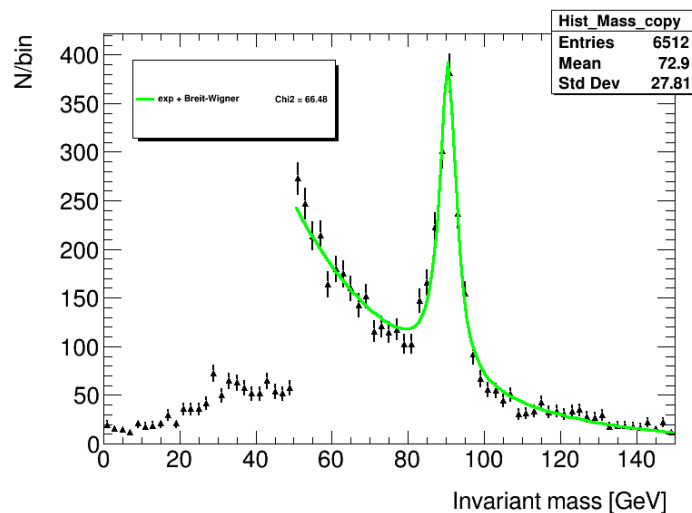


Figure 6.6: Invariant mass plot of the data.

Table 6.1: The significance of the real data before any cuts

	Without cuts
Signal	2634.58
Background + signal	5166.96
Significance	36.6518

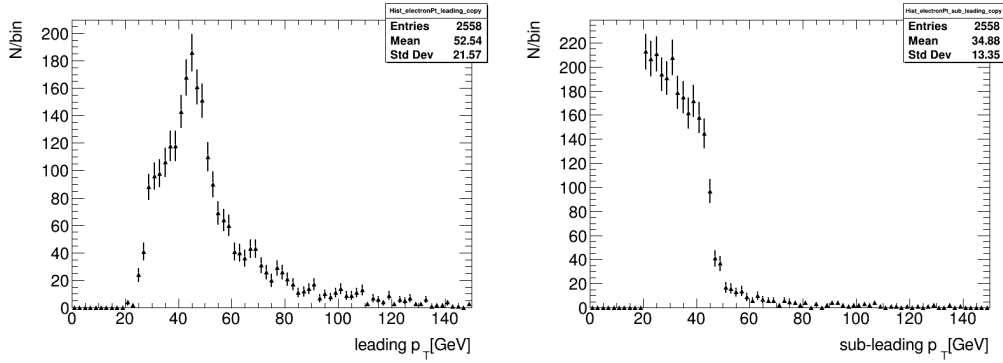
6.2 Cuts

In this section the real data plots will be cut with sub-leading p_T and working points. This is done to cut the large background and make larger peaks. To make sure that we do not "force" a Higgs peak, the Higgs region of 115 GeV and upwards will not be shown in the invariant mass plots. We will also focus on the Z mass peak and make cuts that increase the significance of the Z peak, like in the MC chapter. Table. 6.2 shows that the significance of the $p_T > 20$ GeV cut is the highest for the p_T cuts.

6.2.1 p_T cuts

Since the significance of the $p_T > 20$ GeV cut is the highest for the p_T cuts, see tab. 6.2, this subsection will look at how some of the kinematics changes that occur due to this $p_T > 20$ GeV cut. When looking at the leading and

sub-leading p_T plots in fig. 6.7a and fig. 6.7b we see a peak at 45 GeV in fig. 6.7a and a spread from 20 GeV to 40 GeV in the sub-leading p_T plot in fig. 6.7b. Here it is clear that a 90 GeV invariant mass peak will be there and by looking at a scatter plot it is possible to see if the 50 GeV peak is still there. In the leading p_T there is a slope of higher p_T electrons, while on the sub-leading there is a clear cut off.



(a) p_T of leading electron
with $p_T > 20$ GeV.

(b) p_T of sub-leading electron
with $p_T > 20$ GeV.

Figure 6.7: The leading and subleading p_T of the electrons in the real data with $p_T > 20$ GeV.

The scatterplot fig. 6.8 shows how the $p_T > 20$ GeV cut effects the different electron candidates pairs. Here the (45,45) bright spot from fig. 6.5 is much clearer with this cut. This means that the 90 GeV invariant mass will still be there. The (35,5) bright spot from fig. 6.5 has disappeared, since the sub-leading p_T must be over 20 GeV. A new bright spot has appeared in fig. 6.8 at (35,30). This new bright spot shows up as some background in the new invariant mass plot.

The invariant mass of the real data with a $p_T > 20$ GeV cut is shown in fig. 6.9. The cut removes most of the low invariant mass events and the exponential background is lowered. This makes the invariant mass under the 50 GeV peak, in fig. 6.6 disappear. The 50 GeV peak also disappear after the $p_T > 20$ GeV cut is implemented on the data. In fig. 6.9 the Higgs region of 115 GeV and upwards was removed to not force in a Higgs peak.

Table 6.2 shows the significance of different p_T cuts. For the real data the $p_T > 20$ GeV has the highest significance. This is different from the MC

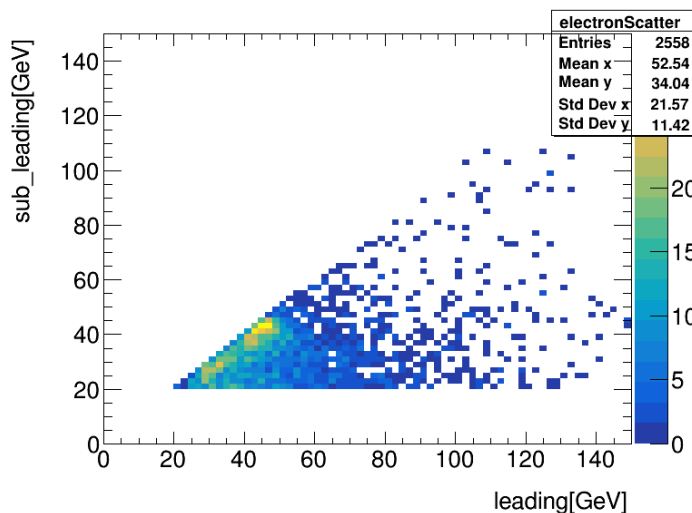


Figure 6.8: Scatter plot of leading vs sub-leading p_T with $p_T > 20$ GeV. There are brightspots at coordinates (35,30) and (45,45)

$Z \rightarrow e^+e^-$ where the significance was highest for $p_T > 30$ GeV, the $p_T > 20$ GeV has almost the same significance, seen in table. 5.2. In table 6.2 the significance of a $p_T > 10$ GeV is also included to make sure that the $p_T > 20$ GeV cut gives the highest significance. The $p_T > 20$ GeV cut will be used in the rest of the chapter. In all of these cuts the Higgs region was removed. This makes sure that significance only looks at the Z peak and not any potential Higgs peak.

Table 6.2: The significance of the p_T cuts.

	$p_T > 10$ GeV	$p_T > 20$ GeV	$p_T > 30$ GeV	$p_T > 40$ GeV
signal	2949.02	2963.67	2335.8	756.51
background + signal	4154.47	3394.06	2335.01	751.468
significance	45.7531	50.871	48.3382	27.597

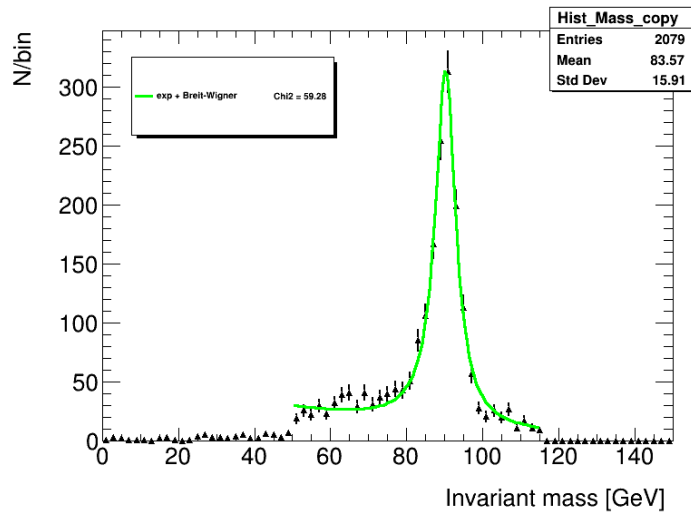
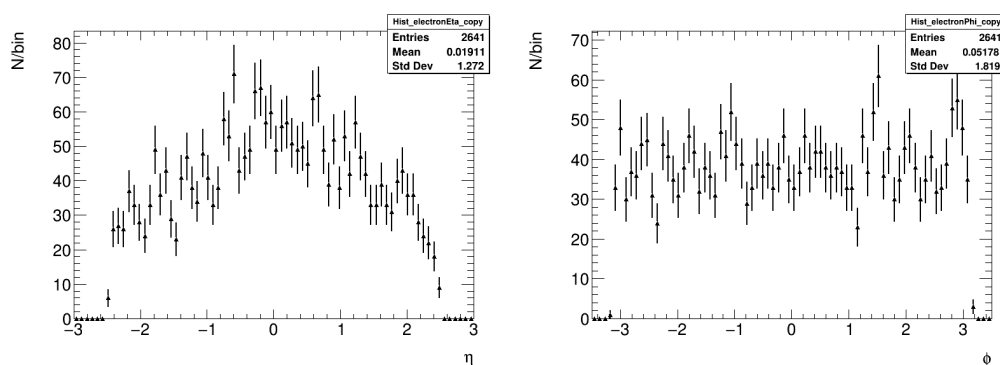


Figure 6.9: Invariant mass plot of the data with $p_T > 20$ GeV, but without the Higgs region.

6.2.2 Working point cut

In this subsection we will see how the Loose working point electrons change some of the different kinematics and the invariant mass.

The angles of the Loose electrons are shown in fig. 6.10a and fig. 6.10b. The electron ϕ is spread across the whole 2π range, like we saw in fig. 6.1b. The electron η in fig. 6.10a looks a lot like the truth η in fig 5.2, but not similar to the real data η in fig. 6.1a. It looks like the ATLAS detector don't have a η preference for Loose working points.



(a) The η of Loose electrons in the real data.

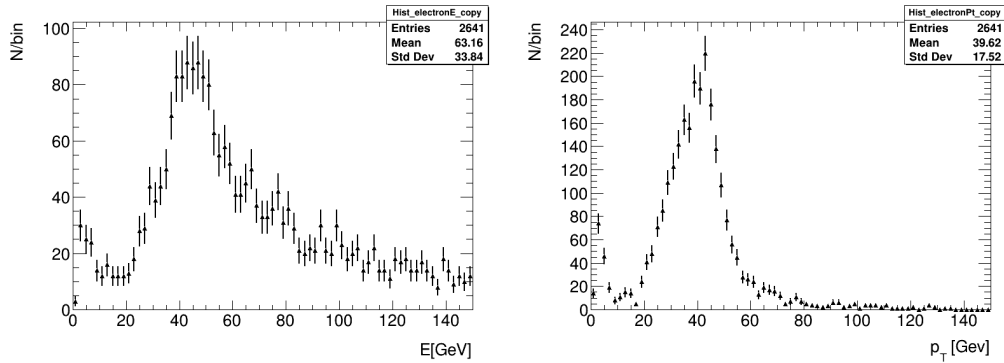
(b) The ϕ of Loose electrons in the real data.

Figure 6.10: The angles η and ϕ of the Loose electrons in the real data.

The energy and p_T of the Loose electrons are shown in fig. 6.11a and fig. 6.11b. They have a very different shape from the real data electrons in fig. 6.2a and fig. 6.2b and the MC $Z \rightarrow e^+e^-$ in fig. 5.3a and fig. 5.3b. This is because the Loose electrons do not have the small energy electrons that one can see in the real data sample. There are clear peaks at 45 GeV in both fig. 6.11a and fig. 6.11b. These peak were also present in energy and p_T of the real data and the MC $Z \rightarrow e^+e^-$.

In fig. 6.12 the number of electron per event is plotted. For Loose electrons most of the events have two electrons per event, which is the number of electrons one needs to find the invariant mass. We will still use the leading and sub-leading electrons to find the invariant mass.

The leading and sub-leading in fig. 6.13a and fig. 6.13b both have clear p_T peaks, the leading have a peak at 45 GeV and the sub-leading have a peak at 40 GeV. These peaks are more focused than the peak that comes from the



(a) The energy of Loose electrons in the real data. (b) The p_T of Loose electrons in the real data.

Figure 6.11: The energy and p_T of the Loose electrons in the real data.

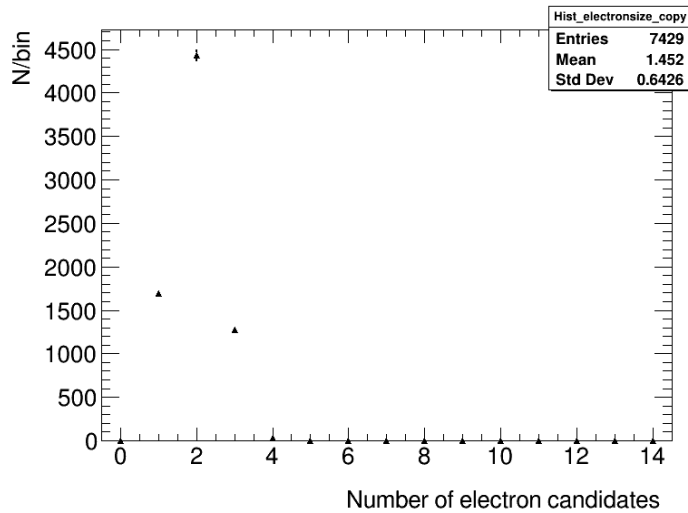


Figure 6.12: The number of electrons per event when looking at the Loose electrons.

$p_T > 20$ GeV cut. The leading p_T plot, fig. 6.13a, does not have a $p_T > 20$ GeV cut. The cut comes from the invariant mass cut from the DOAD. These peak means that there will be a 90 GeV peak. Like in the $p_T > 20$ GeV cut plots, fig. 6.7a and fig. 6.7b, there is a slope for the high p_T leading electrons and a clear cut of for the sub-leading electrons.

To see how the Loose electrons pair together, leading and sub-leading electrons a scatterplot is used, fig. 6.14. Like with the $p_T > 20$ GeV cut scatter plot in fig. 6.8, the (45,45) bright spot from fig. 6.5 is much clearer

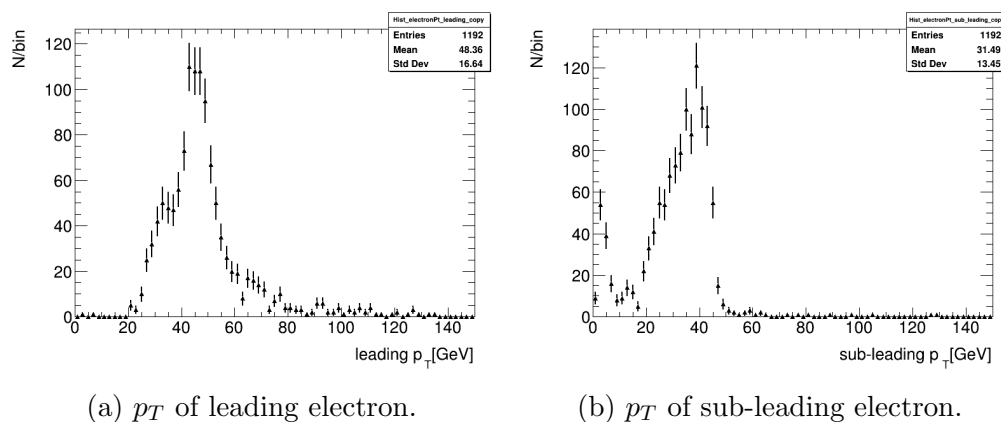


Figure 6.13: The leading and subleading p_T of the Loose electrons in the real data.

with Loose electrons and the (35,5) bright spot has disappeared. This means that there will be a 90 GeV Z peak in the invariant mass plot. The Loose electrons do not have the bright spot at (35,30), seen in fig. 6.8. This means that background in fig. 6.9 will not be there in the Loose electron invariant mass plot.

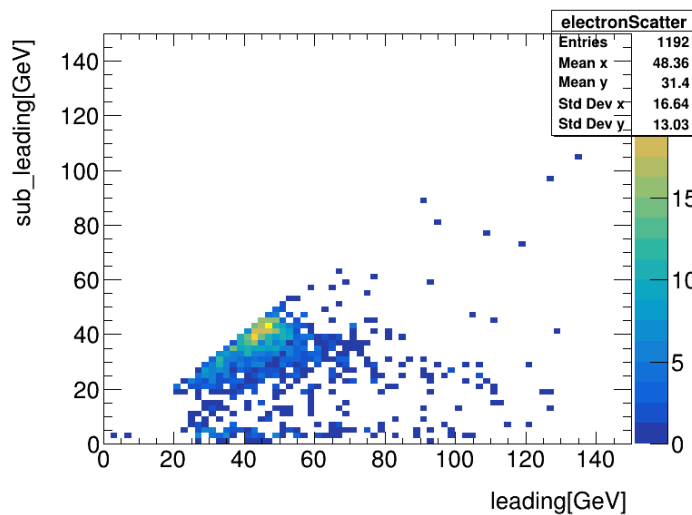


Figure 6.14: Scatterplot of the p_T of the leading electrons and sub-leading electron. There is a brightspot at coordinate (45,45)

The invariant mass of the real data with Loose electrons is shown in fig. 6.15. There is a clear 90 GeV Z peak and the 50 GeV peak in fig. 6.6 is cut.

Like with the $p_T > 20$ GeV cut, in fig. 6.9, the Loose electron removes most of the low invariant mass events. Unlike the $p_T > 20$ GeV cut there is almost no background in the Loose electron invariant mass.

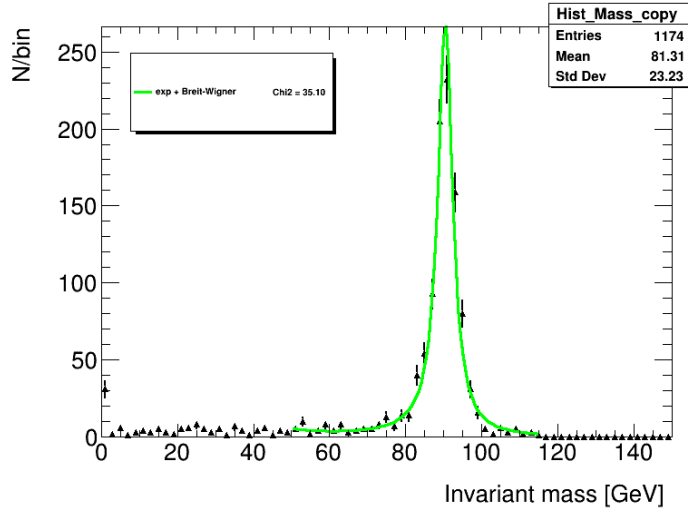


Figure 6.15: Invariant mass plot of the data with Loose working points without the Higgs region. The FWHM of this fit is 5.15 GeV

Like in the MC $Z \rightarrow e^+e^-$ and real data without working point cuts the significance with sub-leading and therefore leading electron p_T cuts have been found. Unlike the MC $Z \rightarrow e^+e^-$ and real data the p_T cuts does not increase the significance. This is because the Loose electrons do not have much background so the p_T cuts mostly cut into the signal and not the background. The equation for significance, eq. 5.2, then becomes:

$$\text{significance} = \frac{S}{\sqrt{S+B}} \approx \frac{S}{\sqrt{S}} = \sqrt{S} \quad (6.1)$$

The background for Loose electrons without cuts is already less than 1. So all the p_T cuts does not have much background to cut into, but the different cuts cut into the signal. Eq. 6.1 shows that lower signal, S , give lower significance.

Table 6.3: The significance of the p_T cuts on Loose electrons.

	without cuts	$p_T > 10$ GeV	$p_T > 20$ GeV
signal	2038.33	2023.20	1948.66
background + signal	2039.24	2024.31	1937.49
significance	45.1378	44.696	44.2707

6.3 Concluding comment

In this chapter the invariant mass model was tested on real data. Here without the Higgs region so this does not interfere with the model. The model works well on the real data when looking at the $Z \rightarrow e^+e^-$ decay.

For the $p_T > 20$ GeV cut there is more background in the invariant mass plot, than in the MC chapter. This is expected as there are a lot more background in the real data sample than in the MC sample and the $p_T > 20$ GeV cut works best at smaller masses. The $p_T > 20$ GeV cut still gives the highest significance of all the p_T cuts. The Loose invariant mass plot does not have much background even with the real data. For Loose electrons the highest significance was without any cuts. In the next chapter we will look at even more data and in those events both of these cuts will be used.

Chapter 7

$\text{H} \rightarrow e^+e^-$

In this chapter the Higgs region of the real data will be examined, first for the single file, used in chapter 6, and then for the whole sample. This sample is a DOAD from the whole year 2018. For Loose electrons a 2016 DAOD sample was used instead of the 2018 sample, as the Loose working points did not work for the whole 2018 sample.

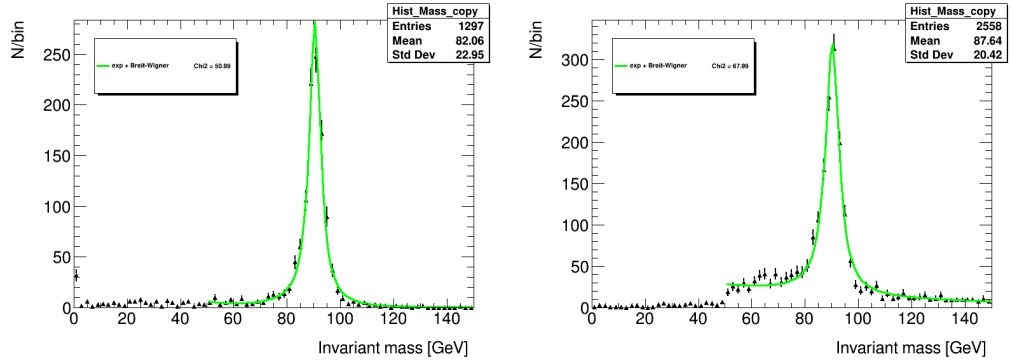
In this chapter a MC $\text{H} \rightarrow e^+e^-$ sample could have been used to examine how this decay would look like, but there was no Monte Carlo $\text{H} \rightarrow e^+e^-$ sample available at the time of this thesis.

7.1 Higgs region from a single file

In chapter 6, the Higgs region was not included in order to develop the reconstruction model. This model can now be used to investigate the Higgs decay. First the Higgs region of the invariant mass with sub-leading $p_T > 20$ GeV cuts, seen in fig. 6.9, and the Loose invariant mass, seen in fig. 6.15, will be examined with the Higgs region included. Looking at fig. 7.1a and fig. 7.1b, it is clear that the number of events in the Higgs region is fewer than in the Z region. The few events will stand out more clearly in some zoomed in plots that will be shown later in this chapter. Both of the invariant mass plots, fig. 7.1a and fig. 7.1b are well fitted by a Breit-Wigner and exponential background.

A closer look at the Higgs region of the invariant mass with sub-leading $p_T > 20$ GeV cuts, seen in fig. 7.1b, and the Loose invariant mass, seen in fig.

7.1. Higgs region from a single file



(a) The Loose invariant mass with Higgs region.

(b) The invariant mass with $p_T > 20$ GeV cut with Higgs region.

Figure 7.1: The invariant mass with Higgs region from a single file from the 2018 sample.

7.1a, will be examined more closely, seen in fig. 7.2 and fig. 7.3. They are both fitted with exponential backgrounds with Breit-Wigner distributions where the masses are manually set to the Higgs mass, 125 GeV. This is to look if there is a Higgs peak in the Higgs region.

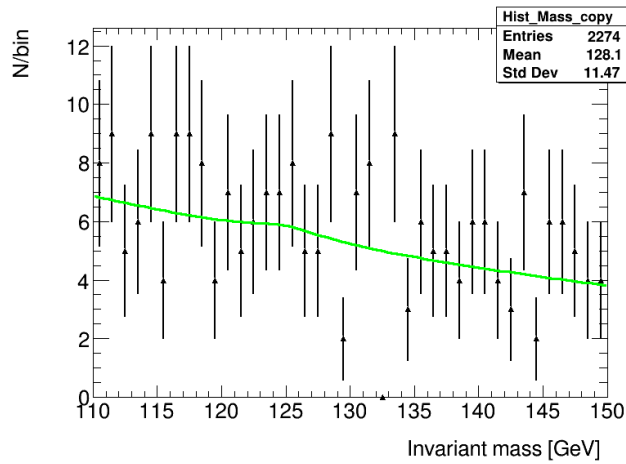


Figure 7.2: The Higgs region of the invariant mass from a single file from the 2018 sample with sub-leading $p_T > 20$ GeV cut seen in fig. 6.9 fitted with a Breit-Wigner with an exponential background. Here the mass of the Breit-Wigner is set to be the Higgs mass, 125 GeV.

For the Higgs region for the sub-leading $p_T > 20$ GeV, fig. 7.2, the exponential background fits well with the data, but there are very few events

with this high invariant mass. This means that the little peak at 125 GeV, with an amplitude of less than 1 probably does not mean a presence of Higgs particles. A larger sample is needed to get more result from this.

For the Higgs region for Loose electrons, fig. 7.3, there are almost no events with this high of invariant mass. Similar to the $p_T > 20$ GeV cut, little can be determined from this plot and a larger sample is needed.

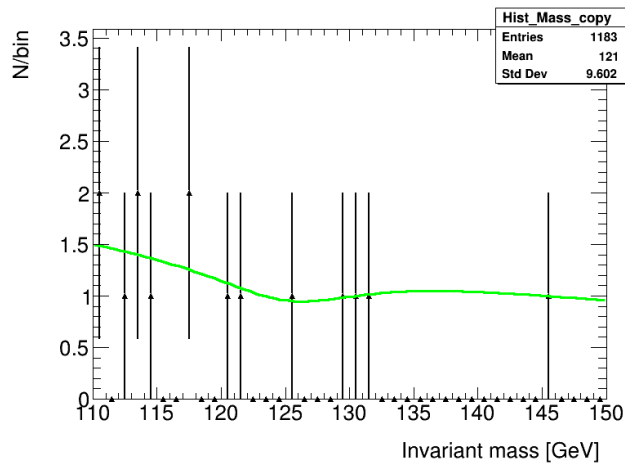


Figure 7.3: The Higgs region of the Loose invariant mass from a single file from the 2018 sample seen in fig. 6.15 fitted with a Breit-Wigner with an exponential background. Here the mass of the Breit-Wigner is set to be the Higgs mass, 125 GeV.

7.2 Higgs region from a whole sample

As shown in sec. 7.1. a single file contains too few events for the Higgs Boson decay to be investigated. To have more events to investigate, the whole 2018 sample from the ATLAS detector will be used.

This sample is very big, too big to be analysed locally, so it was done on the Grid. To investigate the sample a grid job was sent to the Grid with the model made in chapter 5 and a message of which sample that should be analysed. It took a few tries before it worked. Each grid-job took approximately two days, limiting the number of grid-jobs that could be performed for the model and sample.

The Loose electron working point cut did not work on the 2018 data

sample when working on the Grid. The grid job was returned without any cuts on the electron candidates. Therefore another sample had to be used instead. First a 2017 data sample was tried. This sample was the same type of DAOD as the 2018 data sample, so it could have been a good choice, but this sample did not work either as the Grid could not find this sample, therefore no analysis could be done. Lastly, a 2016 data sample was tried and the Loose electrons worked on this sample. This 2016 data sample is the same type of DAOD, a pair of electrons must have an invariant mass of over 50 GeV.

When looking at the DOAD from the whole year 2018, ROOT could only read 440 out of the 540 files that was made. This means that not all of the integrated luminosity $L = 58.5 \text{ fb}^{-1}$ was available for analysis. A guess for the integrated luminosity will be made by adjusting L as following: $L \approx \frac{440}{540} \cdot 58.5 \text{ fb}^{-1} = 47.7 \text{ fb}^{-1}$. This adjusted integrated luminosity will be used to calculate cross sections later in the chapter.

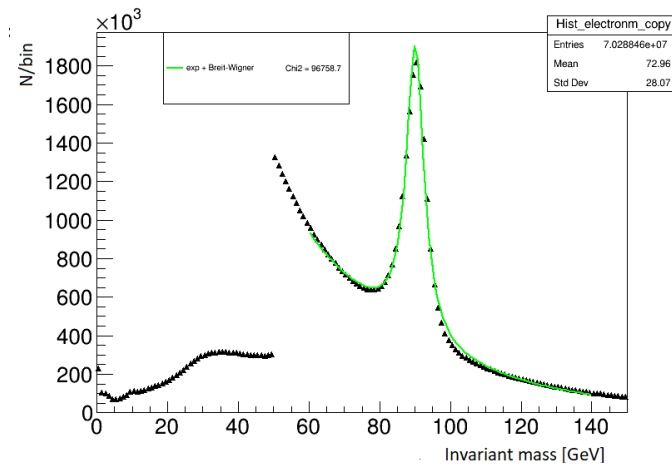


Figure 7.4: Invariant mass of the whole 2018 sample.

The invariant mass for the whole sample, in fig. 7.4, looks similar to the invariant mass from the one file, showed in fig. 6.6. The difference is the number of events in the plots, 6512 events in fig. 6.6 and $6.56 \cdot 10^7$ in fig. 7.4. This is around 10 000 times more events. The DAOD invariant mass cut of 50 GeV for a pair of electron candidates is very clear and there is a large Z peak at 90 GeV. The invariant mass of the whole sample is well fitted by a

Breit-Wigner distribution with an exponential background, just like for one file, seen in fig. 6.6.

7.2.1 2018 data with a $p_T > 20$ GeV cut

The invariant mass of the 2018 real data sample with a $p_T > 20$ GeV cut is shown in fig. 7.5. The cut removes most of the low invariant mass events and the exponential background is lowered. This makes the invariant mass under the 50 GeV peak, in fig. 7.4 disappear. The 50 GeV peak also disappears after the $p_T > 20$ GeV. This is very similar to how the $p_T > 20$ GeV cut worked on one file, seen in fig. 6.9. The number of events in the whole sample, $2.48 \cdot 10^7$, is also around 10 000 times more than the number of events in fig. 6.9, 2079.

The invariant mass with a $p_T > 20$ GeV cut is well fitted by a Breit-Wigner with an exponential background, just as in fig. 6.9. This fit will be used to calculate the cross section of $Z \rightarrow e^+e^-$ and $H \rightarrow e^+e^-$.

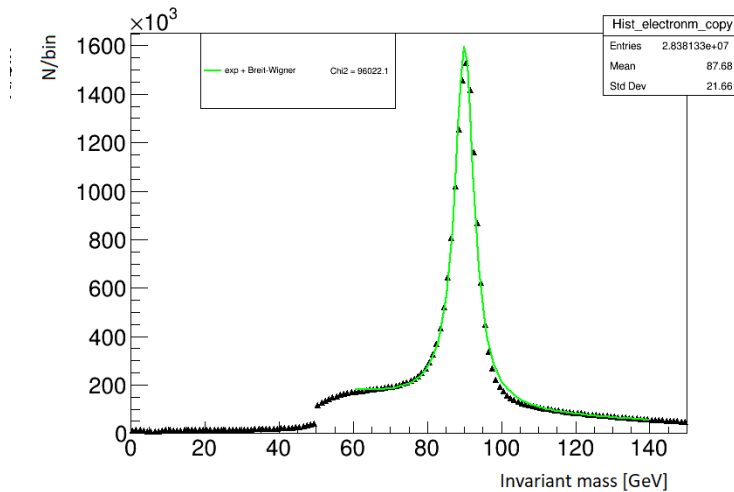


Figure 7.5: The invariant mass of the whole 2018 sample with a $p_T > 20$ GeV cut.

One can use this real data to calculate the cross section for $Z \rightarrow e^+e^-$ using eq. 2.10. To find N_{data} and $N_{background}$ the data is integrated over the Z peak region in fig. 7.5 and over the exponential background. Giving $N_{data} = 8.06055 \cdot 10^6$ and $N_{background} = 1.61736 \cdot 10^6$ and $N_{data} - N_{background} =$

$6.44319 \cdot 10^6$. Fig. 7.5 has more bins to give a clearer plot. This has to be taken into consideration when calculating the number of events. Here a bin has a width of 0.5 GeV, so the number of events must be multiplied by 2 to get the real number of events. The integrated luminosity is $L = 47.7 \text{ fm}^{-1}$ and the efficiency $\epsilon = 0.67$, as found in chapter 5, eq. 5.3. This gives an effective cross section of:

$$\sigma_{eff} = \frac{N_{data} - N_{background}}{\epsilon L} = \frac{2 \cdot 6.44319 \cdot 10^6}{0.67 \cdot 47.7 \text{ fm}^{-1}} = 0.40 \text{ nb} \quad (7.1)$$

Which is around a fifth of the actual cross section for $Z \rightarrow e^+e^-$ which is 1.9 nb and two fifths of the effective cross section from chapter 5, 1.05 nb.

7.2.2 2016 data with Loose working points

As explained in sec. 7.2.1, the Loose electrons did not give proper results in the Higgs region, because of the low number of events in one file. Therefore the whole 2018 real data sample was going to be examined, however this did not work for Loose working points. Neither the 2018 real data sample, that was used in the rest of the real data analysis, nor a 2017 real data sample worked with Loose working points. Loose working points did work on a 2016 real data sample. This data sample was also a DAOD, with the same invariant mass cut; an electron candidate pair having an invariant mass of over 50 GeV. This 2016 real data sample had an integrated luminosity of 35.6 fb^{-1} [34] and ROOT managed to run on all of the files that was created. So, unlike the 2018 sample, there will not be a need for an adjusted luminosity and $L = 35.6 \text{ fb}^{-1}$ will be used when calculating the cross sections.

The invariant mass of the real data with a Loose electron cut is shown in fig. 7.6. The cut removes both the low invariant mass events and also the exponential background. This cut also makes the invariant mass under the 50 GeV peak, as shown in fig. 7.4, disappear. This is very similar to how the Loose electron cut worked on one file from the 2018 data sample, seen in fig. 6.15. The number of events in the whole sample, $2.55 \cdot 10^7$, is also around 20 000 times more than the events in fig. 6.15, 1174.

Real data can be used to calculate the cross section for $Z \rightarrow e^+e^-$ by using eq. 2.10. To find N_{data} and $N_{background}$ one integrates over the data in the Z peak region and integrates over the exponential background just like

for the $p_T > 20$ GeV cut. Then $N_{data} = 1.02549 \cdot 10^7$ and $N_{background} = 24919$ and $N_{data} - N_{background} = 1.02299 \cdot 10^7$. Again must the binning be taken into consideration and this number is multiplied by 2. The integrated luminosity is $L = 35.6 \text{ fb}^{-1}$ and the efficiency $\epsilon = 0.56$, as found in chapter 5. This gives an effective cross section of:

$$\sigma_{eff} = \frac{N_{data} - N_{background}}{\epsilon L} = \frac{2 \cdot 1.02299 \cdot 10^7}{0.56 \cdot 35.6 \text{ fb}^{-1}} = 1.02 \text{ nb} \quad (7.2)$$

Which is around a half of the actual cross section for $Z \rightarrow e^+e^-$ which is 1.9 nb and very close to the effective cross section found in chapter 5, 1.06 nb.

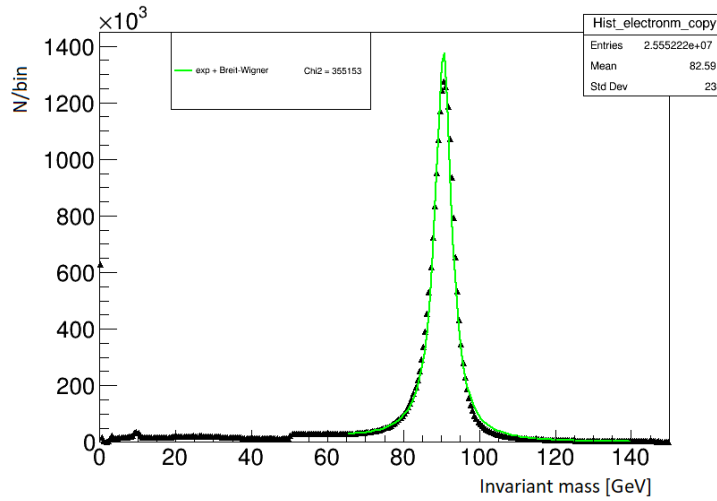


Figure 7.6: The Loose invariant mass of the whole 2016 sample.

The effective cross section for the real data are lower than the effective cross sections from the MC chapter. A reason for this difference could be that the analysed MC sample did not have a trigger calculation in it. The trigger would remove some of the electrons, thereby lowering the efficiency. The efficiency might also have gone down in the real data due to the pile up that can happen at high collision-rates. The Loose electrons had a pile up filter, so this might explain why the Loose cross section is so close to the MC cross section, while the cross section for the $p_T > 20$ GeV cut, where there was no pile up filter, was lower than the MC cross section.

To take this into consideration the effective cross section for the Higgs decay will be multiplied with a constant C , where $C = \frac{\sigma_{MC}}{\sigma_{Data}}$. For the $p_T > 20$

GeV cut the constant will be $C_{p_{Tcut}} = \frac{1.05 \text{ nb}}{0.40 \text{ nb}} = 2.63$ and for Loose electrons the constant will be $C_{Loose} = \frac{1.06 \text{ nb}}{1.02 \text{ nb}} = 1.04$.

7.2.3 Υ and J/Ψ found in the Loose invariant mass plot

There were some small peaks in fig. 7.6 under 10 GeV. To see these peaks more clearly a new invariant mass plot from 0 GeV to 15 GeV was made, seen fig. 7.7. Here there are clear peaks at 3 GeV and 9.5 GeV with some secondary peaks at around 3.75 GeV and 10 GeV. These peaks could be J/Ψ for the 3 GeV peak and Υ for the 9.5 GeV peak. These peaks are low because the DAOD invariant mass cut will remove most of these decays. Some are let through because the leading and sub-leading electrons was chosen to make the invariant mass, and not the two electrons that have the highest invariant mass, like the DAOD uses. So the invariant mass of a pair of electrons have an invariant mass over 50 GeV, but one or more of these electrons could be switched out by electrons with higher p_T , so the invariant mass goes down. When both electrons are switched out, some of the time they are switched to electrons from $\Upsilon \rightarrow e^+e^-$ or $J/\Psi \rightarrow e^+e^-$

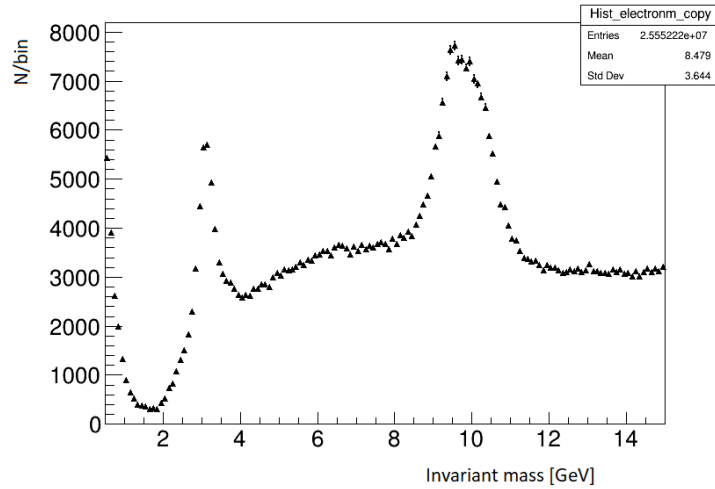


Figure 7.7: The Loose invariant mass of the whole 2018 sample in the 0 GeV to 15 GeV region.

7.3 Analysing $H \rightarrow e^+e^-$ using $p_T > 20$ GeV cut

To investigate the Higgs $\rightarrow e^+e^-$ decay one can look at the Higgs region and determine the number of events that occur here using a Gauss distribution with the exponential background. A Gaussian will be used because of the high background compared to signal in the Higgs region.

The Gaussian will have a forced mean, the Higgs mass 125 GeV. This is to make sure that the fit focuses on the Higgs boson. To find the σ of this Gaussian we will use the same σ as the truth invariant mass from the MC $Z \rightarrow e^+e^-$ chapter, as seen in fig. 7.8 fitted with a Breit-Wigner. Here the FWHM is 2.81 ± 0.08 GeV and the σ of this plot is $\sigma = \frac{\text{FWHM}}{2.355} = 1.19 \pm 0.034$ GeV.

To find a sigma for the Higgs peaks one can use the fact that the mass resolution, σ_M , is dominated by the energy measurement in the EM calorimeter and use the σ that arrives from energy measurements.

$$\sigma_E = k \cdot \sqrt{E} \quad (7.3)$$

To find a formula for the sigma of the mass:

$$\sigma_M = k \cdot \sqrt{M} \quad (7.4)$$

This can be used with the σ found from the truth electrons, $\sigma_Z = 1.19 \pm 0.034$ GeV, to find a σ for the Higgs mass σ_H :

$$\sigma_H = \sqrt{\frac{M_H}{M_Z}} * \sigma_Z = \sqrt{\frac{125 \text{ GeV}}{91.2 \text{ GeV}}} * 1.19 \pm 0.034 \text{ GeV} = 1.39 \pm 0.04 \text{ GeV} \quad (7.5)$$

This mean, 125 GeV and $\sigma_H = 1.39 \pm 0.04$ GeV will be used for both the $p_T > 20$ GeV cut and the Loose electrons.

When looking at the Higgs region of the invariant mass of the 2018 real data sample with a $p_T > 20$ GeV cut, seen in fig. 7.9, there is no clear Higgs peak. This is expected because of the low amounts of Higgs $\rightarrow e^+e^-$ decays found when doing a quick calculation in chapter 3, 0.003 times over the entire time period the ATLAS detector has been running.

7.3. Analysing $H \rightarrow e^+e^-$ using $p_T > 20$ GeV cut

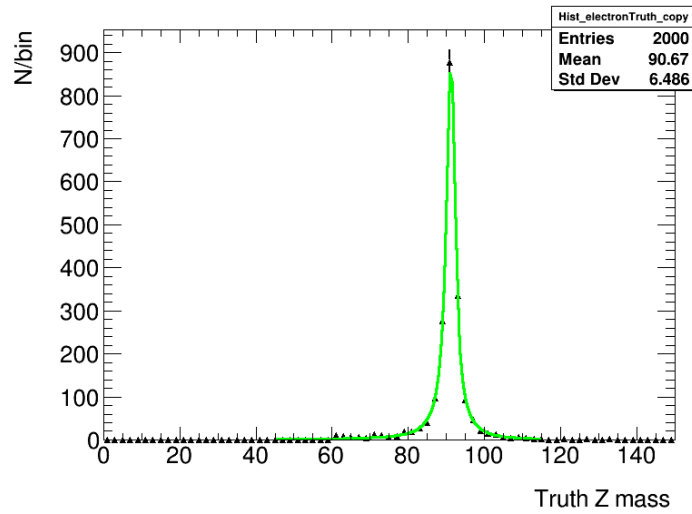


Figure 7.8: The truth invariant mass of the MC $Z \rightarrow e^+e^-$, here fitted with a Breit-Wigner.

To see what a Higgs peak could have looked like, a simulated Higgs peak is plotted, in fig. 7.10. This Higgs peak is a gaussian distribution with a mean of 125 GeV and a $\sigma = 1.39$ GeV and a height of 1200.

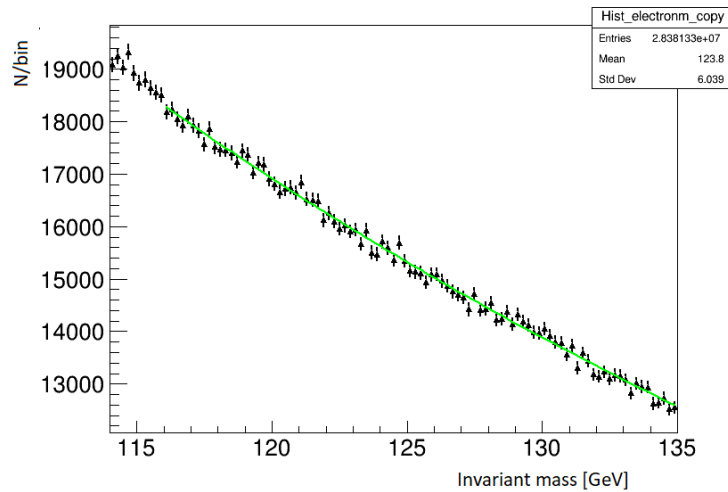


Figure 7.9: The Higgs region of the invariant mass of the whole 2018 sample with a $p_T > 20$ GeV cut fitted with a background in green. The Chi2 of this fit is 88.08.

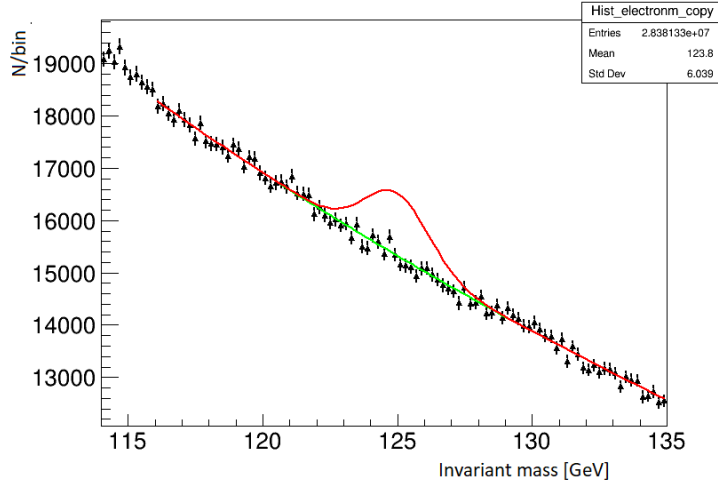


Figure 7.10: The Higgs region of the invariant mass of the whole 2018 sample with a $p_T > 20$ GeV cut. Here a simulated Higgs peak is plotted with a Gaussian in red.

When trying to fit the Higgs region with a $p_T > 20$ GeV cut with a Gaussian, as seen in fig. 7.11, a Higgs peak is found with a negative amplitude, which still can be used. Here the height of the Higgs peak is -84.49 ± 122.81 . This means that the number of signal events is less than $-84.49 + 1.96 \cdot 122.81 = 156.21$ to a confidence level (C.L.) of 95%. This means that there is only a 5% chance that pure background could give a positive fluctuation. However, we are not sure that this background-function is correct. So a more conservative number of signal events is less than $0 + 1.96 \cdot 122.81 = 240.71$. Here the binwidth is 0.2 GeV, so to get the real cross section one must multiply these numbers by 5.

By using this signal one gets a cross section of less than:

$$\sigma_{eff} < C_{p_T\text{-cut}} \cdot \frac{S}{\epsilon L} = 2.63 \cdot \frac{5 \cdot 240.71}{0.67 \cdot 47.7 \text{ fb}^{-1}} = 99.04 \text{ fb} \quad (7.6)$$

7.3. Analysing $H \rightarrow e^+e^-$ using $p_T > 20$ GeV cut

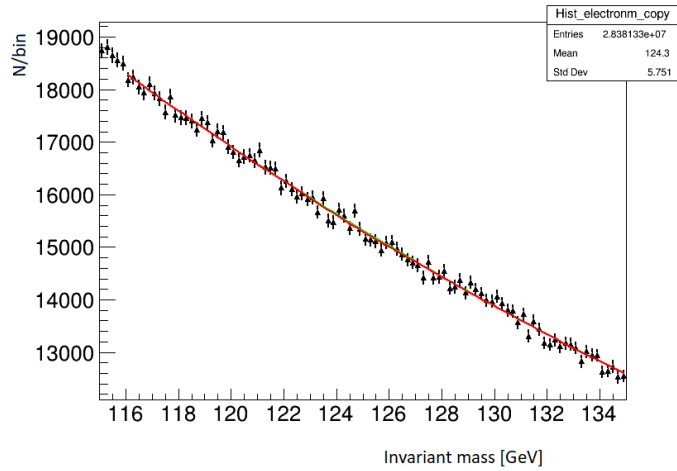


Figure 7.11: The Higgs region of the invariant mass of the whole 2018 sample with a $p_T > 20$ GeV cut. Here a Higgs peak is fitted with a Gaussian in red and background in green.

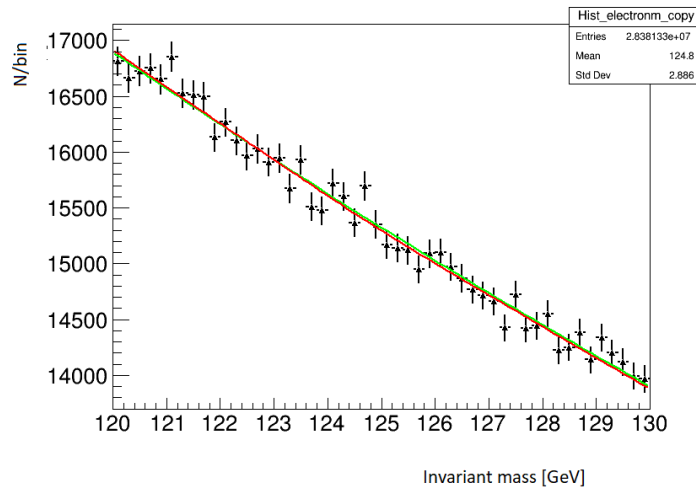


Figure 7.12: The Higgs region of the invariant mass of the whole 2018 sample with a $p_T > 20$ GeV cut with a Gaussian in red and background in green. This plot is zoomed in.

7.4 Analysing $H \rightarrow e^+e^-$ using Loose working points

When determining $H \rightarrow e^+e^-$ decay using Loose invariant mass, the Higgs region is plotted in fig. 7.13. In this plot one can still not see a clear Higgs peak. This is again expected because of the low amounts of $H \rightarrow e^+e^-$ decays found in chapter 4.

To see how a Higgs peak may have looked like, the same simulated Higgs peak as used in sec. 7.3 is plotted, in fig. 7.14. This Higgs peak is a gaussian distribution with a mean of 125 GeV and a $\sigma = 1.39$ GeV and a height of 1200. Here the simulated peak is much clearer as the background is much smaller.

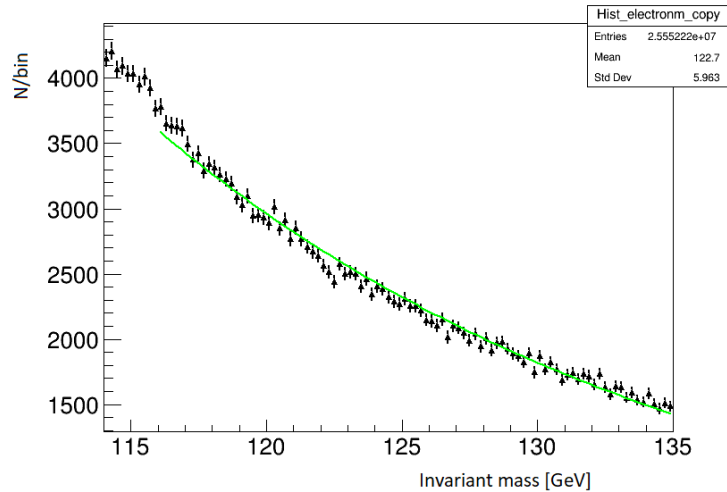


Figure 7.13: The Higgs region of the Loose invariant mass of the whole 2016 sample fitted with a background in green. The Chi2 of this fit is 164.96

When trying to fit the Higgs region of the invariant mass of Loose electrons with a Gaussian, as seen in fig. 7.15, a Higgs peak was found with a negative amplitude. Here the height of the Higgs peak is -208.60 ± 47.39 GeV. Which is a smaller error than for the 2018 data with a $p_T > 20$ GeV cut. Again using a more conservative number of signal events is less than $1.96 \cdot 47.39 = 92.88$. To take the binning into account this must be multiplied by 5.

7.4. Analysing $H \rightarrow e^+e^-$ using Loose working points

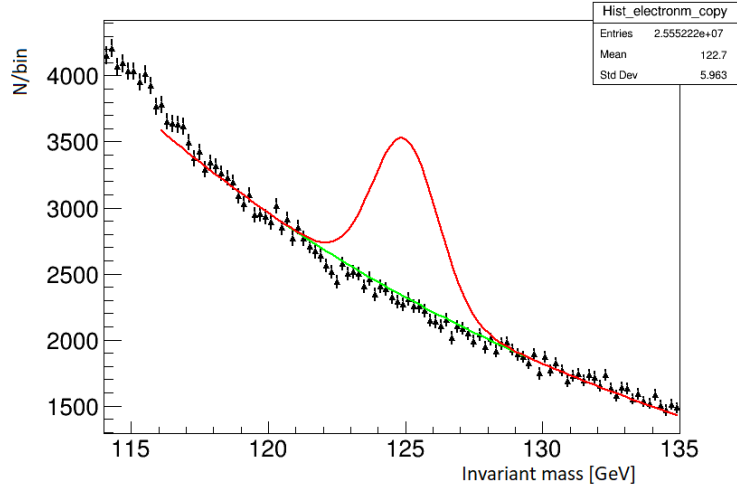


Figure 7.14: The Higgs region of the Loose invariant mass of the whole 2016 sample. Here with a simulated Higgs peak in red.

By using this signal one gets a cross section of less than:

$$\sigma_{eff} < C_{Loose} * \frac{S}{\epsilon L} = 1.04 \cdot \frac{5 \cdot 92.88}{0.56 \cdot 35.6 \text{ fb}^{-1}} = 24.23 \text{ fb} \quad (7.7)$$

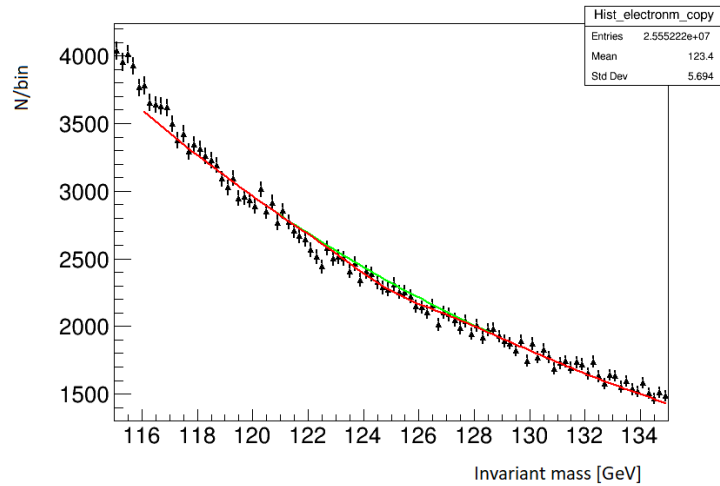


Figure 7.15: The Higgs region of the Loose invariant mass of the whole 2016 sample. Here a Higgs peak is fitted with a Gaussian in red and background in green.

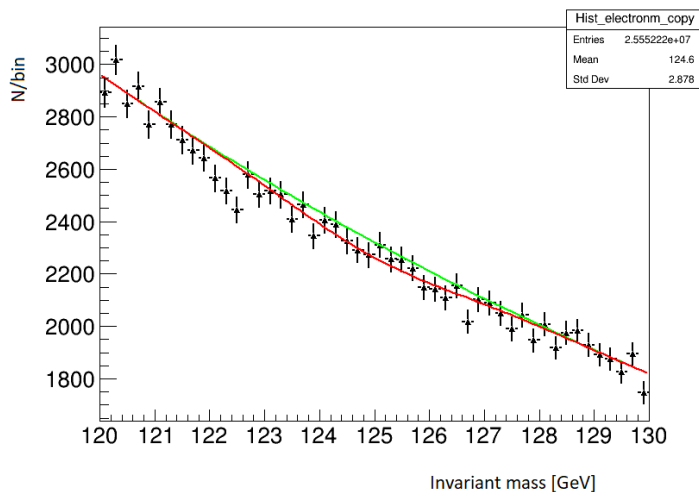


Figure 7.16: The Higgs region of the Loose invariant mass of the whole 2016 sample with a Gaussian in red and background in green. This plot is zoomed in.

7.5 Concluding comment

In this chapter the model for finding the Higgs using invariant mass of leading and sub-leading electrons was used on two real data samples, a DAOD of the whole year of 2018 and a DAOD of the whole year of 2016. For the 2018 data sample a $p_T > 20$ GeV cut was used, and for the 2016 data sample a Loose working point cut was done.

The invariant mass model worked very well on the $Z \rightarrow e^+e^-$ decay. The $p_T > 20$ GeV cut on the 2018 data sample gave an effective cross section of $\sigma_{eff} = 0.40$ nb, see eq. 7.1. This is just under half of the effective cross section found in chapter 5. This was because there was no triggers in the MC sample used in chapter 5 and no pile up filter was used on the 2018 sample. The 2016 data, with Loose electrons, gave an effective cross section of $\sigma_{eff} = 1.02$ nb, see eq. 7.2. This is very close to the effective cross section found in chapter 5, which means that most of the $Z \rightarrow e^+e^-$ decays was found using this method. This tells us that the model works very well for the $Z \rightarrow e^+e^-$ decay.

When looking at the $H \rightarrow e^+e^-$ decay there was not a clear peak in either of the real data invariant mass plots. This was expected as the branching

ratio for $H \rightarrow e^+e^-$ is so small. When fitting the Higgs region of the real data invariant mass plots, see fig. 7.12 and fig. 7.16 there was small Gaussians with negative amplitudes. These could still be used to find a limit for the cross section for the $H \rightarrow e^+e^-$ decay.

The 2018 data with a $p_T > 20$ GeV cut had a lot more background and a lot of uncertainty for the amplitude of the Gaussian. For the 2018 data sample a cross section of $\sigma_{eff} < 99.04$ fb was found, as seen in eq. 7.6. The 2016 data with Loose electrons had a lot less background and the uncertainty of the amplitude were also smaller. For the 2016 data sample a cross section of $\sigma_{eff} < 24.23$ fb was found, as seen in eq. 7.7.

Chapter 8

Results and Discussion

8.1 Finding Z and H using model

In this thesis a mass reconstruction model using the invariant mass of two electrons was developed. The model was developed and improved using the well understood $Z \rightarrow e^+e^-$ decay. The model was then used to investigate two different real data samples from the LHC of 2018 and 2016 using two different types of cuts. When analysing the data for Z bosons using the 2018 real data sample, with a $p_T > 20$ GeV cut, the effective cross section was found to be:

$$\sigma_{eff} = 0.40 \text{ nb} \tag{8.1}$$

While for the 2016 real data sample, with Loose electrons, the effective cross section was found to be:

$$\sigma_{eff} = 1.02 \text{ nb} \tag{8.2}$$

These effective cross sections were close to the effective cross sections found for the Monte Carlo sample in chapter 5, $\sigma_{eff,MC} = 1.05$ nb and 1.06 nb for the 2018 and 2016 sample respectively. For the 2018 real data sample, with a $p_T > 20$ GeV cut, the effective cross section was about half of the MC. The difference between 2018 real data and the Monte Carlo is most likely because of the issues with the Grid and the fact that there was no pile up filter done on the 2018 sample. The first attempts running the 2018 sample

on the Grid returned just empty directories with no ROOT files. When the Grid job returned files, ROOT could only read 440 out of the 540 files. This gives a lot of uncertainty of the integrated luminosity L .

For the 2016 real data sample, with Loose electrons, the effective cross section was similar to the effective cross section from the MC. This is because this sample did not have the same issues as the 2018 sample, there was a pile up filter and ROOT could read out all the files created. The results from the model, both cuts, indicates that the model works very well at finding the $Z \rightarrow e^+e^-$ decay. The mass reconstruction model using invariant mass should therefore also be able to find the $H \rightarrow e^+e^-$ decay.

When analysing the samples for Higgs bosons it is clear that the samples have little or no $H \rightarrow e^+e^-$ decays. For the $H \rightarrow e^+e^-$ decay there was no clear peak in the Higgs region, as seen in fig. 7.9 and in fig. 7.13. The lack of $H \rightarrow e^+e^-$ decay is expected as the calculation in chapter 4 showed that there is 0 expected decays of this sort at the ATLAS detector. The effective cross section calculation can, however, still be done. When doing this, upper limits for the effective cross sections of the $H \rightarrow e^+e^-$ decay was found. For the 2018 real data sample, with a $p_T > 20$ GeV cut, the cross section limit was found to be:

$$\sigma_{eff} < 99.04 \text{ fb} \quad (8.3)$$

For the 2016 real data sample, with Loose electrons, the effective cross section limit was found to be:

$$\sigma_{eff} < 24.23 \text{ fb} \quad (8.4)$$

These effective cross sections are very low, as expected. Both of the invariant masses were fitted with Gaussian distributions with negative amplitudes, seen in fig. 7.11 and in fig. 7.15, so the limit to the cross section was therefore dependant on the uncertainty. The 2018 sample with a $p_T > 20$ GeV cut has a higher limit as there was high uncertainty in the amplitude of the Gaussian fit done, ± 122.81 , seen in fig. 7.11. The 2016 sample with Loose electrons had smaller uncertainty, ± 47.39 , and therefore has a smaller limit. By identifying these low limits, the model confirms that there little to no $H \rightarrow e^+e^-$ decay in these samples.

8.2 Uncertainty

The cross sections for $H \rightarrow e^+e^-$, from 2018 data with a $p_T > 20$ GeV cut and from 2016 data with Loose electrons, were analysed in chapter 7 showing no decays in the Higgs region as expected from the calculations in chapter 3 and chapter 4. However, the results in chapter 7 should be understood as limits of the cross sections as there was not performed a proper uncertainty analysis due to the challenges running the grid jobs, especially the files that did not return data that could be analysed.

Even though the uncertainty cannot be quantified correctly, the most important contributions to the uncertainty will be addressed. For this model, the largest errors come from the integrated luminosity and from the efficiency. It is also important to point out that the background functions used in chapter 7 are not properly verified and could contain undocumented variations. A first approach uncertainty of the cross section is shown in eq. 8.5.

$$\left(\frac{\sigma_\sigma}{\sigma}\right)^2 = \left(\frac{\sigma_\epsilon}{\epsilon}\right)^2 + \left(\frac{\sigma_{\mathcal{L}}}{\mathcal{L}}\right)^2 + \left(\frac{\sigma_{background}}{background}\right)^2 \quad (8.5)$$

The uncertainty from the integrated luminosity, σ_L , is split into two parts. The uncertainty of the integrated luminosity that was ran over in this thesis and the uncertainty of the integrated luminosity measured at the ATLAS detector. The uncertainty from this thesis comes from the problems with running on the Grid. For the 2018 sample, ROOT could only read 440 out of the 540 files that was created. ROOT could read out all the files created from the 2016 sample, but this does not mean that every event from this sample was correctly read out. It is difficult to determine the uncertainty due to these problems, and in order to quantify the uncertainty a number of trials must be run on the Grid. The uncertainty in measured integrated luminosity was not available at the source for the luminosity, [34], but this uncertainty is probably not as large as the uncertainty from the Grid job.

In this thesis, the efficiency for the invariant mass model, with the two different cuts, was found using a Monte Carlo $Z \rightarrow e^+e^-$ sample, as there was no $H \rightarrow e^+e^-$ Monte Carlo sample available at the time of this thesis. The difference between these processes could give some uncertainty. The uncertainty of the efficiency was not calculated for the different cuts either. For the 2018 data sample there was also no pile-up filter which there where

for the MC sample and the 2016 data sample. This would also give a lot of uncertainty to the efficiency.

In chapter 7 the background was used as if it was known, but this is not true. The Chi2 of the 2018 data sample with the $p_T > 20$ GeV cut was 88.08, as seen in fig. 7.9, and for the 2016 data sample with Loose electrons the Chi2 was 164.96, as seen in fig. 7.13. This is not a high Chi2 compared to the Chi2 from the Z peak fits, Chi2 = 96022 as seen in fig. 7.5 and Chi2 = 355153 as seen in fig. 7.6.

To quantify the uncertainty of the model, more jobs must be run on the Grid and ROOT, and will be an important point in the further development of the model.

8.3 Improving cuts

In this thesis only the Loose working points worked. This working point is one of the weaker working points and will let through more electrons than the stronger working points, like Medium and Tight, as seen in fig. 5.18. These stronger cuts would most likely remove more of the background, leading to clearer peaks. However, they would cut more into the signal as well, this could make them a worse choice. This could be an interesting thing to look at in further research.

To improve the current model, different cuts should be investigated. Most likely would Tight electrons be the best choice, as there are so many electron candidates that are actually photons created by bremsstrahlung, and this create a lot of background for electrons. Tight electrons have the strongest requirements and would therefore cut away much more of the background.

Another way to do the cuts would be to look at one electron at a time. For example, cutting the leading electrons with a higher p_T than the sub-leading electrons.

And a last suggestion of improving the cuts, would be to do the different cuts on the same sample. All of these improvements would require significant Grid time.

8.4 Concluding remark

A model using invariant mass has been developed and verified towards real Z and Higgs boson data from the ATLAS detector. The results clearly show that the model is capable of finding the Z bosons decaying into e^+e^- in the real data. It can be concluded that the invariant mass model works for the current samples, and it does not find Higgs bosons decaying into e^+e^- in the real data. This means that the cross section for the $H \rightarrow e^+e^-$ decay must be small, which is confirmed by the model.

Chapter 9

Conclusion

In this thesis an invariant mass model, with two different types of cuts, was developed by looking at a Monte Carlo $Z \rightarrow e^+e^-$ sample. This model used the leading and sub-leading electrons to find the invariant mass.

When testing this model on real data, two different data samples were used. A 2018 real data sample with a $p_T > 20$ GeV cut and a 2016 real data sample with Loose electrons. When testing the model on real data, it worked more than satisfactory on the $Z \rightarrow e^+e^-$ decay, getting approximately the same cross section as for the MC sample. It was much closer for the 2016 sample with Loose electrons than for the 2018 sample with a $p_T > 20$ GeV cut. This is because of there was no pile up filter and ROOT was not able to read all of the files the Grid made when running on the 2018 sample.

The model worked satisfactory on the $Z \rightarrow e^+e^-$ decay, but did not find any $H \rightarrow e^+e^-$ decay. This is expected as the branching ratio for $H \rightarrow e^+e^-$, as calculated in chapter 3, is quite small. For the 2018 real data sample, with a $p_T > 20$ GeV cut, the cross section limit was found to be $\sigma_{eff} < 99.04$ fb. For the 2016 real data sample, with Loose electrons, the effective cross section limit was found to be $\sigma_{eff} < 24.23$ fb.

Over all the model worked very well finding a limit for the effective cross section of the $H \rightarrow e^+e^-$ decay.

Bibliography

- [1] "CERN" <https://en.wikipedia.org/wiki/CERN> 08.03.2021 14:51
- [2] "About CERN" <https://home.cern/about> 29.04.2021 12:39
- [3] "World Wide Web" https://en.wikipedia.org/wiki/World_Wide_Web
08.03.2021 15:25
- [4] "The Large Hadron Collider" <https://home.cern/science/accelerators/large-hadron-collider> 08.03.2021 16:03
- [5] Tommy Ohlsson *RELATIVISTIC QUANTUM PHYSICS* 2011
- [6] "Large Hardon Collider" https://en.wikipedia.org/wiki/Large_Hadron_Collider#Detectors 09.03.2021 16:05
- [7] "ATLAS" <https://home.cern/science/experiments/atlas> 29.04.2021 12:50
- [8] "Concept of luminosity" <https://cds.cern.ch/record/941318/files/p361.pdf>
06.05.2021 19:15
- [9] "Measurement of W^{\pm} -boson and Z-boson production cross-sections in p p collisions at $\sqrt{s} = 2.76$ TeV with the ATLAS detector" <https://arxiv.org/pdf/1907.03567.pdf> 29.04.2021 12:52
- [10] "Measurement of W^{\pm} -boson and Z-boson production cross-sections in p p collisions at $\sqrt{s} = 13$ TeV with the ATLAS detector" <https://arxiv.org/pdf/1603.09222.pdf> 29.04.2021 12:54
- [11] "Pseudorapidity" <https://en.wikipedia.org/wiki/Pseudorapidity>
25.02.2021 15:05

-
- [12] "Accererators and particle detectors"
http://edu.itp.phys.ethz.ch/hs10/ppp1/2010_11_02.pdf 25.02.2021 15:05
- [13] "The Inner Detector" <https://atlas.cern/discover/detector/inner-detector> 25.02.2021 14:18
- [14] "Keeping the ATLAS Inner Detector in perfect alignment"
<https://atlas.cern/updates/experiment-briefing/inner-detector-alignment> 26.02.2021 10:50
- [15] "Alignment of the ATLAS Inner Detector in Run-2"
<https://arxiv.org/pdf/2007.07624.pdf> 26.02.2021 11:15
- [16] "The Barrel Modules of the ATLAS SemiConductor Tracker"
<https://cds.cern.ch/record/974073/files/indet-pub-2006-005.pdf>
28.02.2021 15:15
- [17] "Calorimeter" <https://atlas.cern/discover/detector/calorimeter> 25.02.2021 14:18
- [18] "Calorimeter (particle physics)" [https://en.wikipedia.org/wiki/Calorimeter_\(particle_physics\)](https://en.wikipedia.org/wiki/Calorimeter_(particle_physics)) 03.03.2021 13:44
- [19] "Particle shower" https://en.wikipedia.org/wiki/Particle_shower#Types_of_showers 03.02.2021 14:54
- [20] "Computer Generated image of the ATLAS calorimeter"
<https://cds.cern.ch/record/1095927> 08.02.2021 14:00
- [21] "PASSAGE OF PARTICLES THROUGH MATTER"
<https://pdg.lbl.gov/2005/reviews/passagerpp.pdf> 29.04.2021 13:01
- [22] "Muon Spectrometer" <https://atlas.cern/discover/detector/muon-spectrometer> 25.02.2021 14:18
- [23] "Computer generated image of the ATLAS Muons subsystem"
<https://cds.cern.ch/images/CERN-GE-0803017-01> 25.02.2021 14:18

- [24] M. Aaboud, G. Aad, B. Abbott et al. *Electron reconstruction and identification in the ATLAS experiment using the 2015 and 2016 LHC proton-proton collision data at $\sqrt{s} = 13$ TeV* The European Physical Journal C 79 (Aug,2019) 639–639
- [25] Tommy Ohlsson *RELATIVISTIC QUANTUM PHYSICS* 2011
- [26] The Standard Model <https://physics.info/standard/> 19.04.2021 15:10
- [27] John C. Morrison *Modern Physics for Scientists and Engineers* 2015
- [28] Ernest M Henley and Alejandro Garcia *SUBATOMIC PHYSICS* 2007
- [29] Higgs boson https://en.wikipedia.org/wiki/Higgs_boson#Decay 20.04.2021 15:03
- [30] What dictates how the Higgs boson will decay? <https://physics.stackexchange.com/questions/426243/what-dictates-how-the-higgs-boson-will-decay> 20.04.2021 15:03
- [31] Bjarne Stugu *Measurements of Cross Sections and Couplings of the Higgs Boson Using the ATLAS Detector* 2017
- [32] Decays of the Standard Model Higgs <https://profmattstrassler.com/articles-and-posts/the-higgs-particle/the-standard-model-higgs/decays-of-the-standard-model-higgs/> 02.06.2021 18:52
- [33] Steffen Maeland *Pixel detector performance and study of CP invariance in H to tau tau decays with the ATLAS detector* 2017
- [34] LuminosityPublicResultsRun2 <https://twiki.cern.ch/twiki/bin/view/AtlasPublic/LuminosityPublicResultsRun2> 02.06.19:38
- [35] The Higgs boson <https://home.cern/science/physics/higgs-boson> 11.06.2021 21:20
- [36] Jet performance in ATLAS; First 13 TeV jet results https://indico.in2p3.fr/event/12594/attachments/8609/10685/SeminarCPPM_light.pdf 13.05.2021 12:16

-
- [37] Running the Full Chain <https://twiki.cern.ch/twiki/bin/viewauth/AtlasComputing/WorkBookFullChain> 13.05.2021 12:46
- [38] Why the Monte Carlo method is so important today https://cs.fit.edu/~ryan/cse1002/reading/mc_wics1314.pdf 13.05.2021 12:46
- [39] The Worldwide LHC Computing Grid <https://cds.cern.ch/record/1997398> 05.06.2021
- [40] About ROOT <https://root.cern/about/> 10.03.2021 17:30
- [41] Project Founders https://root.cern/about/project_founders/ 10.03.2021 17:27
- [42] The Athena Framework <https://twiki.cern.ch/twiki/bin/view/AtlasComputing/WorkBookAthenaFramework> 13.05.2021 17:14
- [43] ATLAS Computing <http://cdsweb.cern.ch/record/837738/files/lhcc-2005-022.pdf> 13.05.2021 19:53
- [44] C++ <https://en.wikipedia.org/wiki/C%2B%2B> 10.03.2021 17:30
- [45] Bjarne Stroustrup's FAQ https://www.stroustrup.com/bs_faq.html#what-is 29.04.2021 13:09
- [46] Python (programming language) [https://en.wikipedia.org/wiki/Python_\(programming_language\)](https://en.wikipedia.org/wiki/Python_(programming_language)) 10.03.2021 17:30
- [47] General Python FAQ <https://docs.python.org/3/faq/general.html#what-is-python> 29.04.2021 13:12
- [48] Relativistic Breit–Wigner distribution https://en.wikipedia.org/wiki/Relativistic_Breit%E2%80%93Wigner_distribution 10.03.2021 17:54
- [49] Pythia 6.4 <https://ftp.fau.de/gentoo/distfiles/lutp0613man2.pdf> 29.04.2021 12:46
- [50] Crystal Ball function https://en.wikipedia.org/wiki/Crystal_Ball_function 10.03.2021 17:55

Bibliography

- [51] Electron reconstruction and identification in the ATLAS experiment using the 2015 and 2016 LHC proton–proton collision data at $\sqrt{s} = 13$ TeV <https://arxiv.org/pdf/1902.04655.pdf> 11.05.2011 13:20

- [52] eGamma AOD derivations https://twiki.cern.ch/twiki/bin/viewauth/AtlasProtected/EGammaAODDerivations#How_to_extend_the_DAOD_production 18.05.2021 17:58